Photon correlations probe the quantized nature of light emission from optoelectronic materials

John M. Lupton[*)] and Jan Vogelsang[**)]

Institute for Experimental and Applied Physics, and Regensburg Center for Ultrafast Nanoscopy (RUN), University of Regensburg, 93049 Regensburg, Germany

Even though the quantized interaction between light and matter in the photoelectric effect is considered one of the cornerstones in the development of quantum mechanics, it was long thought impossible to directly observe the quantized nature of light itself. The advent of light-intensity autocorrelation techniques in the 1950s, first developed to study the size of stars, changed little in this perception, until true single-photon correlation spectroscopy from trapped ions was proven to be possible in the late 1970s: photons from a single quantum emitter tend to arrive in bunches, but each light quantum is spaced apart in time – it is antibunched. Initially considered only as the workhorse of atomic quantum optics, over the past two decades, photon correlation techniques have become a standard in fields as diverse as quantum-information processing, biological imaging, polymer physics and materials science in general. The technique is particularly useful for probing materials that are specifically designed to emit or absorb light in optoelectronic devices, such as light-emitting diodes, solar cells or lasers. The central question in such studies is how large a mesoscopic piece of material can become and still behave as an atom-like source of single photons. What interactions may arise between multiple excitations within a material, and what sort of dark states may give rise to intermittency in the stream of photons? We review the many different classes of optoelectronic materials for which photon-correlation spectroscopy has proven to offer useful insight into excited-state dynamics, ranging from molecular, over semiconductor to metallic nanostructures. The technique is particularly suited to probing mesoscopic aggregates of organic semiconductors since each single molecule acts as a quantum emitter itself.

---

*) Email: john.lupton@ur.de

**) Email: jan.vogelsang@ur.de

I. INTRODUCTION

On a dark desert highway, driving westwards through nighttime southern Nevada, crossing a bend, one begins to perceive the distant lights of Las Vegas as a faint steady glow in the sky. Drawing nearer, the glow turns to a glimmer and soon the expanse of light becomes apparent. Closer still, and the largest and brightest buildings become visible until, ultimately, individual sources of light are discernible. On these different length scales, the dynamics of the optical perception depend on different parameters: the faint glimmer of the distant city depends both on atmospheric turbulences and on the inherent dynamics of the sparkling illuminations. The closer one gets, the more dominant the intrinsic features of each individual light source become. But what if the light-emitting objects are so small that they cannot be resolved individually in space, such as single atoms or molecules? Or if we cannot zoom in indefinitely, such as when observing a distant star with a telescope? The point is that there is subtle information on the collection of light emitters within the enclosing medium to be found in the time dependence of the overall light intensity. The way to extract this information is to search for patterns in the temporal functionality, which are revealed by an autocorrelation analysis of the signal, i.e. a mathematical convolution of the signal with itself. Such intensity autocorrelations were introduced in the 1950s in astronomy to measure the size of stars.[1-3]

Perhaps the most famous null result in history was the outcome of Michelson's and Morley's interferometry experiment to probe the presence of a preferred frame of reference for light, a "*luminiferous aether*" which purportedly serves as the medium of propagation of electromagnetic waves.[4] Shining a beam of light onto an angled semitransparent mirror through which it either passes or is reflected creates two beam paths, which can subsequently be superimposed again to interfere with each other as sketched in Figure 1a. As the difference in pathlength ΔL changes, the interference of electric-field amplitudes oscillates between constructive and destructive, giving rise to an oscillation in the detected light intensity. Such interferometers are exquisitely sensitive to changes in path lengths, down to the fraction of an atomic nucleus, and are even used to detect the gravitons formed in the intergalactic collision of two black holes.[5] They are used widely in spectroscopy and metrology, and in optical communications. The Michelson-Morley interferometer (MMI) measures the temporal coherence of a light source, in effect the autocorrelation of the electric field amplitude. The degree of coherence is defined as the normalized correlation of the electric field amplitudes. The broader the bandwidth of a light source, i.e. the broader the spectral range covered by it, the smaller the spatial displacement possible between the two interferometer arms for which interference fringes are observable. The uncertainty principle is at play here: the greater the spectral width, the greater the uncertainty in the frequency of the elementary light wave – the smaller the uncertainty in time and hence the shorter the time, over which the phase relationship between the two beam paths holds. The MMI measures the first-order correlation function of the field amplitude as a function of delay time Δt, $g^{(1)}(\Delta t)$. The mathematical connection between this correlation function and the spectral bandwidth of the light source is straightforward to show: $g^{(1)}(\Delta t)$ corresponds to the Fourier transform of the intensity spectrum,[6] a fact that is widely utilized in Fourier-transform infrared (FTIR) spectroscopy.

But what if we only consider one half of the interferometer, i.e. instead of superimposing the two beam paths to let them interfere we simply measure the intensity in each arm by a photodetector as sketched in Figure 1b. This measurement corresponds to the second-order correlation function $g^{(2)}(\Delta t)$ and seems like a rather trivial simplification of the MMI. When photons arrive at entirely random times, such as in the case of stimulated emission in a laser, no correlation exists between the two detectors either side of the beam splitter. In this case, the second-order intensity autocorrelation function is simply a time-independent constant, i.e. $g^{(2)}(\Delta t) = \text{const.}$ The analysis can have profound consequences since the light intensity is proportional to the photon number and the number of photons is discrete, i.e. quantized. What if only one single photon at a time impinges on the beam splitter? Quantum mechanics tells us that the photon can be both transmitted and reflected so that it interferes with itself, as in the double-slit experiment. But it can be detected only either in the transmission or in the detection pathway, not in both. Measuring the photon coincidence rate, i.e. the intensity cross-correlation between both detectors, will then yield a distinct absence of correlation for zero delay time between the two detectors: the intensity autocorrelation function at $\Delta t = 0$ will be $g^{(2)}(\Delta t = 0) = 0$. This case is referred to as photon antibunching. This situation, which relates to the wave-particle duality, bears some connection to one of the paradigmatic thought experiments of the apparent conflict between the quantized nature of energy and matter and the theory of of space and time, special relativity – a "paradox" named after Einstein, Podolsky and Rosen (EPR).[7] The physical reality of the problem is such that it lies in the nature of the photon to occupy both light paths emanating from the beam splitter but that it can only be picked up by one of the detectors. The photon wavefunctions delocalized on either side of the semitransparent mirror are said to be quantum-mechanically entangled until the wavefunction collapses as a result of the detection event. This entanglement can also arise for multiple photons at once and is at the heart of the modern technology of quantum cryptography and communication, where, for example, the deterministic correlation in the polarization of a pair of photons is considered.[8]

The intensity autocorrelation of light should also reveal a second striking effect, related to the quantum statistics of photons. Electrons are so-called fermions, implying that no two particles can occupy the same energy state with the same quantum numbers. Their distribution in energy follows Fermi-Dirac counting statistics, which spaces them apart in energy. The opposite is true for photons, which are bosons: these follow Bose-Einstein statistics, implying that photons prefer to "huddle together" in the same energetic state. The result is that for light generated by a source in thermal equilibrium, such as a blackbody radiator, photons will not arrive randomly in time but will tend to "bunch" together. As a consequence, in an intensity interferometer, the second-order correlation function – either the autocorrelation of the time-dependent intensity or the cross-correlation between two detection arms of a beam splitter – will tend to increase as the time difference between two photon detection events on either side of the beam splitter Δt decreases to zero. In this case, for the photons to be in thermal equilibrium, the light source must emit many photons simultaneously. However, a single-photon source that shows photon antibunching on a short time scale may also show "photon bunching" on a longer time scale if the single photons arrive bunched together in specific time intervals. Such an effect may have entirely classical origins, such as the time lag arising in a single-photon LED due to capacitative charging and discharging effects, but it may also be linked to excursions of the single-photon source to long-lived "dark" quantum states from which no light emission occurs.[9]

Intensity autocorrelations were first studied in 1954 by Hanbury Brown and Twiss (HBT),[1] who used the technique to determine the size of a star. Instead of timing each detector individually, which requires high-frequency electronics, the correlation between the two detectors was measured as the length of one interferometer arm was changed, corresponding to an increase in Δt. For a perfectly coherent point source serving as the origin of Hyugens plane waves one would not expect to see any difference in the fluctuations of the light intensity detected as Δt is changed: the correlation should be flat because it is always the waves emanating from the same origin which are detected by both detectors. However, if the star has a finite size, then changes in path length will correspond to changes in the side of the star from which the light originates. If the light emerges from the same side, then correlations will persist; if the interferometer probes the two opposite sides of the star, i.e. two different light sources, the correlation is lost.

Together with information on the physical distance of the star to the observer, the path length over which a correlation signal exists allows the apparent diameter of the star to be computed.

This correlation analysis of light inspired by HBT is now a central method in quantum optics and crucial to quantum cryptography. It is also widely used in the life sciences in fluorescence correlation spectroscopy (FCS) as a method to reveal diffusion dynamics, for example in molecular permeation through a cell membrane, and features prominently as dynamic light scattering in materials science, where it reveals molecular sizes and conformations such as of polymers in solution. But perhaps the most obvious application of intensity autocorrelations lies in studying materials that are specifically designed to emit light in optoelectronic devices. In the above analogy one could ask the seemingly simple question of how many emitting sites exist in a material per unit volume and how these interact with each other. How does the injection of an electron into a material affect light emission? How does excitation energy in the form of an energetically excited electron, or correlated electron-hole pair, move about within a material? Although these seem like obvious questions to ask, surprisingly few reports on the application of intensity autocorrelation techniques to optoelectronic materials are to be found in the literature. Here, we aim to review the existing literature, highlighting the wide range of useful potential applications of the technique and pointing to possible future developments. Before proceeding, it is also worth noting that fluorescence correlation techniques are not limited alone to correlating photon arrival times. Obviously, any optical or spectroscopic observable can be used for correlation – the polarization of the light emitted,[10] the spectrum,[11] or even the excited-state lifetime of the emitter,[12] which determines the photon arrival times. This technique has been employed to reveal a range of intriguing molecular conformational dynamics based on photoinduced electron transfer, such as the folding of protein complexes. But the more involved the spectroscopic observable is, i.e. the more photons are required to determine it, the lower the overall time resolution of the correlation analysis. The fastest time resolution is offered by considering correlations in the arrival times of single photons, i.e. in the intensity autocorrelation.

II. FROM INTENSITY AUTOCORRELATIONS TO PHOTON COUNTING STATISTICS

A. Elements of photon statistics

Planck's postulate stipulates that electromagnetic radiation is quantized in packets of energy $E = h\nu$, where h is Planck's constant and ν the frequency of the radiation. The intensity of light then corresponds to the number of quanta per unit time and area. Because of this quantization, any source of light will show statistical fluctuations in intensity. For a light source emitting perfectly temporally uncorrelated, i.e. random, photons, the distribution of the arrival of these discrete quanta in time is described by the Poisson statistical distribution, and the noise associated with the signal – $\sqrt{N}/N$ with N the number of photons – is therefore referred to as Poisson noise, or shot noise in analogy to the discrete pellets making up the slug of a shotgun. This "noise" is literally familiar to anyone caught out in a rainstorm – the rain drops hitting the ground are all virtually identical, all of the same size and shape, but entirely uncorrelated. A light source, however, may experience additional fluctuations on top of the shot noise, which will show up in the photon statistics. In the simplest case, one may think of a little "*daemon*" flicking the light switch on and off at seemingly random intervals. When the light is passed through the beam splitter of an HBT setup, on short time scales, shorter than the time on which the switch is flicked, the statistics of photon arrival times will then be controlled primarily by the "*daemon's*" activity, whereas on long time scales, the underlying Poisson noise will dominate. In other words, the stream of photons shows a memory of the underlying switching process. The way to analyze such random fluctuations in the signal is to search for correlations in the signal with itself. Figure 2a illustrates the light intensity of a photon source split into two pathways by a beam splitter. The first beam path yields an intensity $I_1(t)$, and relative to this, at an arbitrary delay time of Δt, the second path records an intensity $I_2(t + \Delta \mathrm{t})$. Both signals fluctuate randomly, but clearly retain some of the specific functionality: when the "*daemon*" flicks the switch, the effect will show up in both beam paths. This similarity in the noisy signal of both detectors is quantified by computing the second-order intensity autocorrelation, $g^{(2)}(\Delta t) = \frac{\langle I_1(t) I_2(t+\Delta t)\rangle}{\langle I_1(t)\rangle\langle I_2(t)\rangle}$, which corresponds to the cross-correlation between the two detectors. This relation will tend to unity for randomly fluctuating light intensities. For thermal light, i.e. for blackbody radiation, where the photons are in thermal equilibrium, the "*daemon*" grouping the quanta together is the Bose-Einstein statistics of spin-1 particles: photons "prefer" to stick together, giving rise to an above-unity value of the correlation. The evolution of the correlation function with delay time Δt is shown on the right in Figure 2a on a logarithmic time scale. For low light intensities and quantized sources of light, such as an atom or molecule, the light intensity is no longer a classical continuous function of time.[6] It is therefore more appropriate to consider the arrival times of photons rather than the time variation in intensity. To provide a fixed temporal reference, it is easiest to time the arrival of a photon with respect to a trigger, such as the arrival time of a fluorescence photon of a molecule excited by a laser pulse. This is the underlying principle of time-correlated single-photon counting (TCSPC), but performed in the context of the HBT setup. Figure 2b sketches the fluorescence photon arrival times, marked by red (solid) and green (dashed) vertical bars, in response to a periodic laser pulse (grey) in the two detection channels of the beam splitter. Δt indicates the time difference that the two intensity traces are analyzed against. The autocorrelation function is now simply the count of photon coincidence at a given time difference, $N(\Delta t)$, as plotted in the histogram on the right in Figure 2b, showing “photon antibunching” on short timescales and “photon bunching” on longer timescales. Here, it is helpful to plot the time lag in units of the laser repetition period (e.g. 12.5 ns for the standard femtosecond Ti:sapphire oscillator frequency of 80 MHz). In terms of the underlying physics these two representations – a histogram on a linear scale of $\pm\Delta t$ or a correlation function on a logarithmic scale of $|\Delta t|$ – are basically equivalent, provided that information on the absolute “microtimes” of the photon arrival are retained in the latter, and depend primarily on whether a continuous-wave (CW) or pulsed light source is employed to excite the emitter. Both forms of representing photon correlations are utilized in the following and provide different benefits and drawbacks. To observe photon antibunching under CW excitation, one must choose a very short time binning to resolve the antibunching dip, which has a width in the regime of the fluorescence lifetime of the emitter. Therefore, for typical emitters, a sub-nanosecond time binning has to be used, and this is only possible for very bright and stable emitters so as to acquire a sufficient number of coincidence counts for such a short time binning to build up an antibunching histogram. Another downside is that under CW excitation, the time resolution to observe an antibunching dip is limited by the time resolution of the detectors, which can be as short as 50 ps, e.g. for single-photon counting avalanche photodiodes (PDM Series, Picoquant GmbH). If the fluorescence lifetime becomes significantly shorter than the time resolution of the detectors, no photon antibunching will be observed. However, if the time resolution is sufficient, the benefit will be that the rise over correlation time of the antibunching dip can be resolved, which provides valuable information on the excited-state lifetime and excitation rate.[13] This also means that under CW excitation the shape of the antibunching dip is dependent on excitation intensity, but not the depth of the dip itself.

On the other hand, under pulsed excitation, the feasibility of observing photon antibunchingin photon-correlation measurements is not determined by the detector response time, but by the width of the excitation pulse, which has to be significantly shorter than the fluorescence lifetime of the emitting object studied to as to prevent multiple excitation of the emitter by one single pulse. In addition, the overall photon budget of the emitter is used more efficiently because a time binning in the photon arrival times, which is equal to the repetition period of the exciting laser, is sufficient to observe a photon antibunching dip. Such efficient photon budgeting allows photon antibunching of unstable emitters with a low photon quantum yield to be observed.[14] In this case, the fluorescence lifetime and the excitation rate cannot be extracted from the antibunching histogram. However, the fluorescence lifetime can easily be determined by using conventional TCSPC, and therefore the main focus of the work presented here lies on pulsed excitation, which is more universal in terms of the materials classes it can be applied to. Under ideal conditions, i.e. when no background is present, the photon antibunching histogram under pulsed excitation is not dependent on the excitation rate. Obviously, the background cannot be neglected in real experiments and the lower the signal-to-background ratio becomes, the stronger the impact of background photons on the photon antibunching histogram, which will increase the antibunching dip. This phenomenon can be corrected for and is discussed in detail in Ref. 15.

It is also helpful to note that, obviously, an intensity autocorrelation can simply be calculated from the temporal evolution of the fluorescence light intensity as measured by a single photodetector.[16] This approach will be limited by the "dead time" of the photodetector used, i.e. the time required to build up the potential difference again to generate an electrical pulse upon photon arrival, and may also be obscured by electrical ringing effects and optoelectronic afterpulsing phenomena, particularly in the case of avalanche photodetectors.[17] It is also important to realize that the quality of the photon correlation function or the photon coincidence histogram will depend on the overall number of photons detected in total. This number may be limited by the photostability of a single molecule in a real experiment. It is therefore possible to simply add the measurements of photon counts from different single molecules together to improve the overall quality of photon statistics, provided that each single molecule behaves in a similar fashion. This addition of photon counts is not equivalent to averaging over an ensemble because each single photon is still detected individually and, in principle, sub-populations of molecules can be selected.

Although the elementary aspects of luminescence photon statistics relating to the quantized nature of light emission are reasonably straightforward to appreciate, the development of a full quantum-optical theory of photon statistics from a real electronic emitter rather than an idealized two-level system remains challenging.[18] Real-world light sources will show spectral diffusion giving rise to additional dynamics that need to be accounted for in describing the underlying light-matter interaction. In semiconductors, it is common to resort to the generalized optical Bloch equations for this problem, whereas in atomic quantum optics, a stochastic Liouville approach is often used.

It is also worth mentioning that the MMI and HBT correlation techniques can be combined to give photon-correlation Fourier spectroscopy.[19] The method brings together the spectral resolution acquired due to the interference in an MMI configuration with the fast time resolution inherent to single-photon counting, and therefore allows very fast spectral fluctuation events to be tracked. While we shall not dwell further on this technique, its merit lies in the fact that it can determine a relation between the so-called homogeneous linewidth of an emitter and the excited-state lifetime. The lifetime of a transition limits the linewidth of the transition, i.e. the uncertainty in the emitted photon energy, by the Heisenberg uncertainty principle. The homogeneous linewidth therefore corresponds to the coherence time. Coherent emission from perovskite quantum dots was recently reported in that the extraordinarily long single-photon optical coherence time of some 80 ps, determined by photon-correlation Fourier spectroscopy, made an appreciable fraction of the rather short excited-state radiative lifetime of 210 ps.[20] Such coherent single-photon light sources could offer a building block for quantum-coherent information processing assemblies.

B. Material properties responsible for photon bunching and antibunching

Since light is fundamentally quantized, the generation of light will also be controlled by the underlying quantum nature of the light source. This realization applies to any optoelectronic material, a conventional crystalline inorganic semiconductor, a semiconductor nanostructure, amorphous semiconductors, wide-gap insulators with color centers, van-der-Waals materials, and even, under certain conditions, films of metal nanoparticles. In a bulk semiconductor it may be a defect in the lattice, a broken bond or a dislocation or impurity in the crystal, which results in a degree of discreteness in the emission. But the discontinuous nature of light generation is most vividly realized by considering organic semiconductors. An organic light-emitting diode (OLED), for example, consists of a thin layer, often only a few tens of nanometers in thickness, of evaporated or spin-coated material. In many cases, light generation is monomolecular in nature: a dilute solution of the organic semiconductor material will show virtually the same fluorescence spectrum as the electroluminescence from the solid film. Light is generated by electron-hole recombination in the film, which gives rise to the formation of a monomolecular excited state. This molecular excited state constitutes the aforementioned "*daemon*" which controls the flow of photons. As sketched in Figure 3a, a fluorescent molecule can, to a very first approximation, be thought of as a three-level system with a singlet ground state S_0 and a singlet excited state S_1. Transitions can be driven from $S_0 \rightarrow S_1$ at an excitation rate of k_{exc}, and the excited state may decay radiatively with a rate k_{r}, emitting light of energy $h\nu$. In the singlet excited state, a conversion of the spin of the electron may occur, giving rise to intersystem crossing (ISC) to the triplet excited state T_1 at a rate of k_{ISC}. This triplet state is generally dark in that it is not dipole-coupled to the ground state, and decays slowly non-radiatively with a rate k_{T}, undergoing a further spin transition in reverse-ISC. These transitions between "bright" singlet manifolds and "dark" triplets can be thought of as quantum jumps,[9] in analogy to incoherent transitions between different manifolds of an atom driven under a double-resonance excitation,[21,22] giving rise to random telegraph noise in the luminescence signal.[23] The corresponding TCSPC signals on the two HBT detection channels are illustrated in Figure 3b, with the periodic laser pulse marked in grey. Single photons are detected at a certain delay time t_{det} after the time of excitation t_{exc} with a probability $P(t_{\mathrm{det}} - t_{\mathrm{exc}}) \propto \exp(-\frac{t_{\mathrm{det}}-t_{\mathrm{exc}}}{\tau_{\mathrm{LT}}})$, with τ_{LT} the lifetime of the molecular excited state. While the molecule cycles between singlet ground and excited state, it remains "on" (i.e. bright) with regard to light emission and absorption, shown in the temporal evolution of the emitted light intensity in Figure 3a. ISC disrupts this cycle, so that the molecule turns "off" and is no longer able to emit light (i.e. it becomes dark), and remains in this state for the duration of the triplet lifetime, k_{T}^{-1}, which corresponds to the rate of reverse intersystem crossing from the triplet excited state to the singlet ground state, $k_{\mathrm{rev.\ ISC}}$. The intensity autocorrelation of this intermittency is plotted on the right of Figure 3a, showing a photon "bunching" peak at short delay times Δt, which falls off exponentially (black line) with a characteristic decay time $\tau_{char.}$, i.e. $g^{(2)}(\Delta t) = Ae^{-\frac{\Delta t}{\tau_{\mathrm{char.}}}} + 1$, with A the bunching or correlation amplitude. Note that the logarithmic plot using a logarithmic x-axis (i.e. the Δt-axis) gives rise to a stretched step-like form of the exponential correlation function.

A common way to confirm that the molecular triplet state is indeed responsible for the intermittency in the luminescence is to expose the sample to oxygen. Oxygen has a paramagnetic ground state and readily quenches molecular triplet excitations, thereby giving rise to pronounced luminescence bursts on the single-molecule level until irreversible photobleaching sets in.[24,25]

Obviously, the molecular triplet excited state is not the only possible source of photon bunching.[26] Charge-transfer states may also form, which can render the molecule non-emissive, potentially for times significantly longer than the lifetime of the triplet. A material system studied particularly extensively with regards to the origin of intermittency in the stream of photons in luminescence are colloidal nanocrystal quantum dots.[27] In these materials, the distribution of "on" and "off" times in the luminescence is often found to follow a power-law distribution[28] rather than the exponential functionality associated with a well-defined lifetime of a single dark excited state.[27,29,30] A broad range of experimental techniques spanning single-particle Stark spectroscopy,[31,32] single-particle spectroelectrochemistry,[33] and optically detected magnetic resonance spectroscopy[34] have been able to associate this intermittency with charge trapping on the surface of the nanocrystals. Interestingly, in a surprising analogy to triplet quenching in molecules, it was shown that the power-law exponents of luminescence blinking of nanocrystals, and hence of the intensity autocorrelation function, can be modified by exposure to air, presumably because of an oxidation reaction facilitated by the ambient moisture.[35] This effect is suppressed by embedding the nanocrystal quantum dot in a thick semiconductor shell of larger band-gap material. In fact, power-law blinking dynamics, i.e. a power-law shape of the photon bunching signal, may also arise in single molecules when charge-transfer processes occur.[36]

Intermittency effects not entirely dissimilar to those found in semiconductor nanocrystals have also been observed in self-assembled quantum dots grown by vapor-phase epitaxy.[37] These materials are brighter and more stable and can be studied for very long times. $g^{(2)}(\Delta t)$ measurements spanning eleven orders of magnitude in time have been reported for these compounds, revealing intricate structures that point to several different dark states with distinctly different lifetimes.[38]

Since the duration of the fluorescence intensity trace shown in Figure 3a is much longer than the pulse period of the exciting laser, the excitation conditions may be viewed as being quasi-continuous. However, one may also treat each laser pulse individually and plot the intensity autocorrelation as a photon coincidence histogram, i.e. as a function of interpulse temporal spacing Δt as shown in Figure 3b. On the shortest timescales, for $\Delta t = 0$, the photon correlation is dominated by the discreteness of the single-molecule fluorescence. The photon cannot impinge on both detectors at the same time, and so photon antibunching is seen as the photon coincidence drops to zero: $g^{(2)}(\Delta t = 0) \to 0$, limited only by the finite signal-to-noise ratio of the detection.[15]

These sorts of effects on the photon statistics in fluorescence were studied extensively in the 1970s and 1980s in atomic systems, in the 1990s in single molecules and subsequently in quantum dots and other nanoparticles. While they are appealing to visualize the direct link between the discrete nature of light and matter, they are limited in that, ultimately, even large quantum dot structures behave as artificial atoms and therefore the underlying physics is rather similar in all these examples.[39-41] Mesoscopic objects in the solid state, however, allow us to study the interaction between multiple two- or three-level-system-like structures to reveal dramatic effects on the photon statistics, which generally do not emerge in purely atomic analogues.

C. Incoherent versus coherent dipole-dipole coupling: from exciton-exciton annihilation to superradiance

As noted, one may break down an organic semiconductor film, for example in an OLED, into the smallest discrete light-emitting entities – the single molecules. But what if we consider two or more of these single entities linked together, i.e. interacting with each other, in the first step to the bulk film of the material? Two important effects can occur: incoherent coupling between the two excited states by resonant energy transfer from one to the other; or coherent coupling, where the transition dipoles of each of the molecules either add up or subtract from each other.

Many examples of multichromophoric objects were studied in the late 1990s and early 2000s, which exhibited “collective”[42] behavior in that their fluorescence was found to switch on and off randomly on the single-molecule level: blinking, a signature of luminescence from a single emitting species, can arise from larger objects containing multiple emitters, such as dye-decorated dendrimer structures[43] and long conjugated-polymer chains.[44-46] In the simplest case, this blinking is merely a signature of efficient excited-state quenching through interchromophoric energy transfer to a transient trap state, such as a photoradical. Conventional blinking due to intermittent photoquenching on its own does not necessarily tell us anything about the underlying photon statistics since it does not imply that when the multichromophoric molecule emits, it will emit precisely one photon at a time. All the greater the surprise then, that ever larger synthetic and natural objects were found to show signatures of non-classical photon emission.[42,43,47,48]

Figure 4 illustrates an important experiment that was performed by Hofkens *et al.* to probe exciton-exciton annihilation between two like chromophores.[49] Two perylene dyes are linked to a rigid conjugated oligomer or polymer chain, used to provide a well-defined separation in space, corresponding to three, six or, on average, 56 repeat units as indicated in Figure 4a. Three primary photophysical processes are conceivable within this molecule. The first is, depending on the spacing between the two chromophores shown in Figure 4e, trivial energy transfer either from 1 to 2 or from 2 to 1. This effect will happen if the excitation fluence is such that, on average, only one of the two chromophores is excited. Such energy transfer can be described by incoherent dipole-dipole coupling, giving rise to a Förster-type resonance fluorescence energy transfer (FRET). In such a “homo-FRET” constellation, where donor and acceptor are indistinguishable in energy and energy transfer can occur in either direction as indicated in Figure 4e, dipole-dipole coupling can be visualized, for example, by studying the fluorescence polarization anisotropy and the polarization memory between excitation and emission. The strength of FRET depends both on the spacing between the dyes and on the spectral overlap between the ground-state absorption and the emission of the dyes, shown in Figure 4b. If only this mechanism were active, the bichromophoric molecule should not show single-photon antibunching since the two chromophores can emit light independently of each other, even though they can exchange excitation energy (panel h). However, there is also a second pathway for energy transfer to occur, which becomes more important as the excitation density increases: excited-state absorption by one of the two chromophores (panels c, f). When one of the chromophores enters the excited state, a new absorption transition is opened since the molecule can now transition from the S_1 state to higher-lying singlet states S_n. In this case, where both chromophores 1 and 2 are in the excited state, chromophore 1 may pass its excitation energy to chromophore 2. Chromophore 1 then becomes deactivated, and chromophore 2 undergoes excitation to a higher-lying state, as sketched in Figure 4f, from which rapid internal conversion to the first excited state can occur, dissipating the excess excitation energy as heat. Such a mechanism, referred to as singlet-singlet annihilation,[50] is rather analogous to the well-known Auger recombination in atomic and semiconductor physics. The mechanism is remarkably efficient since the excited-state absorption spectrum, measured by transient absorption spectroscopy, has a spectral overlap with the chromophore emission spectrum comparable to that of the chromophore absorption in the conventional homo-FRET process. The consequence of this singlet-singlet annihilation is that the bichromophoric molecule shows deterministic single-photon emission – photon antibunching as illustrated schematically in Figure 4i.

Double excitation of the molecule, so that both chromophores 1 and 2 are in the excited state, depends on the fluence in excitation and is generally a rare event. However, it is precisely these events, that the HBT setup is responsive to: it reports on the conditional probability of detecting the second photon at time $t + \Delta t$ after the first one was detected at time t. As such, it is directly sensitive to the process of singlet-singlet annihilation, which prevents two photons from being emitted as the result of a single excitation pulse, thus leading to photon antibunching.

The third possibility, shown in Figure 4d, g, is for one of the two chromophores to enter a long-lived dark triplet state, i.e. to disrupt the cycling between S_0 and S_1 states. In this case, the triplet absorption spectrum, again measured by transient absorption spectroscopy, perfectly overlaps the chromophore emission spectrum. The singlet excited state of chromophore 1 will pass its energy to the triplet excited state of chromophore 2, raising it to a higher-lying triplet state T_n by means of resonant dipole-dipole coupling, i.e. FRET. The triplet will relax down to the lowest excited state T_1 by means of internal conversion, and the result will be that neither chromophore of the molecule emits light. This singlet-triplet annihilation[51] is rather similar to the Auger recombination observed in some semiconductor nanostructures, which can also be spin dependent. The consequence will be that the entire molecule turns dark, even though only one of the two chromophores is in the dark state. The multichromophoric molecule will then show photon correlations reminiscent of those of a single dye molecule, with both photon antibunching and photon bunching (Figure 4j). In other words, a study of the photon correlations offers direct insight into the strength of singlet-singlet and singlet-triplet interactions, which, because these are resonant dipole-dipole coupling processes, depend on spectral overlap of absorbing and emitting species and the separation in space. By analyzing the photon statistics of a bichromophoric model system undergoing stepwise photobleaching for the different steps of photobleaching, and employing Monte-Carlo simulations to account for the conformational diversity in interchromophoric energy transfer, Fückel *et al.* succeeded in arriving at a quantitative estimate of the singlet-singlet annihilation rate.[52] In fact, the evolution of photobleaching with time in a multichromophoric molecule can quite generally be used to probe the delocalization of the exciton wavefunction, as different chromophores in a strongly-coupled multichromophoric molecule bleach over time, changing the excitonic coupling.[53] As we will discuss further on, photon statistics can therefore be used to estimate the mesoscopic size in volume of a unit of an organic-semiconductor film from which light emission occurs, which can span some 1,000 nm^3. Both singlet-singlet and singlet-triplet annihilation occur in organic semiconductors and can limit device efficiency.[54] In addition, both species, singlet and triplet excitations, may also interact with trapped charge carriers in the molecule, which typically leads to quenching.[55,56] The photon correlation measurement can then contain information on the lifetime and dynamics of such charge species.[57]

Under incoherent dipole-dipole coupling, the two chromophores remain distinguishable: the excitation energy resides either on the one or the other, or on both. Alternatively, coherent dipole-dipole coupling can occur, in which case the two chromophores become indistinguishable because they basically add up to form a new excited state: depending on their relative orientations, the transition-dipole moments of the two molecules add up or subtract. While this effect is well known in molecular photophysics and is referred to as either “Jelly” (J)-type or “hypsochromic” (H)-type aggregation, discussed in detail below in Section VII, its effect on the photon statistics is challenging to study: one needs precisely two chromophores placed at a well-defined short distance to each other, in a photostable environment. This was achieved first by Hettich *et al.* as illustrated in Figure 5a, using a combination of atomic-force microscopy techniques and the electric-field-induced Stark shift to drive the molecules into and out of resonance.[58] For simplicity, we consider only the singlet states of the molecule. Each molecule has a ground (g) and excited (e) state of slightly different energy (Figure 5b). Using the Stark shift, the two transitions can be driven into resonance. Under suitable alignment of the transition dipoles of the two dye molecules, the degeneracy in the excited states is then lifted. The one-photon transition is suppressed for the two molecules and a two-photon transition opens up, where both molecules are excited together. The crux of the experiment is to be able to tune the degree of coupling between the two dipoles, which is done with the help of an electric field, exploiting the Stark shift. When the two molecules are uncoupled (Figure 4c), conventional photon antibunching is observed, shown here under CW excitation and hence as a continuous second-order correlation function $g^{(2)}(\Delta t)$ rather than a photon coincidence histogram. When the two molecules are shifted into electronic resonance, the strength of dipole-dipole coupling increases as does the splitting of the excited states: the two-photon transition becomes possible so that both molecules are excited simultaneously by the new transition seen in the PL excitation spectrum inset in Figure 5d. These experiments can only be carried out at cryogenic temperatures where the emission spectra are extremely narrow, as are the corresponding excited-state absorption spectra. Singlet-singlet annihilation effects such as those in Figure 4 are therefore suppressed. Instead, superradiance occurs:[59] both dye molecules emit a photon at once, giving rise to the photon bunching seen in Figure 5d. The solid lines show exponential fits to the photon correlation curves, which provide a measure of the excited-state lifetime. This lifetime clearly decreases for the case of superradiance compared to the isolated molecule, a direct signature of the effect.[60] Increased radiative rates are generally considered desirable in optoelectronic applications because they imply a smaller role of non-radiative decay of excitation energy, thus raising overall quantum yields. While this demonstration of superradiance in two dye molecules embedded in a molecular crystal constitutes a rather specific example, it offers hope for exploitation of the effect in more real-world situations. Recently, single-photon superradiance was also observed in electroluminescence from molecular chains placed in a plasmonic nanocavity by molecular manipulation using a scanning-tunneling microscope (STM).[61] In this case, superradiance in the tip-induced single-photon electroluminescence was identified from the departure of the photon antibunching fidelity expected for single-photon emission rather than in a direct photon-bunching signal.

In a further direction, perovskite-based quantum dots have been developed with interesting optical characteristics. While perovskites are best known for their application potential in photovoltaics, quantum dots have been shown to be very bright and photostable, and versatile in terms of processing characteristics. It is possible to couple quantum dots to each other in a solid without losing the features of the individual quantum dot. Figure 6 illustrates results from Raino *et al.* on such materials,[62,63] isolated ensembles of quantum dots dispersed in glass thin films or closely packed aggregates arranged in quantum-dot superlattices. Panel a shows photoluminescence (PL) spectra of the two samples, recorded at a temperature of 6 K. The superlattice structure consists of two distinct features, one at lower energy (red, 2.3 eV), which is assigned to coupled quantum dots, and one at higher energy (blue, 2.375 eV) similar in spectral shape and position to the isolated uncoupled dots. As discussed in Section VII, this spectral red shift and narrowing is a classic signature of “J-type” aggregation in molecules, observed here in quantum dots: the transition-dipole moments add up. This is a bit like extending the length of a bathtub and slashing the water to and for in it: the longer the bathtub – the added-up transition-dipole moments – the lower the resonance frequency but the lower also the damping due to friction on the sides of the bathtub since more of the water is in the volume rather than on the surface. The distribution of resonance frequencies, i.e. the resonance spectrum, narrows with reduced damping. The effect of this coherent dipole-dipole coupling on the photon statistics in Figure 6b is quite spectacular: whereas the ensemble of uncoupled quantum dots, selected spectrally from the PL of the quantum-dot superlattice, show a flat intensity autocorrelation, as would be expected for an ensemble of quantum emitters, the red-shifted PL exhibits clear signatures of photon bunching due to superradiance, or more specifically superfluorescence in this case. In addition, the red feature shows a fluence-dependent PL decay, accelerating with increasing excitation density as more and more quantum dots enter the excited state. The PL lifetime of the coupled quantum dots drops to almost a third of that of the uncoupled quantum dots. It is possible to observe such effects in perovskite nanoparticles because of the comparatively narrow transition lines, the high degree of photostability and the exceptionally large transition-dipole moments that make these materials so appealing for solar light harvesting in photovoltaic applications.

Other interesting material systems also exist, which exhibit signatures of superradiance and super-Poissonian photon statistics in light emission, i.e. $g^{(2)}(\Delta t) > 1$, even at room temperature. A recent example focused on nitrogen-vacancy centers in diamond nanocrystals.[64] It is worth mentioning that Dicke-type superradiance can occur in any ensemble of two-level systems coupled by the light field,[59] and may even arise in magnetic-dipole transitions that do not give rise to fluorescence. In such a case, superradiant behavior can show up in the form of spin-dependent charge transport, most notably in OLEDs.[65,66] Such spin-dependent transport may in turn influence excitonic fluorescence properties by charge-exciton interactions.[67]

III. APPLICATIONS OF PHOTON STATISTICS ANALYSIS

In the following, we introduce some of the different research fields where the analysis of luminescence photon statistics plays an important role. Best known perhaps are the field of the life sciences, in particular the ubiquitous technique of fluorescence correlation spectroscopy (FCS),[68-70] as well as the field of quantum information science, but there are several partly connected areas of application which are also worth mentioning.

A. Life sciences

The discussion so far has focused on immobilized emitters of single quanta, but if an object emitting a single light quantum – such as a molecule – is known to be responsible for the light detected, it is possible to use the luminescence correlation function to extract information on the spatial dynamics of the object.[71-73] In dilute solution, single molecules will diffuse in and out of the focus of a microscope. This diffusion process is then analogous to the effect of the aforementioned "*daemon*", the switching "on" and "off" of the photon stream. Care has to be taken to avoid or account for a build-up of the intrinsic dark state of a molecule, the triplet, which becomes particularly prevalent at the high excitation densities used in a confocal fluorescence microscope.[74] The triplet can be quenched by surrounding it with molecular oxygen: the ground state of O_2 is paramagnetic and so triplet excitation energy can transfer to O_2, returning the dye molecule to the ground state. The intermittency in the fluorescence dynamics of the dye molecule is then only related to the diffusion and not to the intrinsic dark states. Obviously, merely studying Brownian diffusion in solution is of limited interest, but it is not obvious how particles diffuse in confined geometries, such as on the surface of a cell. FCS has been crucial in resolving many of the fundamental messaging processes in cellular biology such as the molecular motors responsible for muscle movement – kinesin moving along actin microfilaments.[75] The techniques of biochemistry allow individual molecular constituents of the cell to be labelled with fluorophores so that they can be tracked individually. An unbound dye will show random Brownian diffusion in three dimensions whereas a dye bound to a motor protein will exhibit unidirectional kinetic motion. The result upon binding of a fluorophore to such a structure is a dramatic reduction in the apparent "on" time of the fluorescence as well as the departure of the $g^{(2)}(\Delta t)$ functionality from a purely diffusional form as discussed below. For example, stretched exponentials may emerge as well as power-law functionalities.

The high timing resolution inherent to FCS measurements also allows the observation of photon antibunching of diffusing molecules in solution. The antibunching signal contains important information on intermolecular fluorescence quenching dynamics. The approach has been used to extract a full microscopic picture of the complex photoquenching kinetics in common organic dye systems, e.g. the interaction pathways of rhodamine-110 with aniline,[76] or of Atto-655 with the amino acid tryptophan.[77] Further broad application potential of single-molecule single-photon correlation techniques has also been demonstrated in the unravelling of the different photophysical and photochemical processes active in photosynthetic systems.[78]

While the FCS technique was already well established in the 1970s, it has attracted renewed interest because of the combination with superresolution fluorescence microscopy techniques, which allow a combination of the high time resolution inherent to photon timing and correlation techniques with a high spatial resolution.

B. Superresolution fluorescence microscopy

Any optical imaging process is limited in spatial resolution by the wavelength of the radiation used. One underlying idea of superresolution microscopy is to enhance the spatial resolution beyond this diffraction limit by confining the spatial extent of the light under consideration. The original idea, already formulated almost a century ago, involved shrinking the size of a light source and scanning this source over the sample.[79] In practice, this is achieved, for example, by stretching an optical fiber until it becomes thinner than the wavelength of light. The increased spatial resolution comes at the expense of reduced light throughput since it is only the nearfield of the light which couples to the surface of the sample, limiting the imaging capability to two dimensions. In the past two decades, many different methods for superresolution far-field three-dimensional imaging were developed, which are covered in numerous in-depth review articles.[80-84] For this reason, we will only briefly touch upon the techniques in this context and highlight some specific examples of relevance with regard to the general concept of the analysis of fluorescence photon statistics. Many techniques rely on constraining the region of space from which fluorescence emerges. Such a constraint can be achieved by exploiting a saturable non-linear optical process such as stimulated emission, and superimposing two light beams of different shapes on the sample.[80] The advantage of this technique of stimulated emission depletion (STED) is at once its main disadvantage: high light intensities are involved. Alternatively, the intrinsic fluorescence intermittency of individual light sources, the "blinking", may be used to localize the single emitters.[85] Whenever the "*daemon*" flicks on one of the emitters, the two-dimensional diffraction-limited distribution in light intensity recorded by the microscope changes slightly. Analysis of these dynamics allows stochastic reconstruction of the spatial distribution of the individual fluorophores with subdiffraction resolution. Rather than using random blinking, photoisomerization can be exploited to switch the individual fluorophores on and off. In combination with non-linear excitation, such as through two-photon absorption, the effective cross-section of which depends quadratically on light intensity, three-dimensional spatial resolution can be achieved.

The high fluences involved with STED make the technique ideal for a combination with FCS as pioneered by Eggeling *et al.* with the intention of tracking diffusive processes on subdiffraction length scales,[86] such as the diffusion of single lipids on the plasma membrane of a cell *in vitro*. Figure 7 illustrates the underlying principle of the methodology. A blue pulsed excitation beam, limited in spatial extension by diffraction, is used to excite the fluorophores. A second red pulsed beam is superimposed to deplete part of the excited fluorophores by stimulated emission. The blue beam has a spatial intensity profile of a two-dimensional Gaussian, corresponding to the lowest-order spatial mode of the light wave. The red beam is designed to originate from a higher-order spatial mode so that the intensity profile has the shape of a donut, even though the beam is still limited in its overall extension by diffraction. The combination of excitation and depletion pulses, however, means that the effective area of molecules that remain in the excited state and can fluoresce spans merely 20-40 nm across, provided that the fluorescence and stimulated emission of the molecules can be separated spectrally. The FCS technique determines the average transit time of molecules through the effective excitation volume, sketched in Figure 7b. If the concentration of molecules is sufficiently low so that the apparent brightness becomes discrete, fluctuations in the intensity will be observed as a function of time. Computation of the intensity autocorrelation function (ACF) then gives a distinct and common functionality, which, in a sufficiently homogeneous system, is described by $g^{(2)}(\Delta t) = \frac{1}{N}\left(1 + \frac{\Delta t}{\tau_{\mathrm{D}}}\right)^{-1} + 1$ for two-dimensional diffusion with a characteristic time constant relating to the molecular diffusion, the diffusion time (more generally referred to as the lag time) τ_{D}, and the average number of emitters N inside the confocal observation volume.[87] The relation arises since it is mainly intensity fluctuations due to motion in the $x - y$-plane which are detected. The parameters allow an effective diffusion coefficient of the analyte in the solution to be determined. A typical cellular membrane, sketched in Figure 7c, is quite heterogeneous in space, consisting of many different domains. Whereas conventional diffraction-limited confocal optical excitation averages over many domains, the STED technique can select one single domain where the lipid diffusion is then tracked. Rather than scanning the subdiffraction excitation spot over the cell membrane, the spot size is varied continuously to probe the different interaction mechanisms of the lipids with the membrane (panel d). The trivial case is the situation of a free molecule (purple), where the diffusion coefficient is entirely independent of the volume probed. In contrast, a trapped molecule (green) will show an increase in effective diffusion coefficient with increasing spot size: the larger the spot size, the greater the apparent distance of diffusion when it becomes untrapped and induces a PL intensity fluctuation. The opposite is true for a molecule that becomes retrapped again, i.e. undergoes a hop from one domain to another (blue). Finally, a molecule that is confined within one extended domain will behave like a free particle in terms of its diffusion on short length scales (yellow) but like a trapped one on larger scales.

Fat uptake by a cell is controlled by cholesterol. Such cholesterol-mediated interactions with lipids can give rise to the formation of nanoscale domains on the cell membrane, which are crucial to the interaction of the cell with the environment. The experiments by Eggeling *et al.* revealed that different types of lipids undergo different interactions in the cholesterol-mediated complexes formed on the surface of the cell: sphingolipids and lipid-anchored proteins become trapped for timescales extending up to 10 ms on tiny length scales covering less than 20 nm, whereas phosphoglycerolipids do not and remain free to move. The fact that different fats do not show the same diffusivity on the cell surface is crucial to understanding the metabolism of different compounds. The example illustrates the utility of combined high temporal and spatial resolution in studying biomolecular function.

The technique of FCS exploits the phenomenon of photon bunching, the fact that the photons arrive in interrupted streams. But it is also possible to exploit the quantum-nature of light emission, the photon antibunching, as a method complementary to STED or stochastic image reconstruction to beat the diffraction limit in fluorescence imaging.[88-90] Two emitters spaced apart less than approximately half the wavelength of the light they emit will appear inseparable in the spatial intensity profile, unless their individual intensities can be modulated in a controlled fashion. Figure 8a shows a fluorescence microscope image of two nitrogen-vacancy (NV) centers in a diamond crystal. These color centers are particularly stable and suitable for long-term imaging. The image appears elliptical in shape since the off-diagonal extension of the spot is limited solely by diffraction whereas the on-diagonal spread relates to the spacing of the two light emitters. Because this spacing is smaller than the diffraction limit, the two emitters cannot be separated in space unless they can be turned on and off in a controlled manner. However, it is possible to determine whether the detected light intensity at any given coordinate in the image results from either one or both of the NV centers by determining the intensity correlation function $g^{(2)}(\Delta t)$: if only one of the emitters is active in the blurred spot, photon antibunching will be seen as $g^{(2)}(\Delta t = 0) \rightarrow 0$. Figure 8b illustrates precisely this effect, measured at the three different positions marked by the circle, and the cross and plus sign, respectively. At the central position (∘), both diamond color centers emit so that $g^{(2)}(\Delta t = 0) \approx 0.5$; at either emitter positions (×, +), only one of the two centers emits so that $g^{(2)}(\Delta t = 0) \approx 0$. Such diamond NV centers are very photostable and can be studied for almost indefinite timescales, allowing photon statistics of effectively arbitrary quality to be acquired. With this approach, it was possible to determine a spacing between two emitters of down to 8.5±2.4 nm – a spatial resolution roughly 40-fold better than what is achievable with conventional fluorescence microscopy techniques.

Obviously, acquiring information on the fluorescence photon statistics necessitates long integration times and therefore a high degree of photostability, which is offered by diamond NV centers. However, the technique could recently also be applied to more conventional problems of bioimaging by using semiconductor quantum dots as the active fluorophores. Figure 9 shows fluorescence images of labelled microtubule cell samples, with the white boxes marking the close-up region of the microtubule branching shown in the inset. The images in panel a were obtained by conventional confocal scanning fluorescence microscopy and appear blurred. When taking the $g^{(2)}(\Delta t)$ measurement into account as a further contrast-enhancing parameter (panel b), more structure is resolved in the image. This increase in resolution is remarkable in that, unlike in a comparison to STED or stochastic reconstruction microscopy, both images rely on exactly the same microscopy technique and the same photon flux, but the "quantum image scanning microscopy" (Q-ISM) additionally takes into consideration the photon correlation and the discrete nature of fluorescence.

To fully exploit the capabilities of superresolution imaging using fluorescent probes it is crucial to understand the underlying photophysics of the materials, in particular in the context of biological problems.[91]

C. Quantum information science

The research field that has been built on the discrete nature of light generation – and, potentially, detection – is quantum information science. Vast research efforts exist to generate single photons or photon pairs in a controlled fashion.[92] Since detection of a photon destroys it, optical communication by single photons provides a failproof means of identifying interceptions in the communications channel: as implied by the uncertainty principle, in the measurement of a quantum state it is not possible to determine all relevant properties at the same time, so that it is impossible to recreate an identical quantum state, thus making intrusion into the communication channel inherently traceable.[8] The simplest design in quantum communication may be a light source which emits precisely two photons at a time. Due to the physical conservation laws, these two photons will be quantum-mechanically entangled, for example with regards to their polarization: if the one photon is left-hand circularly polarized, the other one must have right-hand helicity. When the two photons pass through a beam splitter, it is impossible to predict which polarization will split into which direction. The polarization only becomes known upon detection, but it becomes equally known for both propagation directions. Any tampering with the photon during propagation will destroy this entanglement, which can be monitored by a second communications pathway on a classical channel. Conventional production of entangled photons occurs by parametric down-conversion, the opposite process of optical second-harmonic generation. Such a pair-generation procedure is still classical in that it forms classical photon-number states whose autocorrelation follows Poissonian statistics: photons arrive at non-deterministic times at the detector, but their spacing in time follows the Poisson distribution. Deterministic non-classical light sources, in contrast, are true quantum emitters exhibiting "sub-Poissonian" statistics, i.e. photon antibunching. Many examples involving single atoms,[93-95] molecules,[13,96-98] quantum dots,[41,99,100] color centers in crystals,[101] even carbon nanotubes,[102,103] etc. have been reported, but these are of limited scalability and hard to integrate into existing optical communications infrastructure. Much progress has been made, however, in the field of deterministic single-photon light-emitting diodes (LEDs).[104,105] Figure 10a illustrates such a device structure. Besides integrating an electrically addressable quantum emitter, in this case an InAs quantum dot, one has to ensure that the light is emitted from the device as quickly as possible and can be efficiently coupled into an optical fiber. These two requirements are met by growing the LED structure within an optical microcavity which ensures directional emission and also enhances the radiative rate of the optical transition by the Purcell effect: the cavity discretizes the optical density of states, increasing the electric field strength and thus the strength of light-matter interaction according to Fermi's Golden Rule. The top aperture of the device, defined by the aluminum contact, is chosen such that precisely one quantum emitter emits light in the device. However, a semiconductor quantum dot is a complex mesoscopic structure in that it can support multiple different correlated electronic states. Different excitonic species dominate at different driving strengths of the device as shown in Figure 10b. For low currents, three peaks are seen, of which two can be assigned to the neutral exciton X and the positively charged exciton, the trion X^+, respectively. Under these conditions, the trion appears positively charged because the quantum dot is embedded in a semiconductor with a surplus of holes, p-doped GaAs. As the drive current increases, the X^+ transition disappears and the negatively charged trion X^- emerges. Crucially, however, the neutral biexciton transition X_2 is found to increase quadratically in intensity with carrier density, becoming the dominant species at the highest drive currents. This biexciton can serve as a source of entangled photons since it tends to decay by emitting two photons at once. The resulting photon statistics of the LED under pulsed electrical driving at a frequency of approximately 80 MHz are shown in Figure 10c for the two dominant exciton species. Clearly, $g^{(2)}(\Delta t = 0)$ is larger for the X_2 line than for the X transition, which can be separated by means of a spectrometer: the photon coincidence rate is greater for X_2 than for X. With careful engineering, it has been possible to lower the jitter in the light emission – the random time interval between the voltage pulse applied to the LED and the photon generation – to below 100 ps. In this way, the speed of the LED can be raised dramatically to operate at up to 1.07 GHz. Figure 10d shows the time-resolved electroluminescence intensity, which closely follows the drive voltage on the sub-nanosecond timescale. The resulting photon correlation is shown in Figure 10e. Since the LED in this example is driven by a continuous sinusoidal function rather than by a pulse sequence as in the case of panel c, the correlation amplitude does not drop to zero. Such devices show a high fidelity for the deterministic electrical generation of entangled photons as is verified by considering the photon polarization state in the autocorrelation.

In recent years, a variety of single-photon LEDs have been demonstrated, most notably based on the NV centers in diamond, which has to be highly doped to enable charge injection and transport.[106,107] Some devices operate at elevated temperatures, e.g. based on CdSe/ZnSSe/MgS quantum dots,[108] and even at room temperature. LEDs based on carbon nanotubes have also been reported,[109,110] using single solution-processed colloidal nanocrystal quantum dots,[111] and even incorporating single molecules,[112] although the latter suffer substantially from instabilities and low brightnesses. Besides applications in quantum communication, such single-photon sources can also serve well as compact light source for on-chip optical interconnects, a concept whose utility has been explored particularly in the context of carbon nanotubes, which are readily integrated in silicon-based electronics. There are also concepts for using photons and photon pairs generated from single-photon sources for quantum computing,[113] although such an application requires a secondary material to mediate interactions between the quanta.

Although the emphasis of materials systems studied for applications in quantum-information science shifts over time, it is worth noting that some material systems have experienced a bit of a “renaissance” in terms of interest when a particular seemingly insurmountable obstacle is overcome. Single molecules, for example, which were studied in the early 1990s as single-photon sources were generally discarded as potential two-level systems because of the inherently strong coupling to vibronic modes, making them effectively multilevel systems. This limitation can now be overcome by placing the single molecule in an optical microcavity of high quality factor of order 10^5, allowing the molecule to behave as a coherent two-level system.[114] Since the object is so small, detrimental scattering is reduced and extinction of 99 % of a laser beam is observed along with super-Poissonian "super-bunched" light with $g^{(2)}(\Delta t) > 2$. This extraordinarily high extinction for a single two-level system is of importance because it allows different distant quantum systems to be coupled to each other.[114]

D. Semiconductor lasers

The interaction of excited electronic states, such as those of a quantum dot, with cavity photon modes can generate a host of non-linear optical effects which can affect the photon statistics. It is also possible to analyze the photon stream of a semiconductor laser. This is particularly interesting because the autocorrelation function also provides a measure of the degree of coherence of the light. For the perfectly coherent light emitted by a laser, only the statistical shot noise in the photon arrival time will determine the photon statistics, so that $g^{(2)}(\Delta t) = 1$. However, in a pulsed laser structure, it will take time for this coherence to build up following the injection of charge carriers into the ensemble: for stimulated emission to occur, a population inversion must be reached, with more emitters, such as quantum dots, being in the ground state than in the excited state. The rate at which stimulated emission depletes the ensemble of excited states depends on the density of photons in the laser structure, i.e. the quality of the optical cavity. Since the laser structure emits many photons efficiently, it is not necessary to use high quantum-yield photodetectors such as photomultipliers or avalanche photodiodes (APDs) for photon counting. Instead, a streaked intensified multichannel plate, a streak camera, can be employed, which offers far superior timing resolution of picoseconds compared to the hundreds of picoseconds of conventional APDs, but at the expense of lower overall detection efficiency. This technique of measuring $g^{(2)}(\Delta t)$ with a streak camera was pioneered by Bayer *et al.*[115-119] The four extreme cases of photon correlations from an ensemble of excitons are illustrated in Figure 11. If the microscopic sources of light (black), e.g. quantum dots, act independently of each other but the entire system is in thermal equilibrium, with no external confinement of the electromagnetic field, then the light arising from spontaneous emission will be "thermal" in nature, i.e. chaotic. Such a thermal emitter has a finite phase correlation time, which maintains a certain degree of first-order coherence for $\Delta t \rightarrow 0$, so that the second-order coherence tends to $g^{(2)}(\Delta t = 0) = 2$. This result can be arrived at entirely classically from Maxwell's equations by considering intensity fluctuations.[6] When the light sources are confined in a three-dimensional cavity (Figure 11b), however, the spontaneous emission process is still incoherent but directed into the optical mode of the cavity, thus slightly suppressing the value of $g^{(2)}(\Delta t = 0)$ below 2. In such a cavity, below the population threshold for stimulated emission and laser action, the photon emission still remains uncorrelated. However, the presence of the cavity may facilitate photon exchange between the light sources, so that a phase relationship between the different emitters can be established spontaneously. As in the discussion of superradiance from pairs of molecules in Figure 5, one can view this effect as the sharing of one and the same photon by two or more different but degenerate quantum systems. The electronic quantum systems – such as quantum dots – are indistinguishable with regards to the electromagnetic field, implying that the new dressed quantum-mechanical basis set is formed from the sum of the different permutations of the exciton-photon-coupled system. The formalism is not dissimilar to the summation of permutations of spin pairs used when describing the singlet state $|S\rangle$ of a pair of spins as the superposition of the two permutations, $|S\rangle = |\uparrow\downarrow\rangle - |\downarrow\uparrow\rangle$. An entangled many-particle state is formed, independent of excitation density, which gives rise to "super-thermal" (i.e. $g^{(2)}(\Delta t = 0) > 2$) behavior in the photon statistics, limited in magnitude solely by the size of the entangled ensemble. Such behavior has been shown to arise for multiple quantum-dot emitters coupled to one single-mode optical cavity but is decreased as the size of the emitter ensemble increases, and is disrupted by electronic dephasing.[120] Finally, the effect of excitation density must also be considered. Above the threshold of population inversion, stimulated emission and laser action will set in, coupling all emitters in the quantum-dot ensemble to each other via the cavity mode and giving rise to coherent emission with shot-noise photon statistics of $g^{(2)}(\Delta t = 0) = 1$.

Since the dynamics of build-up and decay of laser action in such a microcavity laser depend sensitively on the population density, it is helpful to define the origin of the time axis as the maximum in emission intensity. Figure 11f shows the evolution and decay of light emission from these nanopillar laser structures in response to non-resonant exciton generation by a laser pulse of approximately 20 ps duration. As the laser power increases, the onset of the intensity with time becomes steeper but the decay also becomes longer lived. The streak-camera photon-correlation technique allows $g^{(2)}(\Delta t)$ to be measured simultaneously, as a function of the "microtime" as shown in Figure 11e, i.e. the time with respect to the driving laser pulse, defined by the maximum in the luminescence intensity. Indeed, all curves acquired above the threshold of laser action of ~70 μW show a period over which coherent emission with $g^{(2)}(\Delta t = 0) = 1$ occurs. The duration for which this coherence persists increases with increasing population density, since more and more excitons become available to undergo stimulated emission. However, once the population density becomes sufficiently depleted again, super-thermal emission behavior returns. The below-threshold case (light-blue curve) shows approximately thermal emission with $g^{(2)}(\Delta t = 0) \lesssim 2$ during the pulse maximum, offering a distinct differentiation between the cases of spontaneous and stimulated emission.

Such dynamic photon correlations can be used to explore the different properties of various photonic cavity structures, including more complex photonic crystals, and are particularly interesting with regard to examining the dynamics of hybrid light-matter species such as exciton-polaritons,[121] which themselves can undergo Bose-Einstein-like condensation,[122] even in molecule-based materials.[123] In fact, even ensembles of dye molecules in a microcavity may show signatures of photon bunching when they are in thermal equilibrium. This is a simple consequence of the fact that the photons themselves condense following Bose-Einstein statistics.[124,125]

E. Materials science

Given the extraordinary power of photon-correlation spectroscopy in unravelling dynamical processes in the life sciences, one would be inclined to expect an equally broad range of applications in materials science, such as in the self-assembly of polymers into supramolecular structure – or the opposite process of melting above the glass-transition temperature, or in response to solvent-vapor-induced swelling.[126,127] Such processes are central not only to the entire plastics industry, in cosmetics and detergents, and increasingly in nanomedicinal pharmaceutics, but surprisingly few concrete examples of exploiting photon statistics to examine these processes have been reported.[128,129] This lack reflects, in part, the fact that polymer physics is considered inherently macroscopic and statistical in nature, with little utility attached to microscopic sub-ensemble parameters.

An interesting recent example in materials science is the use of FCS to examine the mechanism of polymer nanoparticle formation by monitoring polymer coalescence directly during nanoparticle preparation following different processes in order to determine the most effective growth method given the processing conditions at hand.[130] The study involved polymeric nanoparticles, which were formed by either solvent evaporation from emulsion nanodroplets of polymer solutions or by so-called miniemulsion polymerization following ultrasonication. The approach could also be applied to inorganic nanocapsules formed by polycondensation of alkoxysilanes at the interface of nanodroplets. The idea put forward is to label the different constituents with dyes of different colors and identify coalescence in the diffusion properties of the dyes distinguished in the two fluorescence channels. The results revealed, quite surprisingly, that coalescence is less important for the first two growth mechanisms (solvent evaporation or miniemulsion polymerization) but crucial in the third (polycondensation of alkoxysilanes). Figure 12a illustrates the basic approach to the experiment. Two different polymers, present either in their native form or as oligomers prior to polymerization, are dispersed in water by stirring and ultrasonication, and are stabilized by means of a surfactant to form nanoparticles. Mixing these two dispersions together leads to a mixture of nanoparticles. The two types of polymer can be distinguished by the color of the dye labels (blue, red) attached to them. Following polymerization or solvent evaporation, dispersed stable nanoparticles are formed, but it is not immediately clear whether these are homogeneous, i.e. all blue or all red, or heterogeneous due to polymer coalescence. Figure 12b illustrates the procedure of the two-color FCS technique. Two excitation volumes are created by the two lasers exciting the blue and red dye labels. These two labels diffuse into the overlapping excitation volumes either independently (left) in the case of no coalescence, or in lockstep (right) in the case of coalescence. The autocorrelation (AC), $G(t) \equiv g^{(2)}(\Delta t)$, of the red and blue fluorescence intensity (Figure 12c) shows the familiar simple functionality expected from two-dimensional diffusion in solution (cf. Section III.D). The two color channels can now be cross-correlated (CC) to reveal either an absence of a correlation (panel c, left), corresponding to the case of no coalescence; or a correlation (panel c, right), implying polymer coalescence.

This straightforward experiment demonstrates the ability to follow physico-organic synthesis *in situ*, though still not strictly on the single-photon level. However, by driving a particular chemical reaction on an organic molecule through the addition of excitation energy, it is actually possible to track organic synthesis directly in space and time, as discussed in the following section.

F. Photocatalysis

It is hard to overstate the role photocatalysis has assumed in current research activities, even though Nature's precedent – aesthetically pleasing as it may be – is perhaps surprisingly inefficient in terms of energy conversion yields. Synthetic chemistry is, inherently, at once microscopic and macroscopic, the microscopic chemical reaction pathway being as crucial as the macroscopic overall reaction yield. In a photodriven conversion, one may think of "light" as a chemical "substance", reacting with another compound, possibly facilitated by a catalyst, to form a product.[131-133] But chemical reactions are generally described in terms of molar quantities, not with regards to single molecules, which a reaction with a single photon would entail. An obvious chemical reaction to study on the single-molecule level is photo-oxidation, the breaking of a covalent $C-C$ bond to form a keto or alkoxy group, which alters the fluorescence efficiency, lifetime and spectrum of the molecule.[134] Such a possibility was first demonstrated by Christ *et al.*,[135] but the process is irreversible and is therefore only of limited utility: the fluorescent molecule is destroyed by the chemical reaction. It is more preferable to design a single-molecule, single-photon cycle, in which one and the same molecule is reused repeatedly to perform a particular reaction.[136] Such a cycle is offered by employing the single dye molecule as a photocatalyst rather than as a reagent: the catalyst reacts a "substrate" molecule with the second reagent – light – to form a product molecule. Fortunately, many such reaction cycles involving dye molecules exist. Figure 13 shows an example of a photoadditive chemical photocatalytic cycle exploiting consecutive photoelectron transfer (conPET), based on a simple rhodamine dye molecule in water, where it adopts a cationic ground state.[137] Excitation of the molecule by a green photon of energy $h\nu_1$ leads to the formation of the excited state of the molecule S_1, which can gain an electron from a common reducing agent such as ascorbic acid – commonly known as vitamin C.[138] Since the rhodamine dye molecule has now changed its charge state, it can no longer simply relax to the ground state by emitting a photon, but instead undergoes slow internal conversion, dissipating the excitation energy as heat. Formation of the neutral rhodamine radical state opens up new optical absorption transitions, which can be excited by a second blue photon of energy $h\nu_2$. This excited photoradical can now transfer an electron to the substrate molecule 2-bromobenzonitrile (BrBN), cleaving the halogen bond to yield BN. The dye photocatalyst is thus returned to its cationic ground state. The point of this particular experiment is that every step of this photoredox cycle affects the fluorescence yield of the single dye molecule: in the ground state, it can absorb light to emit fluorescence, but not once it has entered the radical state. However, PET to the BrBN molecule following absorption of the second photon returns the charge state of the dye to the original configuration, reopening the fluorescence channel, rendering the dye molecule bright. The overall yield of this mechanism can be quantified by standard chemical analysis procedures such as nuclear magnetic resonance,[137] but in order to follow the cycle on the single-molecule level, a crucial trick has to be applied: the photocatalyst must be immobilized so as to prevent it from diffusing out of the focal volume of the fluorescence microscope, while at the same time allowing it sway in solution so that it can interact with the substrate BrBN molecules. This condition is achieved by tethering the dye molecule to one end of a dsDNA (double-stranded deoxyribonucleic acid) oligomer and affixing the other end of the strand, approximately 10 nm in length, to a biotinylated glass slide surface using conventional streptavidin-biotin supramolecular biochemistry techniques. For the photocatalytic reaction to work, both the reducing agent ascorbic acid and the substrate molecule BrBN have to be present in sufficient, i.e. molar, quantities, whereas the photocatalyst dye must be dispersed down to concentrations enabling single-molecule imaging, i.e. at nanomolar concentrations.

Mere inspection of the brightness of the single dye molecule as a function of time will not offer insight into the reaction dynamics since the effect of these dynamics will be masked by random fluctuations in local molecular density and conformation, as well as by photoquenching and photobleaching effects of the dye. Instead, the intensity correlation $g^{(2)}(\Delta t) - 1$ of the fluorescence is inspected as plotted in Figure 14. For nitrogen-saturated water, the rhodamine dye can either cycle between the singlet states, in which case it appears bright, or else enter the triplet state, switching off the fluorescence. The correlation shows a single-exponential functionality with a well-defined amplitude and lifetime corresponding to the triplet lifetime. Note that, since the dye molecule is immobilized in solution, unlike in the FCS experiments discussed above, molecular diffusion cannot occur and does not play a role in the photon statistics. The fact that the triplet state is involved in the photon correlation becomes immediately apparent from flushing the solution with air: the amplitude vanishes and the correlation becomes flat with respect to the correlation time Δt. Since the single dye molecules are ultimately destroyed due to photo-oxidation, the high signal-to-noise level in the data is reached by adding the correlation functions of multiple single molecules. In this particular representation, the functionality plotted corresponds to the median value of 200 single correlation curves.

Adding the reducing agent to the solution stabilizes the dark state by opening the possibility of forming the radical ground state $R^{\cdot}$. This state can be populated either directly from the short-lived singlet excited state of the dye molecule, or from the triplet. Ultimately, after a time longer than the triplet-state lifetime, the radical loses its electron again to the environment, returning the dye to its singlet ground state, reopening the excitation cycle. This correlation function, which is accurately described by a single-exponential fit, is the starting point to examine the effect of the additional reagents. Adding the substrate molecule in Figure 14d to the solution has virtually no effect on the shape and amplitude of the correlation function: the relation between "on" and "off" times of the fluorescence remains unaffected. In contrast, adding the second "reagent" to the reaction, the light $h\nu_2$ at 405 nm corresponding to the absorption band of the dye radical, has a considerable effect on the correlation, lowering its amplitude and shortening the correlation time. As indicated in the scheme in Figure 14e, raising the dye radical into its excited state can accelerate the shedding of the additional photoelectron to the environment and the concomitant internal conversion of the dye to the ground state. The entire photocatalytic redox cycle is closed when all three components are present in panel f: the reducing agent, the substrate and the "reactant", a photon of energy $h\nu_2$. Now, the photoexcited dye radical has a target to transfer the photoelectron to – the BrBN substrate molecule – so that the dye can swiftly return to the fluorescent ground state. The "on" time of the fluorescence increases dramatically and the "off" time is no longer measurable. The remarkable conclusion from these experiments, based merely on the fluorescence photon statistics of the single molecule, is that the organic chemical reaction, the photocatalytic transformation of the substrate molecule – the dehalogenation reaction, i.e. the cleaving of the covalent bromine-boron bond – can be watched in real time and space, one molecule at a time. The experiments reveal that one and the same single rhodamine dye molecule can cleave over 140 such covalent bonds per second – an astonishingly high "turnover number" for such a simple molecule. Being able to track the photocatalytic reaction on the single-molecule level offers insight into the overall efficiencies one may hope to achieve in the ensemble. Crucially, the experiments also demonstrate that pre-association of catalyst and dye molecule must occur prior to the reaction. Since internal conversion of a photoexcited radical state is extremely efficient and often occurs in under a nanosecond,[139] intuitively, one would expect catalytic conversion in solution to be limited by diffusion of the substrate molecule to the catalyst molecule. At the single-molecule concentrations employed here, such diffusion would appear to be very slow and, indeed, there is no indication that diffusion could be the rate-limiting step in the measurements. Instead, it is reasonable to propose that electrostatic interactions drive an association of the substrate molecule with the photocatalyst once it enters the radical state, before the radical is photoexcited to transfer its electron to the substrate. On the other hand, for the cycle to begin anew, the substrate molecule has to dissociate from the photocatalyst again once the reaction has taken place. The underlying electrostatics and molecular dynamics of this intriguing process remain the subject of investigation, but the application of photon correlation spectroscopy to the exciting problem of organic photoredox catalysis clearly offers an answer to the recent call for "*the need to elucidate the photochemical mechanism*".[140]

IV. RECENT DEVELOPMENTS IN ULTRAFAST PHOTON-CORRELATION SPECTROSCOPY

Conventional techniques of photon-correlation spectroscopy based on the HBT setup are limited fundamentally in time resolution by the excited-state lifetime of the object under study and by the speed with which photons can be acquired and processed, i.e. the timing resolution of the photodetector and the detection electronics. Recently, two additions to the conventional approach of photon-correlation spectroscopy have been reported, adding a further time axis to either the excitation or the detection pathway.

A. Photon antibunching under double excitation

A typical APD used for detecting light between 400 and 700 nm can achieve a time resolution of a few hundred picoseconds in a TCSPC setup, but this depends very sensitively on the wavelength of the incident radiation.[141] How then would one go about measuring a PL lifetime of a single molecule on much shorter timescales? The idea, illustrated in Figure 15, is to use a double excitation of a single quantum emitter, such as a molecule, and to measure the photon coincidence rate as a function of the timing ΔT between the two excitation pulses. If ΔT is much shorter than the excited-state lifetime, the second excitation pulse will have no effect on the light emitted. The single molecule will emit precisely one photon, giving rise to a pronounced antibunching dip $g^{(2)}(\Delta t = 0) \approx 0$ in the photon coincidence histogram, formulated here in terms of a "photon coincidence ratio" CR. When the spacing between the two excitation pulses is sufficiently large, the dye molecule can be re-excited to emit a second photon. In this case, $g^{(2)}(\Delta t = 0) \approx 0.5$, equivalent to the photon coincidence ratio. The evolution of the photon coincidence histogram with the interval between the two laser pulses therefore offers a direct way to probe the excited-state lifetime, entirely independently of the time resolution of the photodetection setup.

An example of an application of this technique is shown in Figure 16, exploiting the aforementioned singlet-singlet annihilation (panel a, cf. Figure 4) between chromophores of a rather rigid ladder-type poly(*para*-phenylene) π-conjugated polymer, the structure of which is shown in panel b. The evolution with pulse interval ΔT of the photon coincidence ratios determined from several photon coincidence histograms of single molecules is shown in panel c: for zero spacing in time, when both pulses coincide, the single polymer molecules show virtually perfect photon antibunching, with the photon coincidence ratio values CR grouping around unity. As the delay time increases, the histograms broaden and shift to an average value of 0.5, corresponding to double excitation of the polymer molecule. The red lines show a simple Gaussian fit to the histograms in order to extract a mean value of the photon coincidence ratio for a given interpulse delay time. The technique works particularly well for this ladder-type conjugated polymer since the high degree of structural and energetic order favors efficient intramolecular energy migration and interactions between different regions of the polymer chain: singlet-singlet annihilation is especially effective in this material, as in other polymers of high rigidity such as macrocycle-encapsulated poly(*para*-phenylene-ethynylenebutadiynylene),[142,143] thus giving rise to high-quality photon antibunching. The average photon coincidence ratio $\overline{CR}$ is plotted on linear and logarithmic scales in Figure 16d, e, as a function of interpulse delay time ΔT, revealing a single-exponential decay with near-perfect agreement with the fluorescence lifetime determined by conventional TCSPC.

The time resolution of this new femtosecond double-excitation (FeDEx) technique is limited solely by the width of the laser pulse used for excitation. PL lifetimes as short as 19 ps were reported by applying this technique to plasmonically enhanced fluorophores, dye molecules coupled to noble-metal nanoparticles.[141] In fact, non-radiative energy-transfer processes can also be probed using this method, on even shorter timescales. In symmetrical single-molecule acceptor-donor-acceptor complexes, a π-conjugated oligomer with two identical dye endcaps, the donor-to-acceptor energy transfer on a timescale of 13 ps could be measured by the reduction in the quality of photon antibunching of the endcaps under double-pulse excitation.[141] The temporal dynamics on the single-molecule level were found to be in perfect agreement with ensemble femtosecond transient-absorption measurements of the oligomer donor: in two rather different experiments, the same energy-transfer rate is determined by either considering the donor bleaching (in transient absorption) or the photon statistics of the endcap emission (in FeDEx).

These experiments pose very interesting questions with regards to the radiative rate of light emission from nanostructures. In principle, fluorescence lifetimes as short as the femtosecond laser pulse can be measured. From straightforward considerations of electrodynamics, one can estimate that the typical rate of radiation damping of a dipole-allowed atom-like transition, i.e. of the decay of the excited-state population, corresponds to a radiative lifetime of the order of 10 ns.[144] This decay rate can be raised by enhancing the local electric field amplitude, for example by using photonic confinement and changing the photonic mode density,[145] by coupling to plasmon resonances in metal nanoparticle,[146] or by overcoming the impedance mismatch between the nanoscale dipole of the emitter and free space in optical antenna structures.[147] But it is quite challenging to approach lifetimes substantially below 100 ps – and, with conventional TCSPC techniques – it is hard to measure such short lifetimes without having to resort to deconvolution procedures with the instrument response function,[148,149] which may introduce uncertainties. This technique of measuring photon antibunching under double-pulse excitation therefore offers a unique approach to explore the effectiveness of new nanophotonic structures, or even novel quantum emitters, provided that these serve as deterministic sources of single photons. The highest radiative rates of light sources reported to date, corresponding to lifetimes far below 1 ps, are associated with intraband transitions in noble-metal nanoparticles,[150,151] and with interband transitions in novel two-dimensional semiconductors,[152] but as yet it has not been possible to demonstrate deterministic emission of single photons from such transitions.

B. Time-resolved photon antibunching

The alternative to measuring the degree of photon antibunching under double-pulse excitation in order to acquire an additional time dimension in the measurement is to time-resolve the actual measurement of the intensity autocorrelation. In the example of studying the build-up of coherence in a semiconductor laser nanostructure in Fig. 11, $g^{(2)}(\Delta t = 0)$ is plotted as a function of the “microtime” with respect to the laser pulse that generates the exciton population. Such a time dependence of the correlation function appears feasible and meaningful for the high photon fluxes associated with a laser structure (see Section III.D), where either classical photon emission or photon bunching occur. But how would the approach relate to the case of photon antibunching, where the photon fluxes are inherently low? As discussed in Figure 4, in a multichromophoric structure, photon antibunching arises because of the interaction between two (or more) excited states, the absorption of the excitation energy of one chromophore by the excited state of another one. This process of resonant dipole-dipole coupling is not instantaneous and requires time to build up. In a multichromophoric system, photon antibunching will therefore not appear in the stream of photons generated immediately following a short excitation pulse, but will take time to build up, i.e. it will become apparent at longer delay times with respect to the excitation. As the excited states of the chromophores interact with one another, the number of effectively independent chromophores in the structure will decrease with time after excitation. The underlying dynamics are illustrated in the schematic of an example of five chromophores shown in Figure 17a,b. The HBT setup measures the degree of photon correlations. Therefore at least two chromophores must be excited to detect two photons simultaneously, as sketched. The next-higher order would be the simultaneous population of three excited states, which is clearly always far less likely to occur. The HBT intensity autocorrelation measurement will therefore first and foremost be controlled by the case of two excitations being formed in the multichromophoric structure. These two excitations can now interact with each other by singlet-singlet annihilation as described in Figure 4, which removes one excitation from the system and thus reduces the number of observed photon correlations, raising the contrast of the photon antibunching. Over time, the system will thus increasingly look like one with a lower number of independent chromophores. It is also conceivable that the two excitons formed are not situated on the most proximal sites, but first have to undergo an intersite diffusion process by FRET. As the excitons move around in space, they couple more and more chromophores to each other, until all chromophores are effectively incoherently coupled at the latest microtime after photoexcitation. The consequence of this interaction shows up in the $g^{(2)}(\Delta t)$ measurement performed with time-gated photons selected at a particular time interval after photoexcitation, as shown in Figure 17c, d. Panel c illustrates the standard TCSPC signal, which decays in amplitude exponentially with time. Five different delay times are chosen to compute the $g^{(2)}(\Delta t)$ histograms: as the delay time increases, the depth of the $g^{(2)}(\Delta t = 0)$ dip increases, until perfect photon antibunching with $g^{(2)}(\Delta t = 0) = 0$ is recorded for photons detected at the longest delay times. The five chromophores then behave as one, emitting precisely one single photon at a time.

While this concept may, at first glance, seem compelling, the approach entails several complexities since it effectively departs from the usual computation of the correlation integral in the limits of $\pm\infty$ by utilizing finite limits. The situation is then best described completely in the quantum-statistical picture of the response of each chromophore to a short-impulse laser field. A detailed derivation of the photon correlations under the condition of such time-resolved photon antibunching under pulsed excitation is given in the Supplementary Information of Ref. 153.

To test this proposal, one needs to develop a multichromophoric structure consisting of identical chromophores with very well-defined spacings between them. This goal is achieved by using the technique of DNA origami, folding DNA segments into molecular superstructures as illustrated in Figure 17e. When the two dye molecules are far apart they no longer interact with each other, neither by homo-FRET (cf. Figure 4a) nor by singlet-singlet annihilation (cf. Figure 4c). Each dye molecule radiates photons independently of the other molecules. When the dye molecules are close to each other they interact, so that the pair of dye molecules appear as a single-photon source. The DNA origami structures consist of rigid poles, onto which the five dye molecules are placed. Figure 18 shows the evolution of the number of independent chromophores, n, calculated from the $g^{(2)}(\Delta t)$ measurement, with time after excitation for seven different aggregate structures with different numbers of dyes and different spacings between them. The number of independent chromophores are calculated by taking into account the finite signal-to-noise ratio as described in detail in Ref. 15. For a background-free measurement, the ratio between the central peak height in the correlation histogram, N_{c}, and the height of the lateral peaks, N_{ℓ}, determines the number of effectively independent emitters n, $n = 1/(1 - \frac{N_{\mathrm{c}}}{N_{\ell}})$. Note that N_{ℓ} has to be determined for the limit of $\Delta t \to \infty$ to avoid obscuring of the baseline of the coincidence histogram by the photon bunching effect. Alternatively, photon bunching effects can simply be suppressed by quenching the dark state, usually the triplet, by oxygen, as is the case in many of the experiments discussed here. A value of $\frac{N_{\mathrm{c}}}{N_{\ell}} \approx 0$ corresponds to one emitter, $\frac{N_{\mathrm{c}}}{N_{\ell}} \approx 0.5$ to two, $\frac{N_{\mathrm{c}}}{N_{\ell}} \approx 0.67$ to three, and so on. Figure 18a shows the two trivial cases of either only one single dye molecule being present in the structure (dark grey) or of two dye molecules at opposite ends of the structure (light grey), separated by 12 nm. In both cases, the number of independent chromophores does not change with the microtime after excitation since no interchromophoric energy transfer is possible. The extracted number of independent chromophores is, therefore, 1 or 2, respectively. The situation is very different in panel b when the two dyes are placed either 6 nm or 3 nm apart. Now the number of independent chromophores changes with time, starting at 2 and evolving down towards 1 with increasing microtime. The rate of decay of this metric with time corresponds to the singlet-singlet annihilation rate k_{SSA}. This rate is a crucial parameter in biomolecular optics and organic electronics because it determines how effectively excitation energy, for example in an OLED or a solar cell, is dissipated non-radiatively and therefore lost.[54] Although it constitutes an inherently microscopic parameter, it is generally determined by macroscopic measurements such as ultrafast fluorescence and pump-probe spectroscopy. Here, with the time-resolved photon-antibunching technique, the rate of singlet-singlet annihilation is quantified directly on the microscopic level. As the complexity of the structure increases in Figure 18c for the case of three dye molecules, the dynamics depend again sensitively on the spacing between molecules. In both cases, the initial number of independent chromophores starts out at $n = 3$. For a spacing between dyes of 6 nm, radiative recombination of the dye excited state competes with singlet-singlet annihilation, whereas for a spacing of 3 nm, within 4 ns after excitation all three dye molecules have interacted with each other, so that the multichromophoric structure behaves as a perfect single-photon emitter. The rate k_{SSA} is lowered when compared to the bichromophoric arrangement with 3 nm spacing in Figure 18b because there are now multiple interaction mechanisms for nearest-neighbor and next-nearest-neighbor dyes. Finally, panel d shows the evolution of the fully populated pentachromophoric structure. Again, the number of independent chromophores, derived from $\frac{N_{\mathrm{c}}}{N_{\ell}}$, starts out at the expected value of $n = 5$. Here, k_{SSA} is lowered even further compared to the previous two examples because FRET between the dyes now precedes efficient singlet-singlet annihilation, effectively slowing down the process.

These DNA-origami structures are mainly of academic interest, but they offer unambiguous proof of the feasibility of counting the effective number of independent chromophores within a multichromophoric aggregate system. As discussed in Section VII.D, this approach can be used to quantify the number of emitters in molecular structures of high complexity, such as mesoscopic aggregates of conjugated polymers.

C. Higher-order correlation functions

By inserting additional beam splitters in the microscope detection pathway, it is possible to measure the higher-order photon correlation functions such as $g^{(3)}(\Delta t)$ and $g^{(4)}(\Delta t)$, i.e. to detect three- and four-photon emission events.[154] Such a measurement offers greater sensitivity to the absolute correlation amplitude in both bunching and antibunching with regards to the the background noise, such as dark counts of the detectors,[155] but comes at the expense of necessitating an overall higher number of photons and hence longer integration times, greater luminescence intensities, and improved material stability. Higher-order correlation functions offer more quantitative information from photon antibunching on the number of fluorophores present, and are therefore of great interest in studying processes in systems biology. The feasibility of counting over a dozen single emitters on millisecond timescales has been demonstrated.[156-159] The approach is insensitive to random fluctuations in intensity such as due to photoquenching, and is therefore superior to the conventional method of simply considering the integrated fluorescence intensity to acquire quantitative information on materials. Considering $g^{(3)}(\Delta t)$ and $g^{(4)}(\Delta t)$ is especially helpful for studying multichromophoric objects with a large number of independent emitters (>10), because the contrast for three- or four-photon events over the random background is larger as compared for two-photon events.

V. PHOTON STATISTICS IN OPTOELECTRONIC MATERIALS

The HBT-type luminescence autocorrelation technique can be applied to a broad range of optoelectronic materials to assess the impact of quantization effects on light emission. We begin by illustrating the diversity of materials suitable for such investigations before focusing our discussion on a particularly interesting group of materials, organic semiconductors.

A. Symmetry breaking in molecular model compounds

As elaborated upon in the previous section, the interaction between different chromophores within a multichromophoric compound is a particularly interesting problem to study. It relates to the question of how different chromophores, for example in a biological light-harvesting complex, interact with one another; or, in the context of organic electronics, how large the effective unit of volume in a film of an organic semiconductor is, in which the molecular constituents behave together as a source of light, acting in unison. But what about a molecular object with no obvious well-defined chromophore units, in contrast to the dye molecules discussed in the previous section? In a π-conjugated system, the typical extension of an excited state is 2-3 nm, determined by the spatial delocalization between the electron and "hole" of the exciton formed.[160] This delocalization in turn depends on the strength of electrostatic screening, i.e. on the dielectric constant – which can be small in such materials. What then if the π-conjugation of a molecule extends far beyond the size of a typical exciton? This may be the case in a large oligomer or polymer, but since such molecules are not characterized by a persistent shape, it is not immediately obvious how to relate excitonic localization to spectroscopic observables in an experiment. The solution to this challenge is to employ a molecule with a very well-defined shape, such as that of a ring or wheel.[10,161,162] Figure 19a illustrates such a π-conjugated molecule with the aid of a scanning-tunneling microscope (STM) image. The molecule has the shape of a spoked wheel so that all single molecules essentially acquire the same form. The conjugation extends along the perimeter of the wheel, over a distance of some 16 nm. Under linearly polarized excitation, switching between horizontal (H) and vertical (V) polarization on the microsecond timescale, different parts of the ring perimeter will be excited, but, of course, the exciton is then free to move along the perimeter. Spontaneous symmetry breaking will occur, as indicated by the schematic potential-energy surface in Figure 19b, so that linearly polarized excitation in either plane will result in fluorescence in either polarization plane: there is no memory of the excitation polarization in fluorescence.[161] The luminescence is split into the two polarization planes by means of a polarization beam splitter. There are now two ways to perform the HBT autocorrelation measurement: either with a regular beam splitter, revealing the pronounced photon antibunching shown in Figure 19c (the dashed grey lines indicate the expected correlation amplitude for one or two quantum emitters, given the signal-to-noise ratio of the experiment); or with the polarization beam splitter in panel d. In this experiment, the intensities of H and V polarized fluorescence are cross-correlated with each other. The striking result is that there is no correlation amplitude to be seen in the signal, down to the timescale of the laser repetition period of 50 ns. In other words, there is no memory of the photon polarization state from one photon to the next: each photon is generated with a random polarization. As a consequence, the time-integrated fluorescence of this wheel-shaped molecule appears unpolarized.[10]

Under excitation by either linearly polarized laser light of temporally alternating polarization plane, or circularly polarized light, an exciton is generated anywhere on the perimeter of the wheel structure. It can subsequently move along the perimeter by intramolecular energy transfer, leading to a loss of polarization memory. Such spontaneous symmetry breaking in extended systems of π-electrons is likely to be a generic feature and will also arise in conjugated polymers, which, though nominally rigid, can also undergo substantial bending.[163] In such materials, the symmetry breaking due to strong localization in the excited state will give rise to a dramatic and swift loss in polarization memory. Such localization dynamics are crucial to a microscopic understanding of the excitonic dynamics,[160,164] and therefore also relate to the overall range in space of excitation energy transfer.[165] Similar effects in terms of rapid polarization fluctuations and a loss of polarization memory were also reported for molecular polygon structures made of multiple identical chromophores.[166] A further way to test such localization and symmetry breaking dynamics on the single-molecule level is illustrated in Figure 20. A molecule was designed which consists of an oligomer donor (blue) and two different endcap acceptors, green and red. If the two endcaps are spaced sufficiently far apart so that energy transfer between them is suppressed, then the spontaneous symmetry breaking in the extended π-electron system of the oligomer will determine whether the excitation energy flows to the global (red) or local (green) energetic minimum. The molecule acts like an excitonic seesaw, the dynamics of which are revealed by studying either the fluorescence intensity autocorrelation of one of the fluorescence channels (blue, green or red) or the cross-correlation between them. All measurements shown in Figure 20c were performed under air, thereby quenching most of the triplet population and enhancing the overall fluorescence signal. The first three panels show the intensity autocorrelation of the oligomers, without the endcaps, and of the two endcap molecules. Only for the green dye molecule is a finite correlation amplitude due to the triplet state apparent. The lower two panels show the cross-correlation between the two endcap emission channels, red and green luminescence, for a long oligomer of 8 repeat units and a short one of 4 units. In both cases, a pronounced anticorrelation is seen in the two intensity channels, extending up to a duration of 10 ms: when a green photon has been emitted, the probability of subsequent emission of green photons is greater than that of red photons, and *vice versa*. Excitons in the molecule “seesaw” between the two endcaps. For the short oligomer, direct through-space energy transfer from the green to the red endcap is also possible. As a consequence, the triplet correlation amplitude of the green dye also shows up in the correlation function. Since the overall fluorescence signal is weak and the molecules tend to undergo photobleaching within a few seconds of illumination, the correlation functions shown are obtained by computing the median value of multiple single-molecule measurements as indicated by the number “*N*” in the figure, adding up single photons detected from different single molecules to extend the effective observation period.

The oligomer structure connecting the two dye molecules is not perfectly straight as can be observed by studying the polarization anisotropy in light absorption on the single-molecule level, i.e. recording the PL intensity as the plane of polarization of the excitation laser is rotated. As a consequence, symmetry breaking in the excited state and the resulting energy transfer to one of the two endcaps can be controlled by the light polarization. When the oligomer is slightly bent, changing the light polarization in excitation will direct the flow of energy to the one or the other endcap, offering an intriguing polarization-to-wavelength converter.[167]

Interestingly, a “seesaw” effect not dissimilar to that observed in this molecular structure was also found in band-gap-engineered colloidal semiconductor nanocrystals,[168] which can harbor different emissive species.[169] These structures, which have a shape somewhat resembling an avocado[170] that allows for heterogeneous carrier confinement,[32] also show near-perfect photon antibunching because of the strong Auger interaction, but have a dual-color emission, implying that single photons of either the one or the other color are emitted in sequence. Photon antibunching is then seen both in the autocorrelation of the individual color channels and in the cross-correlation between the two channels.[168]

B. Multiexciton decay in self-assembled nanocrystal quantum dots

As discussed in Section III.C, semiconductor quantum dots are used as sources of single or even entangled photons under electrical driving. However, besides this application potential, the photon statistics can be used to learn about the electronic structure of a nanoscale luminescent semiconductor material. A particularly interesting and versatile class of materials are colloidal nanocrystal quantum structures, which can acquire a range of three-dimensional shapes from dots and rods of different sizes to more complicated asymmetrical structures including tetrapods[171] and higher-order branched forms.[172] Since so much control over size and shape exists during solution-phase epitaxy, these particles exhibit a range of properties which are not easily found in conventional nanostructures grown in the gas phase. A particularly important question relates to how many excitons a quantum structure can accommodate. On the one hand, multiple-exciton formation would appear to be desirable to enable stimulated emission, but on the other hand, since the volume of the excited state is so small, strong Coulombic correlations may arise between the excitations which promote non-radiative Auger recombination.[173] While detrimental to gain,[174] such correlations could conceivably also open up the inverse process of “carrier multiplication”: a high-energy exciton splitting into multiple band-gap excitons. Such a mechanism has attracted much interest because it could potentially be employed to raise the quantum yield of a solar cell above unity, by converting high-energy photons into multiple excitons and hence multiple carrier pairs.[175-177]

Figure 21a illustrates the schematic energy levels of excitonic states in a CdSe/CdZnS quantum dot. Panel b shows the photon correlation function of a single quantum dot under CW excitation. In this case, the population density of the quantum dot will be very low, so that, on average, only one photon is emitted at once: photon antibunching occurs as a dip in the luminescence intensity correlation function, with the rise of the dip with time Δt on either side corresponding to the excited-state lifetime. Figure 21c shows the correlation function measured for an ensemble of quantum dots, under pulsed excitation with a pulse period of 212 ns. The central and lateral peaks in the correlation are of exactly the same height, i.e. the photon statistics simply mirror the Poissonian shot noise of the exciting laser. Panels d-g show the same measurement but for a single quantum dot with different excitation densities. As the population density in the quantum dot increases, a narrow peak rises up at $g^{(2)}(\Delta t = 0)$, corresponding to emission from the biexciton (BX) and even the triexciton (TX). The central peak appears much narrower than the lateral peaks because the non-radiative decay of the higher-order excitons is much faster than for the single exciton since Auger recombination competes with radiative decay. Figure 21h shows how the ratio of the central to peripheral peaks rises with increasing fluence and hence increasing population density of the quantum dot. The argument put forward based on these observations is that ordered photon emission occurs from the multiexciton states: the TX relaxes to the BX emitting a photon, then the BX relaxes to the single exciton X emitting a photon and finally the X decays to generate a third photon. Since multiple photons arrive in short sequence in response to the excitation pulse, the photon antibunching at $g^{(2)}(\Delta t = 0)$ is suppressed. However, the photon bunching one may expect to see is not observed: $g^{(2)}(\Delta t = 0)$ appears to saturate before exceeding unity. This saturation is a consequence of the non-radiative energy dissipation in the multiexcitonic states by Auger recombination, which may also modify the local environment of the quantum dot by facilitating ionization processes.[178] Nevertheless, resorting to a fairly simple trick, it is possible to mitigate this population quenching to reveal photon bunching from multiexcitonic states in single nanocrystal quantum dots: enhancement of the local electric field strength and hence the rate of spontaneous emission following Fermi's Golden Rule by coupling to metal nanoparticles.[179,180]

The biexciton emission can usually be identified by its spectral signature, along with the reduced luminescence lifetime.[181] Figure 22a offers an artistic impression of the setup employed to detect photon bunching from the nanocrystal quantum dot biexciton, along with the relevant relaxation processes. The single quantum dot is placed on a rough silver film which enhances the radiative decay k_R of both the exciton 1X and the biexciton 2X, but also gives rise to a quenching rate k_M for both species: the dipoles induce a mirror image dipole in the metal, which is damped due to Ohmic losses. As noted, relaxation of the biexciton to the ground state G of the quantum dot can also occur by Auger recombination. The effect of the rough silver film is immediately apparent from the luminescence decay transients shown in the insets of Figure

22b,c: the PL lifetime drops over 40-fold due to the presence of the metal nanoparticles making up the rough silver film, both due to quenching of the excited state by the aforementioned image-dipole losses and due to enhancement of the radiative transition. The photon-correlation function, plotted in terms of the laser pulse period, shows clear evidence of photon bunching due to the biexciton emission in the case of the rough metal substrate, with the central peak at $g^{(2)}(\Delta t = 0)$ exceeding the lateral peaks in height. In contrast, on a quartz substrate, the single quantum dot shows a behavior analogous to that discussed in Figure 21.

C. Biexcitons and exciton gating in perovskite nanoparticles

Biexcitons effectively act to suppress the fidelity of single-photon emission from a nanocrystal, and are also found in quantum dots based on organic-inorganic hybrid perovskite materials as shown schematically in Figure 23a.[182,183] A simple way to improve the apparent quality of photon antibunching is to gate the earliest photons out of the measurement, much like in the microtime analysis discussed in Section IV.B.[184,185] Since each photon arrives with a certain time tag, one can simply consider photons which arise, say, 2 ns or more after photoexcitation. This discrimination is possible because the decay of the biexciton is much faster than that of the single exciton. However, while the approach offers some insight into the excited-state dynamics, there is little utility in terms of applications where photon antibunching is desired. An alternative lies in gating the actual photon stream in the emission, by passing the light through an acousto-optical modulator (AOM) and suppressing early photons generated within a certain time of the laser pulse.[186] This approach, however, is technically rather demanding since it requires high-frequency electronics.

Because of their physical volume, quantum dots offer much higher absorption cross sections than dye molecules and can therefore be photoexcited at much lower fluences for imaging applications. In biological environments this lower fluence entails far lower background signals from autofluorescent biomolecules such as proteins. But it is the size of quantum dots which also allows for the accommodation of multiexcitonic species. The best of both worlds, strong absorption along with pure single-photon emission, can be achieved by combining both together, using the nanocrystal as the absorber and the dye as an emitter, excited by non-radiative energy transfer.[187,188] The idea is sketched in Figure 23b. The experiment uses perovskite nanocrystals, which have particularly favorable luminescence characteristics. Nanocrystals are dispersed in low concentration in a polymer film with a much higher density of dye molecules added; the dye fluorescence appears spatially continuous under the fluorescence microscope. Either photoemission occurs from the nanocrystal, in which case a maximum of two photons is emitted; or energy transfer occurs to the dye, which can intrinsically only emit one single photon. The $g^{(2)}(\Delta t)$ measurements in Figure 23d, e clearly show the effect of photon arrival time: the central to lateral peak ratio ($\frac{N_\mathrm{c}}{N_\ell}$) is 19 % when all photons are taken into account, implying a substantial contribution from biexciton emission as sketched in panel a. Excluding photons arriving within 2 ns of the excitation pulse lowers $\frac{N_\mathrm{c}}{N_\ell}$ to 2 %, vastly improving the quality of photon antibunching. Detecting the characteristic dye emission, separated from the nanocrystal by a spectral filter, shows a marked effect of the light-harvesting process on the photon statistics, even when all of the emitted photons are taken into consideration. The central dip assumes a value of $\frac{N_\mathrm{c}}{N_\ell} = 3$ %, implying that the energy transfer mechanism has an effect comparable to electronically gating out many of the earliest photons in the measurement. We note, however, that some caution is warranted in interpreting the photon coincidence histogram and stress that the $\frac{N_\mathrm{c}}{N_\ell}$ ratio does not necessarily translate directly into $g^{(2)}(\Delta t)$: as discussed below, the nanocrystal also shows a finite photon-bunching amplitude, which raises the lateral peaks in the photon coincidence histogram, thereby obscuring the true depth of the central peak. For a qualitative analysis of the effect of temporal gating this form of analysis is sufficient.

A conceivable mechanism of how this exciton-gating scheme could operate is sketched in Figure 23c: the dye molecule is excited by energy transfer from the biexciton state, raising the molecule to the S_1 excited state. Due to the photoinduced absorption of this excited state, analogous to the singlet-singlet annihilation mechanism discussed in Figure 4, the nanocrystal single exciton can decay non-radiatively by raising the dye singlet excited state to a higher-lying state from which non-radiative internal conversion occurs. The excitation energy of two excitons in the nanocrystal is converted to one photon from the dye molecule.

As discussed in Figure 4, photoinduced absorptions in the dye exist both in association with singlet excited states and with triplets. The detriment of the nanocrystal is biexciton formation, which limits single-photon generation. The drawback of the dye molecule is that it can undergo intersystem crossing to the triplet dark state, becoming non-emissive – a severe limitation in any single-photon application. The hybrid nanocrystal-dye system can mitigate this limitation too, as sketched in Figure 23i. Since the nanocrystal continues to absorb even when the dye molecule enters the dark triplet state, it can continue to pass on excitation energy to the molecule. Assuming that the energy levels align as indicated in the sketch, this excitation energy from the nanocrystal can now raise the dark triplet excitation of the molecule to a higher-lying triplet state, from which reverse intersystem crossing to the bright singlet manifold becomes feasible.[189] Panels g, h illustrate the striking effect of this mechanism on the single-photon emission of the dye molecule. Under direct excitation, the dye shows a clear photon-bunching amplitude with an exponential decay of $g^{(2)}(\Delta t)$ associated with the triplet lifetime. This correlation vanishes entirely when the dye is excited indirectly, i.e. by energy transfer from the nanocrystal. $g^{(2)}(\Delta t)$ is not entirely flat in this case, mirroring the blinking statistics of the single nanocrystal which are associated with charging effects. However, strikingly, the photon correlation of the single dye molecule (red curve) now matches almost perfectly the function associated with emission from a single nanocrystal (green curve). The triplet photon-bunching amplitude is suppressed.

These experiments illustrate the value of hybrid approaches, combining different single-photon sources made of different materials and with different intrinsic characteristics. In addition, the experiment illustrates how single nanocrystals can serve as effective excitonic antennae to pick out single molecules from an ensemble.[190,191] The dispersed dye film appears continuous under the fluorescence microscope since the spacing between the dye molecules is smaller than the diffraction limit. Energy transfer from the nanocrystal can then select single dye molecules from this continuous ensemble.

Finally, it is worth noting that because of the unique electronic structure of perovskite quantum-dot materials, the ground state is of triplet character so that the lowest-energy singlet band-edge exciton is actually a dark state.[192] This configuration promotes the creation of entangled photons in the emission from biexcitons. Because of the strong spin-orbit coupling and the unique band structure, this emission can be tuned by magnetic fields so that one and the same particle can be controlled to show either preferential photon antibunching or bunching.[193]

D. Two-dimensional transition-metal dichalcogenide semiconductors

Over the past decade, much interest has developed in the properties of atomically thin semiconductor materials, made either by exfoliation from van der Waals crystals or grown epitaxially in the vapor phase. These materials are exceptionally stable to photodegradation. As

Andre Geim famously put it, they can in effect be viewed as "giant molecules".[194] Samples can be structured to make devices and to isolate quantum emitters, which arise in the semiconductor due to defect sites. Such quantum emission as signified by photon antibunching is quite remarkable because it emanates from a macroscopic object, a flake of the van der Waals crystal some tens of microns in extension.[195-199] Figure 24a,b illustrates the schematic of such a monolayer transition-metal dichalcogenide crystal of WSe_2.[200] Discrete luminescence peaks are observed at low temperatures, labelled P1-P4 in panel c, which correspond to different excitonic species having different polarization properties, horizontal (H) or vertical (V). Peaks 3 and 4 are not visible under vertical polarization. Such a splitting in polarization states arises from the dipole selection rules of optical transitions in these semiconductors associated with the split valence band. These transitions can be shown to correspond to both exciton (X) and biexciton (XX) transitions from the excited (e) to the ground (g) state as sketched in Figure 24b. By selecting different spectral regions of the emission, the different excitonic species can be correlated with each other. The emission of both Peak 1 and Peak 2 each shows photon antibunching in panels d, e. In contrast, the cross-correlation of the photon emission from Peak 1 and 2 in panel f exhibits photon bunching with a correlation amplitude $g^{(2)}(\Delta t = 0)$ larger than the lateral peaks in the photon coincidence histogram: Peak 1 and Peak 2 are therefore associated with cascaded emission from biexciton and exciton. Note that, in contrast to the example of the CdSe colloidal quantum dot discussed in Figure 22, the volume taken up by the exciton in the two-dimensional crystal is larger, so that biexciton emission can be readily identified without elaborate enhancement schemes of the radiative rate.

E. Single-photon electroluminescence from metal nanoparticles

Photon correlations have been demonstrated in many different luminescent materials, but they can also show up in light generation from compounds and structures not immediately associated with luminescent transitions, such as in metal nanostructures. Perhaps one of the more surprising discoveries relating to scanning tunneling microscopy (STM) was that the tunnel junction between the tip and a substrate can generate light.[201] There are several possible reasons that have been put forward to rationalize this effect: plasmons may become electrically excited and emit light; inelastic tunneling itself between metals of two different electron affinities may give rise to light emission like in a metal-insulator-metal junction;[202] the metallic nanostructure may act as an electrically driven antenna for light;[203] or the statistical fluctuation in the single-electron tunnel current may give rise to a time-varying electronic dipole which leads to light emission.[204] Irrespective of the mechanism of light generation, which obviously overlap partially in nature although being described in different physical frameworks, it is interesting to study the statistics of the photons emitted. The first such investigation revealed distinct photon bunching in the luminescence generated at the tip of an STM, an effect that can be attributed to the electric charging of the capacitor formed by tip and surface and the resulting discharge by the tunneling process from tip to surface.[205] Once the electron has transferred from the tip, the potential difference breaks down and is built up again over a time corresponding to the RC time constant, the product of capacitance and resistance. In fact, with appropriate design of the system, photon "superbunching" with $g^{(2)}(\Delta t = 0) = 70$ within a time resolution of 53 ps could recently be demonstrated.[206] A further set of experiments involved the excitation of a molecular state by an STM, offering a discrete electronic excitation. In this case, which employed otherwise non-emissive C_{60} molecules to generate light in combination with the tip-substrate system, photon antibunching could be observed owing to the high stability of the material involved.[207] Electroluminescence from single zinc-phthalocyanine molecules has also been observed with an STM, showing strong photon antibunching.[208]

Light generation is not limited to sophisticated STM systems, however, but may also arise from noble-metal nanoparticles formed by electromigration. Photon antibunching from such structures was first demonstrated by Dickson *et al.*[209,210] Figure 25 summarizes the key results. A thin metal film of gold or silver is grown between two electrodes. Passing a current through the film gives rise to electromigration, so that, ultimately, nanoparticles form and the current flow is disrupted as illustrated in panel a. By applying an alternating current instead of a direct current, further electromigration is inhibited and light emission occurs from nanoparticles in the break junction region, seen as diffraction-limited spots in the microscope image in Figure 25b. Since the nanoparticle break junction corresponds, in effect, to a tunnel junction, the electroluminescence (EL) intensity increases exponentially with drive voltage as shown in panel c. As in the aforementioned example of the STM tip, substantial photon bunching is seen in $g^{(2)}(\Delta t)$ in panel d under direct-current drive, corresponding to an RC time of 7 ns. It is important to stress that this is a purely classical feature in photon correlations, related merely to the charging and discharging of the nanoparticle capacitor structure. The peak feature in the correlation function at 9 ns arises due to an artifact relating to an afterglow effect of the photodiodes used: if a photon from the nanoparticle break junction impinges on one of the detectors, it can generate secondary luminescence from the highly biased silicon, which is then picked up by the second detector. This photon bunching measurement is shown for a silver nanoparticle film, which does not exhibit photon antibunching, presumably because the excited state related to the light emission from silver nanoparticles is too short lived and can be re-excited electrically within the time resolution of the detection setup – rather like in the case of the double-excitation photon antibunching technique discussed in Section IV.A. This limitation does not apply to light generation from gold nanoparticles, shown in the photon antibunching measurement in Figure 25e under pulsed excitation. Here, a clear dip is seen in the photon correlation at zero delay time, implying deterministic single-photon generation from metal nanoparticles, at room temperature: a purely quantum signature of light emission.

F. Further material systems showing single-photon emission

In recent years, the technique of photon-correlation spectroscopy has been applied to a wide range of optoelectronic materials, particularly with the goal of demonstrating deterministic single-photon emission. Perhaps the most intriguing demonstration of photon antibunching was on a material which is not, strictly, used in optoelectronics but nevertheless serves as an example of the intricacies of light-matter interaction and energy conversion: the bacterial photosynthetic light-harvesting complex LH2, which contains a total of 27 chlorophyll pigments. Two different types of arrangements of the pigments exist in the protein complex. The packing geometry strongly controls interchromophoric coupling and ensures the overall light-harvesting functionality. Because the fluorescence yield of the complex is low, single-molecule experiments are typically very challenging to perform. However, by enhancing the radiative rate of fluorescence by using suitable metallic optical antenna structures it was shown to be possible to measure the photon statistics and reveal photon antibunching.[211]

Many types of solid-state single-photon emitters have now been reported.[212] Even objects larger than LH2 can show deterministic single-photon emission: carbon nanotubes,[102,103,109,213-215] two-dimensional crystals[196] such as hexagonal boron nitride,[216,217] and films of silicon carbide.[218] In these cases, it is defects in the crystal lattice which localize excitons and give rise to strong photon antibunching, spanning the spectral range from the UV to the IR. For example, in hexagonal boron nitride, carbon was recently identified as the source of visible single-photon emission.[219] Some of these materials have proven to be particularly stable to degradation and also suitable for integration in LED structures. Single-photon generation is particularly interesting in the IR spectral region, within the windows of minimal absorption of glass fibers as used for optical communication.[215] Both colloidal and self-assembled vapor-phase-grown quantum dots have been demonstrated as single-photon sources in this spectral region, including PbS/CdS,[220] InP/ZnSe,[221] InAs,[222] InAs/InP,[223] and InAs/GaAs quantum dots,[224] with some of these even preserving photon antibunching up to room temperature. In InAs quantum-dot structures, the measurement of $g^{(2)}(\Delta t)$ could be used to track both the photon antibunching and photon bunching effects, which appear as intensity blinking in the time traces of the luminescence.[37] This blinking in these inorganic materials arises from charge trapping. In colloidal systems, antibunching has even been found in clusters of many giant CdSe/CdS quantum dots, implying effective electronic coupling between the individual particles,[225] much like the case of multiple aggregated polymer chains.[226]

As discussed above, single-photon emission can also be generated by electrical excitation, using an STM to drive an electronic transition. A few examples exist where, instead, the electron beam of a scanning-electron microscope (SEM) is used for excitation.[227] Since the electron beam is of very high energy, typically tens of keV, this technique of cathodoluminescence is only suitable for the most stable of materials. Photon antibunching was thus observed from NV centers in nanodiamonds.[227]

A further intriguing application of photon-correlation measurements is to hybrid excitations in semiconductors, for example to strongly coupled states of light and matter – exciton polaritons formed by placing a quantum dot in a microcavity. For such a hybrid excitation, which shows a distinct splitting of the optical transition energy into two modes and a universal dispersion relation of the two modes, i.e. a textbook phonon-polariton-like dependence of the transition energy on momentum and hence on viewing angle, it is not immediately obvious that the luminescence should show photon antibunching, although it indeed does.[228] Likewise, electron-hole pairs can be coupled to vibrational modes of the semiconductor, by exciting surface-acoustic waves (SAWs) in the material. This approach has also been used to localize the carriers and enable photon antibunching to be observed.[229,230] The concept effectively corresponds to SAW-driven electroluminescence and is particularly useful for converting the electron spin quantum state to the light polarization quantum state. In fact, by coupling vibrations to quantum emitters it is, in principle, also possible to prepare single quanta of vibrations, i.e. single phonons.[231] Furthermore the single photon emitted can be coupled into a plasmon polariton mode of a silver nanowire, which in turn can decay to a photon again – photon antibunching from a collective electronic excitation.[232] Finally, the measurement of photon correlations now appears to have come full circle, back to the original application of the HBT autocorrelator in radio astronomy,[1] with the demonstration of deterministic sources of RF photons. One of these sources is based on a biased Josephson junction, a ring structure containing a superconductor/semiconductor/superconductor interface, which emits CW radiation due to the AC Josephson effect.[233] With a fixed bias, the phase of the superconductor varies linearly in time, resulting in a sinusoidal current, the frequency of which depends solely on the bias.

VI. EXCITED-STATE DYNAMICS IN ORGANIC SEMICONDUCTORS

As noted in the introduction, while photon correlation techniques can be applied to many diverse material systems, they are a particularly appealing tool to study optoelectronic materials that are inherently discrete in nature.

A. Polarization fluctuations and light outcoupling in OLEDs

An OLED consists of one or several thin layers of an organic semiconductor, usually of the order of 100 nm in overall thickness, grown on a transparent electrode on a glass substrate. A reflecting counter-electrode makes it a thin-film waveguide structure. Such waveguiding can give rise to optical losses due to reabsorption effects, and for many years has been the focus of studies of possible mitigation pathways.[234,235] As Figure 26a illustrates, the orientation of the transition-dipole moment of the light-emitting molecule has a dramatic effect on the waveguiding: when the dipole lies in the plane of the OLED, emission preferentially occurs in the forward direction, minimizing waveguide losses. If the dipole points orthogonally to the plane, light is not radiated in the forward direction but into the waveguide mode, from which it can only be released again by appropriate engineering of the refractive index or by scattering. Remarkably, OLEDs have been reported with quantum efficiencies approaching 40 %,[236] implying that waveguide losses are almost negligible because of an apparently coincidental optimal orientation of the transition-dipole moments during film growth.[237] The most efficient OLED emitter molecules are organometallic metal-ligand complexes such as the structure shown in the inset of Figure 26c, tris(1-phenylisoquinoline)iridium(III) ($Ir(piq)_3$). This compound emits phosphorescence from the triplet state. During electron-hole recombination, molecular excitations are formed in both the singlet and the triplet state, which is usually non-emissive in common purely hydrocarbon-based fluorophores. The iridium ion serves to mix triplet and singlet states by spin-orbit coupling, allowing radiative emission to occur from both[238,239] but preferentially from the lower-energy triplet. Remarkably, during OLED fabrication, it appears that the Ir(piq)$_3$ molecule adopts the optimal orientation due to electrostatic interactions with the substrate and adjacent molecules. It is therefore of great interest to determine the actual orientation of the transition-dipole moment directly in space. Conventionally, insight into this problem is gained by examining the angular dependence of the luminescence intensity emitted from a film,[240] but this approach is not sensitive to the overall molecular heterogeneity or the possibility of underlying dynamics in the dipole orientation. The Ir(piq)$_3$ molecule has threefold symmetry, so it is not immediately obvious how the transition dipole will align within the compound even if the arrangement of the molecules in the OLED can be probed by structural analysis techniques such as neutron scattering or grazing-angle x-ray scattering.

Figure 26b shows a luminescence microscope image of single Ir(piq)$_3$ molecules dispersed in PMMA.[241] Unlike the objects discussed in the prior sections, which all exhibited fluorescence, it is crucial to note that the phosphorescence of these molecules arises from a dipole-forbidden transition from the triplet state. The emission rate of photons is therefore extremely low, resulting in a detection rate even in an optimized microscope of only a few kHz. This low rate is a result of the fact that, even in the most efficient of emitters such as Ir(piq)$_3$, triplet phosphorescence lifetimes are of the order of 1 μs. With a detection efficiency of the microscope setup of 1 %, the maximum photon count rate achievable when the molecule is driven under saturation is only roughly 10 kHz. In a typical single-molecule fluorescence imaging microscope, such count rates may be considered too low since there will always be a luminescence background arising from the substrate or the molecule-embedding matrix. However, because the phosphorescence lifetime is so much longer than that of the fluorescence background, it is possible to discriminate the two by temporal gating, i.e. by using only photons detected at long arrival times after pulsed photoexcitation.[242] Once the positions of the single molecules are identified on the sample, the spectrum can be measured, as shown in Figure 26c. The intensity autocorrelation is recorded by the standard HBT setup and is shown in panel d. Since the fluorescence yield of Ir(piq)$_3$ and related compounds is extremely low owing to the efficient intersystem crossing, the luminescence of the molecule is dominated entirely by the triplet state: instead of giving rise to photon bunching, as in the previous examples, it is now the triplet which gives rise to photon antibunching. The $g^{(2)}(\Delta t)$ function in Figure 26d therefore appears with an inverted shape, with the red curve indicating a single-exponential fit with the triplet lifetime of order 1 μs. As noted, in order to arrive at a detectable emission rate of single photons, the triplet transition has to be driven close to the rate of saturation, which is determined by the triplet excited-state lifetime. The power dependence of the detection rate of phosphorescence photons shown in Figure 26e therefore appears to saturate above an excitation power of 10 μW in this experiment. Remarkably, although few studies of single molecules of such triplet emitters exist, Nothaft *et al.* even succeeded in detecting single-photon electroluminescence from Ir(piq)$_3$ molecules embedded at very low concentration in an OLED structure, with electrically driven photon antibunching.[112]

With the aid of a polarizing beam splitter it is possible to assess the degree of linear dichroism of the single Ir(piq)$_3$ molecules. A simple analysis of the statistical distribution of linear dichroism over many single molecules reveals that the transition dipoles do not adhere to a random distribution in space: the degree of polarization of the luminescence is actually substantially lower than that found for fluorescent molecules with a well-defined transition-dipole moment. The reason for this discrepancy lies in random fluctuations of the transition-dipole orientation within one single molecule, much like in the case of the random polarization fluctuations discussed in the context of spontaneous symmetry breaking in conjugated macrocycles in Section V.A. Figure 27 shows an example of the fluctuations in linear dichroism of a single Ir(piq)$_3$ molecule, measured by passing the luminescence through a polarizing beam splitter. A simple analysis of the noise in the overall single-molecule phosphorescence intensity compared to the fluctuations in linear dichroism shows that the latter cannot arise as a consequence of the former. The polarization fluctuations are intrinsic to the molecule itself: the orientation of the transition-dipole moment within single Ir(piq)$_3$ molecules fluctuates and jumps in time, very much unlike the fixed dipole orientation in common dye molecules such as perylene or rhodamine. This “scrambling” of the polarization of the phosphorescence light generated may be highly beneficial to the light outcoupling in OLEDs since it prevents light from being generated from dipoles pointing orthogonally to the plane of the film. Such spontaneous symmetry breaking could provide an explanation for the unexpectedly high external quantum efficiency of triplet-emitter-based OLEDs.[236]

B. Photon statistics and molecular conformation

A veritable “zoo” exists of molecular materials suitable for organic electronics. Whereas most commercial applications, such as OLEDs, involve small-molecular luminescent materials such as the Ir(piq)$_3$ discussed in the previous section, a remarkable versatility of characteristics has also been demonstrated for much more complex macromolecular compounds, in particular for conjugated polymers. Polyfluorenes, the structure of which is shown in the inset in Figure 28, have proven to be a particularly interesting group of polymers because they can exist in two distinct conformations as was initially demonstrated by x-ray diffractometry:[243] either the repeat units are twisted with respect to each other, as shown in panel a, or the entire chain becomes planarized, enhancing rigidity and leading to only minimal overall bending of the chain. This degree of planarization of the chain has a dramatic effect on the bond alternation and hence on the luminescence spectra: even on the single-molecule level, the twisted, so-called “glassy” phase, shows blue-shifted emission which appears spectrally broadened. In contrast, the planar “β-phase” is characterized by red-shifted emission with narrower peaks and a well-defined vibronic progression. This differentiation between the two conformational species is particularly stark on the single-molecule level at cryogenic temperatures as reported by Becker *et al.*[244] Which conformational phase is adopted by the polymer molecule depends on the processing treatment of the material. Regular spin coating tends to promote formation of the kinetically trapped glassy phase, which can then be annealed to the β-phase by solvent-vapor exposure.[245] While the differences between the two phases in room-temperature PL spectra in Figure 28 may not appear to be overly dramatic, the effect on the photon statistics, shown in panels c, d, is: the β-phase chain shows substantial photon antibunching whereas the glassy-phase chain does not. The $g^{(2)}(\Delta t)$ histograms under pulsed excitation indicate the level of the $g^{(2)}(\Delta t = 0)$ dip expected for one (*) or two (**) emitters given the signal-to-noise level. Merely the shape of the molecule, not its chemical composition, controls the photon statistics in this example. Similar observations were also made for more flexible polymer systems based on poly(phenylene-vinylene),[246] for which the chain conformation could even be controlled by inkjet printing.[247] In these materials, the quality of photon antibunching improves with decreasing molecular weight and upon folding of the polymer chain into a collapsed funnel-like structure.

A detailed study of the polarization anisotropy of single chains of β-phase polyfluorene, together with low-temperature PL excitation spectroscopy,[248] revealed that the excitons are free to explore the entire chain, even if it is curved in space.[249] The result of this excitonic mobility is that the overall polarization anisotropy in luminescence is actually somewhat lower than what one may expect from such a highly ordered molecular system. The dynamics of exciton localization within the extended π-conjugated polymer are not unlike those discussed in the excitonic seesaw or the conjugated spoked wheel in Section V.A. The net result of excitons being so highly mobile, giving rise to strong photon antibunching in β-phase polyfluorene, is that the polarization memory becomes scrambled and the overall fluorescence arising from the single molecule appears less polarized:[250] clearly a beneficial effect in terms of light outcoupling out of on OLED structure as discussed in the previous section.

Fluorescence correlation spectroscopy (FCS) is a particularly useful tool to study the effect of conformation of conjugated polymers since the "molecular brightness" (MB), i.e. the ratio between the number of photons absorbed and emitted,[251] can be compared on the single-molecule level in solution to measurements of the fluorescence quantum yield in the solid state. The MB is extracted directly from the second-order correlation function. In the simplest case, when the chain does not fold in solution, the quality of photon antibunching would be expected to simply scale with the diffusion constant in solution, which in turn relates to the size of the molecule:[252] the faster translational motion, the higher the probability of single-photon emission.[253] With this approach, Lin *et al.* found evidence that the brightness of the single polymer chain can be reduced by a dramatic amount upon immobilization of the molecules in a matrix, up to 1-2 orders of magnitude, presumably because the immobilized molecules adopt conformations which promote energy funneling to dark, non-emissive sites such as chemical defects or trapped charges.[254] As discussed in the next section, this limitation does not appear to arise in materials of sufficient purity. In addition, care has to be taken to ensure that the chains really are fully dissolved in dilute solution. Evidence for aggregate formation even at picomolar concentrations was found in FCS measurements on conjugated polymers by Wu *et al.*, who also demonstrated that these aggregates could be removed by simple syringe filtering.[255]

C. Exciton-exciton annihilation in conjugated polymers

As discussed in Section II.C, it is the annihilation of two singlet excitons within the polymer chain which enables it to emit precisely one single photon at a time, as in the previous example of β-phase polyfluorene. These excitons are formed on different chromophores of the polymer. In the dye-endcapped oligomer example structure discussed in Section II.C, it is obvious that each dye molecule corresponds to one chromophore, as in the situation of the DNA-origami structures labelled with multiple dyes described in Section IV.B. But what are actually the chromophores in a conjugated polymer? A particularly useful material system to study chromophore formation in polymers to resolve this question has proven to be ladder-type poly(*para*-phenylene) (LPPP), the structure of which was already discussed in Figure 16. Figure 29a-c shows single-molecule PL spectra recorded under cryogenic conditions, at 5 K, for molecules of three different chain lengths: an oligomer, a undecamer consisting of exactly 11 phenyl rings; a short polymer chain with, on average, 62 rings; and a long polymer chain with, on average, 165 rings. Both the oligomer and the polymer show only one peak. The oligomer spectrum is slightly broadened and shifted to the blue because of the increased exciton confinement. The message of this measurement is that, in the short polymer chain, only one chromophore unit is formed, just like in the oligomer. However, the chromophore on the polymer chain is longer than the undecamer, giving rise to additional coherence effects as discussed in more detail below in Section VII.A. These coherences narrow the inhomogeneously broadened spectrum by increasing the overall oscillator strength of the optical transition: the chromophore in the polymer chain therefore also appears much brighter than the undecamer since its extinction is greater. The case is very different for the example spectrum of the long-chain polymer: here, a total of five discrete peaks can be resolved, each assigned to a different chromophore. Evidently, the π-electron system of the polymer is disrupted in places so that discrete excitonic states are formed.[256] A statistical analysis over many different molecular weights shows that the average number of peaks observed in the spectrum indeed increases monotonously with chain length: chromophores can be counted on single polymer chains. This low-temperature spectroscopy only shows that different chromophores exist within the polymer chain: it cannot determine how many photons are emitted at once by the different chromophores. To do this, the fluorescence intensity correlation is measured. Since this measurement necessitates high photon count rates, it is best performed at room temperature using a microscope objective of high numerical aperture.

Given the high degree of photostability of LPPP molecules, it is particularly well suited to study photon correlations on the single-molecule level.[257-260] In contrast to some of the examples discussed in earlier sections of this review, where the photon statistics of multiple single molecules were considered in aggregate, i.e. by adding up the data from multiple single-molecule measurements, here, meaningful information can already be extracted from one single molecule. Figure 29d,e show photon antibunching and bunching, measured on one single LPPP polymer chain. The data quality is close to perfect, following the predictions discussed in Section II.A. Because of the high degree of rigidity of the LPPP backbone, excitons are effectively free to move between chromophores.[259] The multichromophoric structure therefore shows both signatures of virtually perfect singlet-singlet annihilation (antibunching) and singlet-triplet annihilation (bunching).

Many conjugated polymers show features of non-classical photon emission, even though the dip in the photon correlation is often quite weak and care has to be taken to ensure that the lateral peak heights in the photon coincidence histograms are not distorted by photon bunching effects. Since these are optoelectronic materials used in OLEDs, it is even possible to integrate them into diode-like structures and to study the single-molecule luminescence,[56] and the photon statistics,[261] under injection of charge carriers. Charge carriers would be expected to quench the overall fluorescence since they introduce an additional absorption band. Intuitively, one would expect this quenching effect to improve the fidelity of photon antibunching, even if fewer photons are emitted overall. However, the opposite actually turns out to be correct: a quenching of the overall PL intensity on the single-molecule level tends to correlate with a reduction in photon antibunching since energy-transfer pathways and the overall interchromophoric light-harvesting efficiency is reduced.[261]

On a side note, it is worth mentioning that conjugated polymers also give strong and discrete spectral signatures in Raman scattering. Obviously, conventional Raman scattering will not give rise to any interesting features in the photon correlation, however, some conjugated polymers have proven to be particularly suitable for studying Raman scattering on the single-molecule level, in surface-enhanced Raman scattering (SERS). Claims of single-molecule SERS initially remained somewhat controversial because there is no obvious optical means of proving that the Raman signal really does originate from a single molecule other than by invoking an indirect argument of a correlation between molecular density and Raman signal strength.[262] Only one report exists on a study of photon antibunching to confirm the single-molecule nature of SERS from small gold clusters.[263] With the brightness and versatility of conjugated polymers, which enable simultaneous detection of the single-molecule luminescence and Raman spectrum as well as the identification of different chromophores within the polymer chain,[264] it should be feasible to expand the detection to include a measurement of photon antibunching in conjunction with resonance Raman spectroscopy.

The aforementioned polymer compound LPPP is a useful model material system to explore the underlying photophysics of conjugated polymers, but because it is not commercially available in high purity and is only of limited utility in actual devices, it remains mainly of academic interest. In contrast, one of the best-known commercial materials, used widely in organic photovoltaics, is poly(3-hexylthiophene) (P3HT), the structure of which is shown in Figure 30a. The database "*Web of Science*" returns over 9,000 articles alone for P3HT, and over 10,000 more for general polythiophenes: "*the best seller in polymer photovoltaic research*",[265] as Dang, Hirsch, and Wantz called it. Having understood the general concept of the formation of polymer chromophores by inspecting the LPPP model system, the insight can easily be transferred to examine the photophysics of P3HT.[266] The polythiophene chain is quite flexible and, depending on the solvent and processing conditions, can either form extended worm-like chains, illustrated in Figure 30a, or the collapsed structures shown in panel b.[267] The optical properties of these two single-molecule species are very different indeed. Whereas the average PL intensity on the single-chain level increases linearly with molecular weight for the extended chains (Figure 30a), it saturates for the collapsed chains in panel b. One may be tempted to think that the extended polymer chains behave like the LPPP chains discussed above, with energy transfer occurring along the chain. This is not the case, however: measurement of the photon correlation $g^{(2)}(\Delta t)$ neither shows photon bunching nor antibunching for these chains. Also, the fluorescence intensity on the single-chain level does not exhibit discrete jumps but only displays continuous fluctuations. The case is very different for the collapsed P3HT chain, where the excitation energy is funneled from the entire chain to one emitting chromophore unit, marked in red in the cartoon: here, the PL intensity exhibits single-step photobleaching, shown in Figure 30c, along with a clear triplet amplitude in the photon correlation in panel d. Exposure of the single molecule to air quenches the triplet excited state, removing the correlation amplitude (blue curve). $g^{(2)}(\Delta t = 0)$ shows clear photon antibunching, which implies that emission occurs from only one state (marked red), independent of the chain length. From the photon correlation it is possible to extract the average "on" and "off" times of the fluorescence of single chains, following the procedure discussed in Section II.A, as a function of molecular weight. These values are extracted from the exponential fit to the $g^{(2)}(\Delta t)$ function and the amplitude of the correlation. As shown in Figure 30e, the average "on" time of the fluorescence decreases with increasing molecular weight. This is a rather trivial observation and to be expected: the larger the molecule, the greater the absorption cross section, the more frequently the molecule becomes excited and the more probable an excursion to the dark triplet state becomes, which quenches the entire fluorescence of the molecule. However, at the same time, the duration of the dark "off" state remains independent of molecular weight. Again, this may be to be expected because the triplet-state characteristics are inherently monomolecular in nature and highly localized, but it is gratifying to observe this constancy so clearly. The implications of these observations for photovoltaic devices are profound: given the high yield of triplet formation in P3HT following light absorption and the efficient singlet-triplet annihilation in collapsed polymer structures, which would also be expected to form in the film of a device, one may conclude that up to half of the singlet excitons formed upon photoexcitation may be lost non-radiatively by singlet-triplet annihilation. This mechanism then constitutes a competitive loss channel to electron-hole dissociation, limiting the efficiency of solar cells.

Surprisingly, although the triplet states are not affected by molecular weight in collapsed chains of P3HT – monomolecular aggregates – they are quenched in multichain aggregates, thereby limiting the impact of singlet-triplet annihilation as a loss channel in bulk films.[17] This effect could be resolved by growing single multichain aggregates in a controlled fashion, by *in situ* solvent vapor annealing of the dilute polymer sample under the single-molecule microscope.[17] Counting the number of luminescent spots in the microscope image before and after annealing gives an estimate of the number of individual polymer chains making up the single aggregate.[127,226,268,269] Measurement of $g^{(2)}(\Delta t)$ on such nanoparticles revealed signatures of very effective interchain energy transfer in the fact that even multichain aggregates can still show photon antibunching. However, in one and the same measurement on the same nanoparticle, the triplet correlation amplitude in $g^{(2)}(\Delta t)$ is found to be suppressed, implying that even though the singlet-singlet annihilation mechanism remains active, the singlet-triplet annihilation mechanism is suppressed.[17] This suppression can only happen if the triplet state itself is quenched in the multichain aggregate, presumably by dissociation of the triplet into intermolecular charge-pair species of lower energy.

This example highlights the utility of studying intermolecular interactions with photon correlation techniques: moving beyond the limit of the single molecule to mesoscopic objects containing multiple single molecules, thereby providing the first step on the way to understanding the intrinsic properties of bulk materials. The fact that P3HT is used so successfully in photovoltaic applications rather implies that it is not overly emissive and challenging to examine on the single-molecule level with photon correlation techniques.[270,271] Nevertheless, even more effective photovoltaic materials have now been examined using this single-molecule approach, such as the polymer “PTB7”,[272] which has a particularly broad absorption spectrum with favorable overlap with the solar spectrum. In this material, it was also possible to unravel the spectral heterogeneity and identify a range of monomolecular electronic processes, even in larger aggregate structures.[273,274]

VII. MOLECULAR MESOSCOPICS: FROM SINGLE MOLECULES TO BULK MATERIALS

As outlined in the previous section, it is possible to investigate the intermediate regime between single molecules and a bulk film of an organic semiconductor material by controlled deterministic aggregation of single molecules to mesoscopic objects. Two fundamental questions arise with this approach: what sort of electronic interactions exist between molecules, i.e. how do their transition-dipole moments couple with each other in the assembled objects; and how large can a molecular aggregate become to still behave as a mesoscopic source of single photons? The latter question is implicitly related to the ease with which excitation energy can move within the aggregate, since efficient sampling of different molecular sites by migrating excitons will facilitate singlet-singlet annihilation as a prerequisite to single-photon emission. This exciton diffusion on mesoscopic length scales, i.e. over distances larger than the size of the individual molecular constituent, will in turn be implicitly connected to the intermolecular electronic interactions, making this a particularly interesting avenue to explore.

A. Molecular electronic aggregation phenomena

When molecules assemble in aggregates, in solution or in the solid state, two effects may occur with regard to their transition-dipole moments, illustrated in Figure 31. The first effect arises when the dipoles arrange in a “head to tail” configuration. This situation may occur in certain dye molecules, but it is particularly prevalent in a conjugated polymer,[275] which is made up of individual monomer units: the dipoles associated with the individual repeat units all add up, raising the transition oscillator strength. This long-known effect of “J-aggregation”, named after E. E. Jelly’s work in 1936, continues to be of extraordinary relevance in organic electronics. Its impact on the electronic transitions of the aggregate, illustrated in Figure 31a, is threefold:[275] the transition energy will shift to the red, much like the transition energy of a particle delocalized over two quantum wells has a lower eigenenergy than the particle localized in either well. Because of the increase in oscillator strength, the radiative rate will rise, shortening the PL lifetime. At the same time, the increase in coherence of the excited state will limit vibrational coupling, so that the PL spectrum will appear spectrally narrowed to the purely electronic transition with reduced vibronic sidebands. Such intramolecular J-type aggregation will be promoted quite naturally by intermolecular interactions between polymer chains in an aggregate, provided that the side chains of the polymer are sufficiently short so that they do not get entangled with each other, which would hinder alignment. An example of a structure of such a J-aggregate is sketched on the left in Figure 31b. The opposite effect to J-type aggregation is referred to after the hypsochromic shift parallel transition-dipole moments induce: the “H-aggregate”. Now, the transitions become inhibited because the individual dipoles interfere destructively. The excited-state energy levels split again, but the allowed transition now arises from the higher-energy level, which becomes depopulated by internal conversion. The result of this relaxation process is that the hypsochromic shift is only seen in absorption and not in the luminescence of the aggregate. The emission is characterized by a dramatic decrease in the radiative rate and an increase in vibrational coupling. Again, as in the case of the J-aggregate, the emission spectrum will shift to the red with respect to the uncoupled molecule, but, in contrast to the J-aggregates, it will appear spectrally broadened due to the influence of the vibrational modes on the radiative transition: vibrations serve to distort the lattice, breaking the symmetry that prohibits radiative decay from the lowest-energy level, effectively lending oscillator strength to the dipole-forbidden transition.

H-type aggregation is an inherently intermolecular effect so that its strength depends sensitively on the separation between the individual units: H-type electronic coupling is usually entirely suppressed for a spacing of 1 nm between the dipoles. The effect can be probed accurately in dimer and trimer chromophore model systems, where the spacing between the chromophores is set by the molecular scaffold:[276-278] the intramolecularization of intermolecular interactions. In contrast, the molecular arrangement in the aggregate may still be such that long-range intramolecular order is preserved to a certain degree, so that signatures of intramolecular J-type aggregation effects still arise. Both phenomena, however, can be suppressed by decorating the conjugated polymer with bulky side chains, such as polymer brushes, which entangle with each other, inhibiting any long-range ordering. Examples of three such materials, which show H-type coupling, J-type coupling and a suppression of coupling are given in Figure 31c. These three compounds all have the same poly(*para*-phenylene-ethynylenebutadiynylene) (PPEB) π-conjugated backbone, and therefore the same monomolecular electronic and vibrational characteristics, but differ strongly in their assembly properties upon aggregation.[279] The anticipated effect of aggregation is resolved clearly in the comparison of spectra and PL lifetimes obtained on the single-molecule level at room temperature, as shown in Figure 32. The three materials have virtually identical PL spectra and fluorescence lifetime decays on the single-molecule level. Upon aggregation, PPEB-1 shows a dramatic shift in the PL spectrum to the red along with strong broadening to a featureless spectrum, accompanied by a near tenfold increase in the PL lifetime when compared to the isolated polymer chain. In contrast, PPEB-2 exhibits a smaller redshift compared to the isolated molecule, but also shows a pronounced spectral narrowing and a decrease in the PL lifetime. No discernible effect is seen in the spectra of aggregates of PPEB-3 containing bulky side-chains: the aggregate spectra and PL dynamics are virtually identical to those of the isolated chain. PPEB-2 therefore behaves as a J-aggregate, PPEB-1 as an H-aggregate. However, this perspective is a little too simplistic, since the intramolecular ordering should be favored in both molecule species. Although the light emission – the PL spectrum and lifetime – of PPEB-1 is dominated by the H-type character of the intermolecular aggregation, intramolecular J-type aggregation will also arise. Such a combined aggregation phenomenon is referred to as an HJ-type aggregate.[275,278]

The three types of polymer aggregate structures have very different characteristics in terms of their fluorescence photon statistics, shown in Figure 33. The $g^{(2)}(\Delta t)$ histograms are composed of data from approx. 50 single aggregates each. The HJ-aggregate of PPEB-1 shows a clear photon antibunching dip but no signature of photon bunching since the measurement was conducted in air with ambient oxygen. It is quite remarkable that a molecular mesoscopic object containing tens of single polymer chains, with a total molecular weight of several megadalton,[226] still shows such strong photon antibunching. Evidently, excitation energy is swiftly transferred to regions of the molecular aggregate where the interchain coupling is strongest, so that red-shifted emission with a reduced radiative rate occurs. At the same time, however, the emissive species – a strongly coupled H-aggregate – does not show any signatures of intermittency in the luminescence due to either charge separation or triplet shelving, which would both show up as an amplitude in $g^{(2)}(\Delta t)$ at finite delay times. This lack of photon bunching is primarily a consequence of the suppression of triplet formation by exposure to ambient air during measurement; triplet quenching is so strong in these H-type aggregates that photon correlation experiments are not possible under nitrogen when one single triplet state quenches the entire luminescence of the aggregate. This situation contrasts with the aforementioned experiments on P3HT (Section VI.C), which showed a vanishing of the triplet photon bunching peak under nitrogen atmosphere in the multichain aggregate (Section VI.C). The case is very different in Figure 33b for the J-type aggregate of PPEB-2, where strong interchain interactions are suppressed by a slight increase in intermolecular spacing. In this multimolecular structure, where the photophysics is dominated by the strong intrachain J-type coupling, photon antibunching is still observed but with a reduced dip at $\Delta t = 0$ compared to the H-type aggregate. Crucially, however, in this case a clear photon-bunching feature is observed in $g^{(2)}(\Delta t)$, even though the measurement is again performed in air. The photon bunching is described by a single-exponential function of lifetime 1 μs. It is tempting to attribute this amplitude to residual triplet shelving of the excitation cycle occurring in the multimolecular object, given the fact that triplet quenching by oxygen should be reduced in the densely packed aggregate structure embedded in PMMA. However, it is challenging to rationalize why such triplet shelving should be retained in the J-type aggregate structure – which is less densely packed than the H-type aggregate of PPEB-1 – when no photon bunching is seen in the latter. Alternatively, it is conceivable that the less dense packing promotes the formation of metastable charge-transfer states, which are populated by the triplet state. Studies of optically detected magnetic resonance on dye molecules in comparison to the single-molecule fluorescence dynamics demonstrated that this pathway can indeed occur over the intermediate long-lived triplet state, and is promoted by the presence of oxygen, giving rise to long-lived dark states as well as possible irreversible photoreactions arising due to radical formation.[280] Finally, in the disordered aggregate of PPEB-3 chains in Figure 33c, both coupling within and between the polymer chains is found to be suppressed: the photon correlation shows only a minimal dip at $\Delta t = 0$, and again no discernible photon bunching amplitude due to a dark state. The polymer aggregate behaves as a multichromophoric emitter with minimal coupling between the chromophores.

This third case constitutes the rather trivial expectation for the behavior of a multimolecular aggregate: it appears much like one would expect the ensemble of a bulk film to behave. The other two cases are far more interesting. The photon antibunching feature arises because of singlet-singlet annihilation, so it must evolve over a certain timescale as excitation energy diffuses through the mesoscopic object. One would expect this diffusion to be accelerated in the H-type aggregate structure since the polymer chains are in closer proximity to each other than in the J-type aggregate. However, in the H-type aggregate it is not at all clear how many emitting sites should exist within the mesoscopic object, which can easily span tens of nanometers in extension. Strong interchain contact could conceivably exist in different positions within the aggregate, forming different local sinks for excitation energy, and thereby making the H-aggregate a *de facto* multisite emitting structure. Excitation energy may then become trapped in different local energetic minima, without being able to reach the global energetic minimum. Furthermore, exciton theory appears to suggest that exciton-exciton annihilation is coherently suppressed due to the coherent dipole-dipole coupling in H-aggregates, but interestingly not in J-aggregates, owing to the sign of the phase relation between the two dipoles.[281] It is therefore of utmost interest to study the dynamics of the excitons in the individual aggregates.

B. Tracking exciton diffusion and annihilation

With the time-resolved photon antibunching technique discussed in Section IV.B, tested with multichromophoric DNA-origami structures, it is possible to track both exciton diffusion within the conjugated-polymer aggregates as well as to determine the effective number of emitting sites in the aggregate. At short photon arrival times, the strength of the dip of $g^{(2)}(\Delta t)$ at $\Delta t = 0$ will provide a metric for the number of independent chromophores in the system. As the excitons diffuse between these chromophores, singlet-singlet annihilation occurs and the depth of the $g^{(2)}(\Delta t = 0)$ dip increases with delay time. The rate and dynamics of this increase mirror the rates of annihilation and exciton diffusion, and are therefore linked to the underlying dimensionality of exciton diffusion. Figure 34a plots the evolution of the number of independent chromophores emitting in the aggregate, extracted from the $g^{(2)}(\Delta t)$ measurement as described in Section IV.B, as a function of time for the two aggregate types consisting of approximately ten chains each. Striking differences are seen in the dynamics of these two aggregate species. As before, the dataset is arrived at by considering the cumulative photon statistics of several hundred single aggregates. At very short times, both aggregates start out at approximately the same number of independent chromophores, which is determined primarily by the overall size of the aggregate. Whereas the H-type aggregate drops down to near-perfect photon antibunching within approximately 1 ns after excitation, the dynamics in the J-type aggregate are much slower, demonstrating that the processes of exciton diffusion and subsequent exciton-exciton annihilation differ strongly between H- and J-type aggregates. Excitonic diffusion is usually analyzed by considering the rate of change of exciton density with time following a second-order reaction equation. Since the time-resolved photon antibunching measurement does not measure exciton density but rather the effective volume an exciton can map out without annihilating with another one, a metric related to the inverse exciton density is considered here to quantify exciton diffusivity. From the density of the polymer material, the number of chains counted in the aggregate, and the average molecular weight of the polymer, an estimate can be made for the volume of each aggregate, V_{agg}. It can be shown that the rate of change of the excitation density equals the product of the annihilation rate and the bimolecular excitation density $n(n-1)$, where n signifies the number of independently emitting chromophore sites within the aggregate (a complete derivation of this relationship is given in the Supplementary Material of Ref. 153). Therefore, by plotting the logarithm of the quantity $\frac{n}{n-1}$ multiplied by the volume of each aggregate as a function of time, the bimolecular annihilation rate $\gamma = k_{\mathrm{SSA}} V_{\mathrm{Agg}}$, i.e. the product of singlet-singlet annihilation rate and aggregate volume, is determined from the slope of the functionality as indicated in Figure 34b. Three regions of γ are identified in the plots: the slope either varies with time, is constant, or zero. For the second region marked in the figure, the annihilation rate is over ten times greater in the H-aggregate than in the J-aggregate, implying much stronger interactions between the chromophores in the former case. This marked difference in dynamics can be interpreted in terms of the dimensionality of excitonic diffusion in the polymer nanoparticle as illustrated in Figure 34c. For short times, exciton diffusion either occurs along the polymer chain, i.e. in one dimension, or within very small H-aggregate structures consisting of only two chain segments in close proximity.[276] In the latter case, the diffusion can be thought of as occurring in fewer than two dimensions. In the intermediate region of the dynamics, full three-dimensional exciton diffusion occurs, but because the H-aggregates have a higher degree of ordering, which correlates with the greater level of interchain contact, exciton diffusion will be much swifter than in the J-aggregates, where the formation of regions of interchain contact is suppressed. The level of interchain disorder is exaggerated somewhat in this representation for illustration purposes. For the longest delay times of the photons detected, after approximately 2 ns after excitation, singlet-singlet annihilation no longer controls the photon statistics and the slope drops to zero. This cutoff marks an estimate for the time over which excitons can diffuse to encounter a second exciton within the aggregate: the effective diffusion length of excitons in three dimensions L_{3D}. As one would expect,[282] the diffusion lengths stated in the figure are substantially greater for the H-type aggregates than for the J-type aggregates, where the chains are spaced further apart.

Finally, it is also possible to examine the effect of aggregate size on the singlet-singlet annihilation rate. On the one hand, larger aggregates may be expected to offer more molecular sites where excitations are formed, promoting exciton diffusion. On the other hand, the morphology of the aggregate may change with aggregate size, and concomitantly affect the excitonic diffusivity. Figure 34d shows the temporal evolution of the $g^{(2)}(\Delta t)$ measurement, converted to the normalized number of emitting sites per volume element, $\ln\left(\frac{n}{n-1}\right) V_{\mathrm{Agg}}$, for two PPEB-2 J-type aggregates of different sizes, comprising, on average, either six or nine polymer chains. The annihilation rate is clearly greater for the smaller aggregate than for the larger one, implying that molecular ordering indeed deteriorates as the size of the aggregate grows. The time-resolved photon antibunching measurement therefore also offers unique insight into the molecular arrangement and the overall morphology of mesoscopic molecular objects, complementing conventional measurements of microscopic structure by polarization-modulation spectroscopy.[283]

VIII. CONCLUSIONS AND OUTLOOK

It is easy to forget that the human visionary system is only sensitive to changes in light intensity at rates of below a few tens of Hertz. Much information is hidden in the flickering of a light-emitting object, even if it is not resolved by the naked eye. To see such dynamics we need special "glasses" – the intensity autocorrelation. The HBT-type correlation approach offers a prime example of how a particular physical concept and experimental methodology are developed for a very specific application – measuring the size of stars – only to find plentiful applications in entirely unrelated fields of research: in many ways, photon-correlation measurements in luminescence microscopy truly constitute an example of "nanoastronomy", allowing broad taxonomy of the diversity in behavior of single-photon sources. The approach proves useful in a broad range of optoelectronic materials and device structures, in addition to the more commonplace applications in the life sciences. Understanding how light is emitted from an optoelectronic material, i.e. what the sequence of emitted photons is, offers information both on the kind of interactions that exist with excitations in the immediate environment of the emitter, and on the nanoscale arrangement of the light-emitting material itself.

We discussed several promising avenues for further development of spectroscopies relating to luminescence photon statistics, in particular with regards to superresolution fluorescence imaging and ultrafast fluorescence microscopy. For example, with the double-excitation technique presented in Section IV.A, it is, in principle, possible to probe dynamics of single-photon sources on timescales much shorter than the intrinsic excited-state lifetime. In view of the versatility with which photon statistics can be controlled by self-organization processes – be these in polymeric vesicles, in nanocrystal quantum dots, in DNA-origami structures, in the monomolecular morphology of single polymer chains or even in supramolecular aggregates of organic semiconductors, the measurement of fluorescence photon statistics promises to provide a helpful metric to follow nanoscale self-assembly processes *in situ*.

We note that most of the examples discussed here relate to measurements of the photon statistics at room temperature, under ambient conditions, mainly because of the greater ease of working with microscope objectives of large numerical aperture under these conditions. A host of additional effects are expected to arise under cryogenic conditions, where electronic transitions narrow. In particular, in molecular multichromophoric systems and molecular aggregates, one may expect the spectral overlap between donor and acceptor states – both excited states of different chromophores within the system – to decrease sharply, so that both photon antibunching (due to singlet-singlet annihilation) and photon bunching effects (due to singlet-triplet annihilation) are suppressed at low temperatures. Under these conditions, it should become possible to reach much greater excitation densities within a molecular complex, opening the possibility of superradiance effects arising along with the associated acceleration of radiative decay and photon bunching.

Finally, we note that here, we have only focused our attention on the luminescence intensity autocorrelation, while only briefly touching on correlations arising in luminescence color and polarization. Of course, there are more spectroscopic observables which can reveal information on the underlying dynamics of the light-emitting system by a temporal autocorrelation: early on in the spectroscopy of single molecules, molecular dynamics were already probed through an autocorrelation analysis of the fluorescence spectrum.[11,284,285] In addition, the photon counting technique at the heart of the intensity autocorrelation can be used to derive a secondary correlation function, the temporal correlation of the fluorescence lifetime. This variation in time of the PL lifetime has been shown to relate to photoinduced electron transfer events[12] and can be used to probe conformational dynamics of protein structures.[286] Obviously, any secondary spectroscopic observable necessitates the detection of a higher number of photons, thereby limiting the temporal resolution of the autocorrelation analysis. The observable used for the analysis therefore has to be matched to the photon flux and the time scale of the dynamics under consideration.

With this review, we hope to provide some grounding to ensure that the analysis of fluorescence photon statistics will become more broadly used in studies of new luminescent materials, offering a truly microscopic way of examining the mechanisms that limit both the luminescence rate and yield.

Acknowledgements

The authors are indebted to Dr. Felix Hofmann for assistance with assembling the artwork and to Dr. Sebastian Bange for careful review of the manuscript.

Data availability statement

Data sharing is not applicable to this article as no new data were created or analyzed in this study.

References

1 Hanbury Brown, R. & Twiss, R. Q. A new type of interferometer for use in radio astronomy. *Phil. Mag. J. Sci.* **45**, 663 (1954).

2 Hanbury Brown, R. & Twiss, R. Q. Correlation between Photons in two Coherent Beams of Light. *Nature* **177**, 27 (1956).

3 Hanbury Brown, R. & Twiss, R. Q. A Test of a New Type of Stellar Interferometer on Sirius. *Nature* **178**, 1046 (1956).

4 Michelson, A. & Morley, E. W. On the Relative Motion of the Earth and the Luminiferous Æther. *Phil. Mag.* **24**, 5 (1887).

5 Abbott, B. P. & al., e. Observation of Gravitational Waves from a Binary Black Hole Merger. *Phys. Rev. Lett.* **116**, 061102 (2016).

6 Orrit, M. Photon statistics in single molecule experiments. *Single Mol.* **3**, 255 (2002).

7 Einstein, A., Podolsky, B. & Rosen, N. Can Quantum-Mechanical Description of Physical Reality Be Considered Complete? *Phys. Rev.* **47**, 777 (1935).

8 Zeilinger, A. Fundamentals of quantum information. *Phys. World* **11**, 35 (1998).

9 Basché, T., Kummer, S. & Bräuchle, C. Direct spectroscopic observation of quantum jumps of a single-molecule. *Nature* **373**, 132 (1995).

10 Aggarwal, A. V., Thiessen, A., Idelson, A., Kalle, D., Würsch, D., Stangl, T., Steiner, F., Jester, S. S., Vogelsang, J., Höger, S. & Lupton, J. M. Fluctuating exciton localization in giant pi-conjugated spoked-wheel macrocycles. *Nat. Chem.* **5**, 964 (2013).

11 Lu, H. P. & Xie, X. S. Single-molecule spectral fluctuations at room temperature. *Nature* **385**, 143 (1997).

12 Cotlet, M., Masuo, S., Luo, G. B., Hofkens, J., Van der Auweraer, M., Verhoeven, J., Müllen, K., Xie, X. L. S. & De Schryver, F. Probing conformational dynamics in single donor-acceptor synthetic molecules by means of photoinduced reversible electron transfer. *Proc. Natl. Acad. Sci. U. S. A.* **101**, 14343 (2004).

13 Basché, T., Moerner, W. E., Orrit, M. & Talon, H. Photon antibunching in the fluorescence of a single dye molecule trapped in a solid. *Phys. Rev. Lett.* **69**, 1516 (1992).

14 Tinnefeld, P., Müller, C. & Sauer, M. Time-varying photon probability distribution of individual molecules at room temperature. *Chem. Phys. Lett.* **345**, 252 (2001).

15 Weston, K. D., Dyck, M., Tinnefeld, P., Müller, C., Herten, D. P. & Sauer, M. Measuring the number of independent emitters in single-molecule fluorescence images and trajectories using coincident photons. *Anal. Chem.* **74**, 5342 (2002).

16 Verberk, R. & Orrit, M. Photon statistics in the fluorescence of single molecules and nanocrystals: Correlation functions versus distributions of on- and off-times. *J. Chem. Phys.* **119**, 2214 (2003).

17 Steiner, F., Lupton, J. M. & Vogelsang, J. Role of Triplet-State Shelving in Organic Photovoltaics: Single-Chain Aggregates of Poly(3-hexylthiophene) versus Mesoscopic Multichain Aggregates. *J. Am. Chem. Soc.* **139**, 9787 (2017).

18 He, Y. & Barkai, E. Super- and sub-Poissonian photon statistics for single molecule spectroscopy. *J. Chem. Phys.* **122**, 184703 (2005).

19 Brokmann, X., Bawendi, M., Coolen, L. & Hermier, J. P. Photon-correlation Fourier spectroscopy. *Opt. Express* **14**, 6333 (2006).

20 Utzat, H., Sun, W. W., Kaplan, A. E. K., Krieg, F., Ginterseder, M., Spokoyny, B., Klein, N. D., Shulenberger, K. E., Perkinson, C. F., Kovalenko, M. V. & Bawendi, M. G. Coherent single-photon emission from colloidal lead halide perovskite quantum dots. *Science* **363**, 1068 (2019).

21 Bergquist, J. C., Hulet, R. G., Itano, W. M. & Wineland, D. J. Observation of quantum jumps in a single atom. *Phys. Rev. Lett.* **57**, 1699 (1986).

22 Cook, R. J. & Kimble, H. J. Possibility of direct observation of quantum jumps. *Phys. Rev. Lett.* **54**, 1023 (1985).

23 Sauter, T., Neuhauser, W., Blatt, R. & Toschek, P. E. Observation of quantum jumps. *Phys. Rev. Lett.* **57**, 1696 (1986).

24 Hübner, C. G., Renn, A., Renge, I. & Wild, U. P. Direct observation of the triplet lifetime quenching of single dye molecules by molecular oxygen. *J. Chem. Phys.* **115**, 9619 (2001).

25 Schindler, F., Lupton, J. M., Feldmann, J. & Scherf, U. Controlled fluorescence bursts from conjugated polymers induced by triplet quenching. *Adv. Mater.* **16**, 653 (2004).

26 Bernard, J., Fleury, L., Talon, H. & Orrit, M. Photon bunching in the fluorescence from single molecules - a probe for intersystem crossing. *J. Chem. Phys.* **98**, 850 (1993).

27 Kuno, M., Fromm, D. P., Hamann, H. F., Gallagher, A. & Nesbitt, D. J. Nonexponential "blinking" kinetics of single CdSe quantum dots: A universal power law behavior. *J. Chem. Phys.* **112**, 3117 (2000).

28 Lippitz, M., Kulzer, F. & Orrit, M. Statistical evaluation of single nano-object fluorescence. *Chem. Phys. Chem.* **6**, 770 (2005).

29 Verberk, R., van Oijen, A. M. & Orrit, M. Simple model for the power-law blinking of single semiconductor nanocrystals. *Phys. Rev. B* **66**, 233202 (2002).

30 Houel, J., Doan, Q. T., Cajgfinger, T., Ledoux, G., Amans, D., Aubret, A., Dominjon, A., Ferriol, S., Barbier, R., Nasilowski, M., Lhuillier, E., Dubertret, B., Dujardin, C. & Kulzer, F. Autocorrelation Analysis for the Unbiased Determination of Power-Law Exponents in Single-Quantum-Dot Blinking. *ACS Nano* **9**, 886 (2015).

31 Empedocles, S. A. & Bawendi, M. G. Quantum-confined stark effect in single CdSe nanocrystallite quantum dots. *Science* **278**, 2114 (1997).

32 Müller, J., Lupton, J. M., Lagoudakis, P. G., Schindler, F., Koeppe, R., Rogach, A. L., Feldmann, J., Talapin, D. V. & Weller, H. Wave function engineering in elongated semiconductor nanocrystals with heterogeneous carrier confinement. *Nano Lett.* **5**, 2044 (2005).

33 Galland, C., Ghosh, Y., Steinbruck, A., Sykora, M., Hollingsworth, J. A., Klimov, V. I. & Htoon, H. Two types of luminescence blinking revealed by spectroelectrochemistry of single quantum dots. *Nature* **479**, 203 (2011).

34 van Schooten, K. J., Boehme, C. & Lupton, J. M. Coherent Magnetic Resonance of Nanocrystal Quantum-Dot Luminescence as a Window to Blinking Mechanisms. *Chem. Phys. Chem.* **15**, 1737 (2014).

35 Müller, J., Lupton, J. M., Rogach, A. L., Feldmann, J., Talapin, D. V. & Weller, H. Air-induced fluorescence bursts from single semiconductor nanocrystals. *Appl. Phys. Lett.* **85**, 381 (2004).

36 Cichos, F., von Borczyskowski, C. & Orrit, M. Power-law intermittency of single emitters. *Curr. Op. Coll. Int. Sci.* **12**, 272 (2007).

37 Santori, C., Fattal, D., Vuckovic, J., Solomon, G. S., Waks, E. & Yamamoto, Y. Submicrosecond correlations in photoluminescence from InAs quantum dots. *Phys. Rev. B* **69**, 205324 (2004).

38 Davanco, M., Hellberg, C. S., Ates, S., Badolato, A. & Srinivasan, K. Multiple time scale blinking in InAs quantum dot single-photon sources. *Phys. Rev. B* **89**, 161303 (2014).

39 Bayer, M., Stern, O., Hawrylak, P., Fafard, S. & Forchel, A. Hidden symmetries in the energy levels of excitonic 'artificial atoms'. *Nature* **405**, 923 (2000).

40 Banin, U., Cao, Y. W., Katz, D. & Millo, O. Identification of atomic-like electronic states in indium arsenide nanocrystal quantum dots. *Nature* **400**, 542 (1999).

41 Michler, P., Imamoglu, A., Mason, M. D., Carson, P. J., Strouse, G. F. & Buratto, S. K. Quantum correlation among photons from a single quantum dot at room temperature. *Nature* **406**, 968 (2000).

42 Hübner, C. G., Zumofen, G., Renn, A., Herrmann, A., Müllen, K. & Basché, T. Photon antibunching and collective effects in the fluorescence of single bichromophoric molecules. *Phys. Rev. Lett.* **91**, 093903 (2003).

43 Tinnefeld, P., Weston, K. D., Vosch, T., Cotlet, M., Weil, T., Hofkens, J., Müllen, K., De Schryver, F. C. & Sauer, M. Antibunching in the emission of a single tetrachromophoric dendritic system. *J. Am. Chem. Soc.* **124**, 14310 (2002).

44 VandenBout, D. A., Yip, W. T., Hu, D. H., Fu, D. K., Swager, T. M. & Barbara, P. F. Discrete intensity jumps and intramolecular electronic energy transfer in the spectroscopy of single conjugated polymer molecules. *Science* **277**, 1074 (1997).

45 Lim, T. S., Hsiang, J. C., White, J. D., Hsu, J. H., Fan, Y. L., Lin, K. F. & Fann, W. S. Single short-chain conjugated polymer studied with optical spectroscopy: A donor-accepter system. *Phys. Rev. B* **75**, 165204 (2007).

46 Huser, T., Yan, M. & Rothberg, L. J. Single chain spectroscopy of conformational dependence of conjugated polymer photophysics. *Proc. Natl. Acad. Sci. U. S. A.* **97**, 11187 (2000).

47 Hollars, C. W., Lane, S. M. & Huser, T. Controlled non-classical photon emission from single conjugated polymer molecules. *Chem. Phys. Lett.* **370**, 393 (2003).

48 Sanchez-Mosteiro, G., Koopman, M., van Dijk, E., Hernando, J., van Hulst, N. F. & Garcia-Parajo, M. F. Photon antibunching proves emission from a single subunit in the autofluorescent protein DsRed. *Chem. Phys. Chem.* **5**, 1782 (2004).

49 Hofkens, J., Cotlet, M., Vosch, T., Tinnefeld, P., Weston, K. D., Ego, C., Grimsdale, A., Müllen, K., Beljonne, D., Brédas, J. L., Jordens, S., Schweitzer, G., Sauer, M. & De Schryver, F. Revealing competitive Förster-type resonance energy-transfer pathways in single bichromophoric molecules. *Proc. Natl. Acad. Sci. U. S. A.* **100**, 13146 (2003).

50 Barzda, V., Gulbinas, V., Kananavicius, R., Cervinskas, V., van Amerongen, H., van Grondelle, R. & Valkunas, L. Singlet-singlet annihilation kinetics in aggregates and trimers of LHCII. *Biophys. J.* **80**, 2409 (2001).

51 Yu, J., Lammi, R., Gesquiere, A. J. & Barbara, P. F. Singlet-triplet and triplet-triplet interactions in conjugated polymer single molecules. *J. Phys. Chem. B* **109**, 10025 (2005).

52 Fückel, B., Hinze, G., Nolde, F., Müllen, K. & Basché, T. Quantification of the Singlet-Singlet Annihilation Times of Individual Bichromophoric Molecules by Photon Coincidence Measurements. *J. Phys. Chem. A* **114**, 7671 (2010).

53 Hernando, J., Hoogenboom, J. P., van Dijk, E., Garcia-Lopez, J. J., Crego-Calama, M., Reinhoudt, D. N., van Hulst, N. F. & Garcia-Parajo, M. F. Single molecule photobleaching probes the exciton wave function in a multichromophoric system. *Phys. Rev. Lett.* **93**, 236404 (2004).

54 Baldo, M. A., Holmes, R. J. & Forrest, S. R. Prospects for electrically pumped organic lasers. *Phys. Rev. B* **66**, 035321 (2002).

55 Baker, W. J., McCamey, D. R., van Schooten, K. J., Lupton, J. M. & Boehme, C. Differentiation between polaron-pair and triplet-exciton polaron spin-dependent mechanisms in organic light-emitting diodes by coherent spin beating. *Phys. Rev. B* **84**, 165205 (2011).

56 Gesquière, A. J., Park, S. J. & Barbara, P. F. Hole-induced quenching of triplet and singlet excitons in conjugated polymers. *J. Am. Chem. Soc.* **127**, 9556 (2005).

57 Schedlbauer, J., Scherf, U., Vogelsang, J. & Lupton, J. M. Dynamic Quenching of Triplet Excitons in Single Conjugated-Polymer Chains. *J. Phys. Chem. Lett.* **11**, 5192 (2020).

58 Hettich, C., Schmitt, C., Zitzmann, J., Kuhn, S., Gerhardt, I. & Sandoghdar, V. Nanometer resolution and coherent optical dipole coupling of two individual molecules. *Science* **298**, 385 (2002).

59 Gross, M. & Haroche, S. Super-radiance - an essay on the theory of collective spontaneous emission. *Phys. Rep.* **93**, 301 (1982).

60 Fidder, H., Knoester, J. & Wiersma, D. A. Superradiant emission and optical dephasing in J-aggregates. *Chem. Phys. Lett.* **171**, 529 (1990).

61 Luo, Y., Chen, G., Zhang, Y., Zhang, L., Yu, Y. J., Kong, F. F., Tian, X. J., Zhang, Y., Shan, C. X., Luo, Y., Yang, J. L., Sandoghdar, V., Dong, Z. C. & Hou, J. G. Electrically Driven Single-Photon Superradiance from Molecular Chains in a Plasmonic Nanocavity. *Phys. Rev. Lett.* **122**, 233901 (2019).

62 Raino, G., Becker, M. A., Bodnarchuk, M. I., Mahrt, R. F., Kovalenko, M. V. & Stoferle, T. Superfluorescence from lead halide perovskite quantum dot superlattices. *Nature* **563**, 671 (2018).

63 Raino, G., Utzat, H., Bawendi, M. G. & Kovalenko, M. V. Superradiant emission from self-assembled light emitters: From molecules to quantum dots. *MRS Bull.* **45**, 841 (2020).

64 Bradac, C., Johnsson, M. T., van Breugel, M., Baragiola, B., Martin, R., Juan, M. L., Brennen, G. K. & Volz, T. Room-temperature spontaneous superradiance from single diamond nanocrystals. *Nat. Commun.* **8**, 1205 (2017).

65 Waters, D. P., Joshi, G., Kavand, M., Limes, M. E., Malissa, H., Burn, P. L., Lupton, J. M. & Boehme, C. The spin-Dicke effect in OLED magnetoresistance. *Nat. Phys.* **11**, 910 (2015).

66 Jamali, S., Mkhitaryan, V. V., Malissa, H., Nahlawi, A., Popli, H., Gruenbaum, T., Bange, S., Milster, S., Stoltzfus, D. M., Leung, A. E., Darwish, T. A., Burn, P. L., Lupton, J. M. & Boehme, C. Floquet spin states in OLEDs. *Nat. Commun.* **12**, 465 (2021).

67 Kavand, M., Baird, D., van Schooten, K., Malissa, H., Lupton, J. M. & Boehme, C. Discrimination between spin-dependent charge transport and spin-dependent recombination in pi-conjugated polymers by correlated current and electroluminescence-detected magnetic resonance. *Phys. Rev. B* **94** (2016).

68 Elson, E. L. & Magde, D. Fluorescence correlation spectroscopy. 1. Conceptual basis and theory. *Biopolymers* **13**, 1 (1974).

69 Magde, D., Elson, E. L. & Webb, W. W. Fluorescence correlation spectroscopy. 2. Experimental realization. *Biopolymers* **13**, 29 (1974).

70 Aragon, S. R. & Pecora, R. Fluorescence correlation spectroscopy as a probe of molecular-dynamics. *J. Chem. Phys.* **64**, 1791 (1976).

71 Haustein, E. & Schwille, P. Fluorescence correlation spectroscopy: Novel variations of an established technique. *Annu. Rev. Biophys.* **36**, 151 (2007).

72 Rigler, R., Mets, U., Widengren, J. & Kask, P. Fluorescence correlation spectroscopy with high count rate and low-background - analysis of translational diffusion *Eur. Biophys. J.* **22**, 169 (1993).

73 Eigen, M. & Rigler, R. Sorting single molecules - application to diagnostics and evolutionary biotechnology. *Proc. Natl. Acad. Sci. U. S. A.* **91**, 5740 (1994).

74 Widengren, J., Mets, U. & Rigler, R. Fluorescence correlation spectroscopy of triplet-states in solution - a theoretical and experimental-study. *J. Phys. Chem.* **99**, 13368 (1995).

75 Verbrugge, S., Kapitein, L. C. & Peterman, E. J. G. Kinesin moving through the spotlight: Single-motor fluorescence microscopy with submillisecond time resolution. *Biophys. J.* **92**, 2536 (2007).

76 Sharma, A., Enderlein, J. & Kumbhakar, M. Photon Antibunching in Complex Intermolecular Fluorescence Quenching Kinetics. *J. Phys. Chem. Lett.* **7**, 3137 (2016).

77 Sharma, A., Enderlein, J. & Kumbhakar, M. Photon Antibunching Reveals Static and Dynamic Quenching Interaction of Tryptophan with Atto-655. *J. Phys. Chem. Lett.* **8**, 5821 (2017).

78 Kondo, T., Chen, W. J. & Schlau-Cohen, G. S. Single-Molecule Fluorescence Spectroscopy of Photosynthetic Systems. *Chem. Rev.* **117**, 860 (2017).

79 Synge, E. H. XXXVIII. A suggested method for extending microscopic resolution into the ultra-microscopic region. *Phil. Mag. J. Sci.* **6**, 356 (1928).

80 Hell, S. W. Far-field optical nanoscopy. *Science* **316**, 1153 (2007).

81 Bates, M., Huang, B. & Zhuang, X. W. Super-resolution microscopy by nanoscale localization of photo-switchable fluorescent probes. *Curr. Op. Chem. Biol.* **12**, 505 (2008).

82 Dedecker, P., Flors, C., Hotta, J. I., Uji-I, H. & Hofkens, J. 3D nanoscopy: Bringing biological nanostructures into sharp focus. *Angew. Chem. Int. Ed.* **46**, 8330 (2007).

83 Gould, T. J. & Hess, S. T. Nanoscale Biological Fluorescence Imaging: Breaking the Diffraction Barrier. *Meth. Cell Biol.* **89**, 329 (2008).

84 Huang, B., Bates, M. & Zhuang, X. W. Super-Resolution Fluorescence Microscopy. *Annu. Rev. Biochem.* **78**, 993 (2009).

85 Betzig, E., Patterson, G. H., Sougrat, R., Lindwasser, O. W., Olenych, S., Bonifacino, J. S., Davidson, M. W., Lippincott-Schwartz, J. & Hess, H. F. Imaging intracellular fluorescent proteins at nanometer resolution. *Science* **313**, 1642 (2006).

86 Eggeling, C., Ringemann, C., Medda, R., Schwarzmann, G., Sandhoff, K., Polyakova, S., Belov, V. N., Hein, B., von Middendorff, C., Schonle, A. & Hell, S. W. Direct observation of the nanoscale dynamics of membrane lipids in a living cell. *Nature* **457**, 1159 (2009).

87 Krichevsky, O. & Bonnet, G. Fluorescence correlation spectroscopy: the technique and its applications. *Rep. Prog. Phys.* **65**, 251 (2002).

88 Cui, J. M., Sun, F. W., Chen, X. D., Gong, Z. J. & Guo, G. C. Quantum Statistical Imaging of Particles without Restriction of the Diffraction Limit. *Phys. Rev. Lett.* **110**, 153901 (2013).

89 Schwartz, O., Levitt, J. M., Tenne, R., Itzhakov, S., Deutsch, Z. & Oron, D. Superresolution Microscopy with Quantum Emitters. *Nano Lett.* **13**, 5832 (2013).

90 Tenne, R., Rossman, U., Rephael, B., Israel, Y., Krupinski-Ptaszek, A., Lapkiewicz, R., Silberberg, Y. & Oron, D. Super-resolution enhancement by quantum image scanning microscopy. *Nat. Photon.* **13**, 116 (2019).

91 Ha, T. & Tinnefeld, P. Photophysics of Fluorescent Probes for Single-Molecule Biophysics and Super-Resolution Imaging. *Annu. Rev. Phys. Chem.* **63**, 595 (2012).

92 Lounis, B. & Orrit, M. Single-photon sources. *Rep. Prog. Phys.* **68**, 1129 (2005).

93 Kimble, H. J., Dagenais, M. & Mandel, L. Photon anti-bunching in resonance fluorescence. *Phys. Rev. Lett.* **39**, 691 (1977).

94 Diedrich, F. & Walther, H. Nonclassical radiation of a single stored ion. *Phys. Rev. Lett.* **58**, 203 (1987).

95 Short, R. & Mandel, L. Observation of sub-Poissonian photon statistics. *Phys. Rev. Lett.* **51**, 384 (1983).

96 Ambrose, W. P., Goodwin, P. M., Enderlein, J., Semin, D. J., Martin, J. C. & Keller, R. A. Fluorescence photon antibunching from single molecules on a surface. *Chem. Phys. Lett.* **269**, 365 (1997).

97 Fleury, L., Segura, J. M., Zumofen, G., Hecht, B. & Wild, U. P. Nonclassical photon statistics in single-molecule fluorescence at room temperature. *Phys. Rev. Lett.* **84**, 1148 (2000).

98 Lounis, B. & Moerner, W. E. Single photons on demand from a single molecule at room temperature. *Nature* **407**, 491 (2000).

99 Kim, J., Benson, O., Kan, H. & Yamamoto, Y. A single-photon turnstile device. *Nature* **397**, 500 (1999).

100 Michler, P., Kiraz, A., Becher, C., Schoenfeld, W. V., Petroff, P. M., Zhang, L. D., Hu, E. & Imamoglu, A. A quantum dot single-photon turnstile device. *Science* **290**, 2282 (2000).

101 Kurtsiefer, C., Mayer, S., Zarda, P. & Weinfurter, H. Stable solid-state source of single photons. *Phys. Rev. Lett.* **85**, 290 (2000).

102 Högele, A., Galland, C., Winger, M. & Imamoglu, A. Photon antibunching in the photoluminescence spectra of a single carbon nanotube. *Phys. Rev. Lett.* **100**, 217401 (2008).

103 Endo, T., Ishi-Hayase, J. & Maki, H. Photon antibunching in single-walled carbon nanotubes at telecommunication wavelengths and room temperature. *Appl. Phys. Lett.* **106**, 113106 (2015).

104 Yuan, Z. L., Kardynal, B. E., Stevenson, R. M., Shields, A. J., Lobo, C. J., Cooper, K., Beattie, N. S., Ritchie, D. A. & Pepper, M. Electrically driven single-photon source. *Science* **295**, 102 (2002).

105 Shields, A. J. Semiconductor quantum light sources. *Nat. Photon.* **1**, 215 (2007).

106 Mizuochi, N., Makino, T., Kato, H., Takeuchi, D., Ogura, M., Okushi, H., Nothaft, M., Neumann, P., Gali, A., Jelezko, F., Wrachtrup, J. & Yamasaki, S. Electrically driven single-photon source at room temperature in diamond. *Nat. Photon.* **6**, 299 (2012).

107 Lohrmann, A., Pezzagna, S., Dobrinets, I., Spinicelli, P., Jacques, V., Roch, J. F., Meijer, J. & Zaitsev, A. M. Diamond based light-emitting diode for visible single-photon emission at room temperature. *Appl. Phys. Lett.* **99**, 251106 (2011).

108 Quitsch, W., Kummell, T., Gust, A., Kruse, C., Hommel, D. & Bacher, G. Electrically driven single photon emission from a CdSe/ZnSSe single quantum dot at 200 K. *Appl. Phys. Lett.* **105**, 091102 (2014).

109 He, X., Htoon, H., Doorn, S. K., Pernice, W. H. P., Pyatkov, F., Krupke, R., Jeantet, A., Chassagneux, Y. & Voisin, C. Carbon nanotubes as emerging quantum-light sources. *Nat. Mater.* **17**, 663 (2018).

110 Khasminskaya, S., Pyatkov, F., Slowik, K., Ferrari, S., Kahl, O., Kovalyuk, V., Rath, P., Vetter, A., Hennrich, F., Kappes, M. M., Gol'tsman, G., Korneev, A., Rockstuhl, C., Krupke, R. & Pernice, W. H. P. Fully integrated quantum photonic circuit with an electrically driven light source. *Nat. Photon.* **10**, 727 (2016).

111 Lin, X., Dai, X. L., Pu, C. D., Deng, Y. Z., Niu, Y., Tong, L. M., Fang, W., Jin, Y. Z. & Peng, X. G. Electrically-driven single-photon sources based on colloidal quantum dots with near-optimal antibunching at room temperature. *Nat. Commun.* **8**, 1132 (2017).

112 Nothaft, M., Hohla, S., Jelezko, F., Fruhauf, N., Pflaum, J. & Wrachtrup, J. Electrically driven photon antibunching from a single molecule at room temperature. *Nat. Commun.* **3**, 628 (2012).

113 O'Brien, J. L. Optical quantum computing. *Science* **318**, 1567 (2007).

114 Wang, D. Q., Kelkar, H., Martin-Cano, D., Rattenbacher, D., Shkarin, A., Utikal, T., Götzinger, S. & Sandoghdar, V. Turning a molecule into a coherent two-level quantum system. *Nat. Phys.* **15**, 483 (2019).

115 Assmann, M., Veit, F., Bayer, M., Gies, C., Jahnke, F., Reitzenstein, S., Höfling, S., Worschech, L. & Forchel, A. Ultrafast tracking of second-order photon correlations in the emission of quantum-dot microresonator lasers. *Phys. Rev. B* **81**, 165314 (2010).

116 Assmann, M., Veit, F., Bayer, M., van der Poel, M. & Hvam, J. M. Higher-Order Photon Bunching in a Semiconductor Microcavity. *Science* **325**, 297 (2009).

117 Jahnke, F., Gies, C., Assmann, M., Bayer, M., Leymann, H. A. M., Foerster, A., Wiersig, J., Schneider, C., Kamp, M. & Höfling, S. Giant photon bunching, superradiant pulse emission and excitation trapping in quantum-dot nanolasers. *Nat. Commun.* **7**, 11540 (2016).

118 Kazimierczuk, T., Schmutzler, J., Assmann, M., Schneider, C., Kamp, M., Höfling, S. & Bayer, M. Photon-Statistics Excitation Spectroscopy of a Quantum-Dot Micropillar Laser. *Phys. Rev. Lett.* **115**, 027401 (2015).

119 Wiersig, J., Gies, C., Jahnke, F., Assmann, M., Berstermann, T., Bayer, M., Kistner, C., Reitzenstein, S., Schneider, C., Höfling, S., Forchel, A., Kruse, C., Kalden, J. & Hommel, D. Direct observation of correlations between individual photon emission events of a microcavity laser. *Nature* **460**, 245 (2009).

120 Temnov, V. V. & Woggon, U. Photon statistics in the cooperative spontaneous emission. *Opt. Express* **17**, 5774 (2009).

121 Klaas, M., Schlottmann, E., Flayac, H., Laussy, F. P., Gericke, F., Schmidt, M., von Helversen, M., Beyer, J., Brodbeck, S., Suchomel, H., Höfling, S., Reitzenstein, S. & Schneider, C. Photon-Number-Resolved Measurement of an Exciton-Polariton Condensate. *Phys. Rev. Lett.* **121**, 047401 (2018).

122 Kasprzak, J., Richard, M., Kundermann, S., Baas, A., Jeambrun, P., Keeling, J. M. J., Marchetti, F. M., Szymanska, M. H., Andre, R., Staehli, J. L., Savona, V., Littlewood, P. B., Deveaud, B. & Dang, L. S. Bose-Einstein condensation of exciton polaritons. *Nature* **443**, 409 (2006).

123 Plumhof, J. D., Stöferle, T., Mai, L. J., Scherf, U. & Mahrt, R. F. Room-temperature Bose-Einstein condensation of cavity exciton-polaritons in a polymer. *Nat. Mater.* **13**, 248 (2014).

124 Schmitt, J., Damm, T., Dung, D., Wahl, C., Vewinger, F., Klaers, J. & Weitz, M. Spontaneous Symmetry Breaking and Phase Coherence of a Photon Bose-Einstein Condensate Coupled to a Reservoir. *Phys. Rev. Lett.* **116**, 033604 (2016).

125 Klaers, J., Schmitt, J., Vewinger, F. & Weitz, M. Bose-Einstein condensation of photons in an optical microcavity. *Nature* **468**, 545 (2010).

126 Kulzer, F., Xia, T. & Orrit, M. Single Molecules as Optical Nanoprobes for Soft and Complex Matter. *Angew. Chem. Int. Ed.* **49**, 854 (2010).

127 Vogelsang, J., Brazard, J., Adachi, T., Bolinger, J. C. & Barbara, P. F. Watching the Annealing Process One Polymer Chain at a Time. *Angew. Chem. Int. Ed.* **50**, 2257 (2011).

128 Bonne, T. B., Ludtke, K., Jordan, R. & Papadakis, C. M. Effect of polymer architecture of amphiphilic poly(2-oxazoline) copolymers on the aggregation and aggregate structure. *Macromol. Chem. Phys.* **208**, 1402 (2007).

129 Wang, D. P., Yuan, Y., Mardiyati, Y., Bubeck, C. & Koynov, K. From Single Chains to Aggregates, How Conjugated Polymers Behave in Dilute Solutions. *Macromolecules* **46**, 6217 (2013).

130 Schaeffel, D., Staff, R. H., Butt, H. J., Landfester, K., Crespy, D. & Koynov, K. Fluorescence Correlation Spectroscopy Directly Monitors Coalescence During Nanoparticle Preparation. *Nano Lett.* **12**, 6012 (2012).

131 Ghosh, I., Ghosh, T., Bardagi, J. I. & König, B. Reduction of aryl halides by consecutive visible light-induced electron transfer processes. *Science* **346**, 725 (2014).

132 Ghosh, I., Marzo, L., Das, A., Shaikh, R. & König, B. Visible Light Mediated Photoredox Catalytic Arylation Reactions. *Acc. Chem. Res.* **49**, 1566 (2016).

133 Romero, N. A. & Nicewicz, D. A. Organic Photoredox Catalysis. *Chem. Rev.* **116**, 10075 (2016).

134 Adachi, T., Vogelsang, J. & Lupton, J. M. Unraveling the Electronic Heterogeneity of Charge Traps in Conjugated Polymers by Single-Molecule Spectroscopy. *J. Phys. Chem. Lett.* **5**, 573 (2014).

135 Christ, T., Kulzer, F., Bordat, P. & Basché, T. Watching the photo-oxidation of a single aromatic hydrocarbon molecule. *Angew. Chem. Int. Ed.* **40**, 4192 (2001).

136 Vester, M., Staut, T., Enderlein, J. & Jung, G. Photon Antibunching in a Cyclic Chemical Reaction Scheme. *J. Phys. Chem. Lett.* **6**, 1149 (2015).

137 Haimerl, J., Ghosh, I., König, B., Vogelsang, J. & Lupton, J. M. Single-molecule photoredox catalysis. *Chem. Sci.* **10**, 681 (2019).

138 Haimerl, J. M., Ghosh, I., Koenig, B., Lupton, J. M. & Vogelsang, J. Chemical Photocatalysis with Rhodamine 6G: Investigation of Photoreduction by Simultaneous Fluorescence Correlation Spectroscopy and Fluorescence Lifetime Measurements. *J. Phys. Chem. B* **122**, 10728 (2018).

139 Gosztola, D., Niemczyk, M. P., Svec, W., Lukas, A. S. & Wasielewski, M. R. Excited doublet states of electrochemically generated aromatic imide and diimide radical anions. *J. Phys. Chem. A* **104**, 6545 (2000).

140 Marchini, M., Bergamini, G., Cozzi, P. G., Ceroni, P. & Balzani, V. Photoredox Catalysis: The Need to Elucidate the Photochemical Mechanism. *Angew. Chem. Int. Ed.* **56**, 12820 (2017).

141 Schedlbauer, J., Wilhelm, P., Grabenhorst, L., Federl, M. E., Lalkens, B., Hinderer, F., Scherf, U., Höger, S., Tinnefeld, P., Bange, S., Vogelsang, J. & Lupton, J. M. Ultrafast Single-Molecule Fluorescence Measured by Femtosecond Double-Pulse Excitation Photon Antibunching. *Nano Lett.* **20**, 1074 (2020).

142 Becker, K., Lagoudakis, P. G., Gaefke, G., Höger, S. & Lupton, J. M. Exciton accumulation in pi-conjugated wires encapsulated by light-harvesting macrocycles. *Angew. Chem. Int. Ed.* **46**, 3450 (2007).

143 Becker, K., Gaefke, G., Rolffs, J., Höger, S. & Lupton, J. M. Quantitative mass determination of conjugated polymers for single molecule conformation analysis: enhancing rigidity with macrocycles. *Chem. Commun.* **46**, 4686 (2010).

144 Feynman, R. P. *The Feynman Lectures on Physics, Vol. I, Chapter 32. Addison-Wesley (1964)*. Vol. 32 (Addison-Wesley).

145 Barnes, W. L. Fluorescence near interfaces: the role of photonic mode density. *Journal of Modern Optics* **45**, 661 (1998).

146 Lakowicz, J. R. Radiative decay engineering: Biophysical and biomedical applications. *Anal. Biochem.* **298**, 1 (2001).

147 Huang, J.-S., Feichtner, T., Biagioni, P. & Hecht, B. Impedance Matching and Emission Properties of Nanoantennas in an Optical Nanocircuit. *Nano Lett.* **9**, 1897 (2009).

148 Kinkhabwala, A., Yu, Z. F., Fan, S. H., Avlasevich, Y., Müllen, K. & Moerner, W. E. Large single-molecule fluorescence enhancements produced by a bowtie nanoantenna. *Nat. Photon.* **3**, 654 (2009).

149 Hoang, T. B., Akselrod, G. M. & Mikkelsen, M. H. Ultrafast Room-Temperature Single Photon Emission from Quantum Dots Coupled to Plasmonic Nanocavities. *Nano Lett.* **16**, 270 (2016).

150 Haug, T., Klemm, P., Bange, S. & Lupton, J. M. Hot-Electron Intraband Luminescence from Single Hot Spots in Noble-Metal Nanoparticle Films. *Phys. Rev. Lett.* **115**, 067403 (2015).

151 Roloff, L., Klemm, P., Gronwald, I., Huber, R., Lupton, J. M. & Bange, S. Light Emission from Gold Nanoparticles under Ultrafast Near-Infrared Excitation: Thermal Radiation, Inelastic Light Scattering, or Multiphoton Luminescence? *Nano Lett.* **17**, 7914 (2017).

152 Poellmann, C., Steinleitner, P., Leierseder, U., Nagler, P., Plechinger, G., Porer, M., Bratschitsch, R., Schüller, C., Korn, T. & Huber, R. Resonant internal quantum transitions and femtosecond radiative decay of excitons in monolayer WSe2. *Nat. Mater.* **14**, 889 (2015).

153 Hedley, G. J., Schröder, T., Steiner, F., Eder, T., Hofmann, F., Bange, S., Laux, D., Höger, S., Tinnefeld, P., Lupton, J. M. & Vogelsang, J. Picosecond time-resolved antibunching measures nanoscale exciton motion and the true number of chromophores. *Nat. Commun.* **12**, 1327 (2021).

154 Rundquist, A., Bajcsy, M., Majumdar, A., Sarmiento, T., Fischer, K., Lagoudakis, K. G., Buckley, S., Piggott, A. Y. & Vuckovic, J. Nonclassical higher-order photon correlations with a quantum dot strongly coupled to a photonic-crystal nanocavity. *Phys. Rev. A* **90**, 023846 (2014).

155 Amgar, D., Yang, G. L., Tenne, R. & Oron, D. Higher-Order Photon Correlation as a Tool To Study Exciton Dynamics in Quasi-2D Nanoplatelets. *Nano Lett.* **19**, 8741 (2019).

156 Ta, H., Wolfrum, J. & Herten, D. P. An Extended Scheme for Counting Fluorescent Molecules by Photon-Antibunching. *Laser Phys.* **20**, 119 (2010).

157 Kurz, A., Schmied, J. J., Grussmayer, K. S., Holzmeister, P., Tinnefeld, P. & Herten, D. P. Counting Fluorescent Dye Molecules on DNA Origami by Means of Photon Statistics. *Small* **9**, 4061 (2013).

158 Grussmayer, K. S., Kurz, A. & Herten, D. P. Single-Molecule Studies on the Label Number Distribution of Fluorescent Markers. *Chem. Phys. Chem.* **15**, 734 (2014).

159 Grussmayer, K. S., Steiner, F., Lupton, J. M., Herten, D.-P. & Vogelsang, J. Differentiation between Shallow and Deep Charge Trap States on Single Poly(3-hexylthiophene) Chains through Fluorescence Photon Statistics. *Chem. Phys. Chem.* **16**, 3578 (2015).

160 Tretiak, S., Saxena, A., Martin, R. L. & Bishop, A. R. Conformational dynamics of photoexcited conjugated molecules. *Phys. Rev. Lett.* **89**, 097402 (2002).

161 Thiessen, A., Würsch, D., Jester, S. S., Aggarwal, A. V., Idelson, A., Bange, S., Vogelsang, J., Höger, S. & Lupton, J. M. Exciton Localization in Extended pi-Electron Systems: Comparison of Linear and Cyclic Structures. *J. Phys. Chem. B* **119**, 9949 (2015).

162 Würsch, D., Hofmann, F. J., Eder, T., Aggarwal, A. V., Idelson, A., Höger, S., Lupton, J. M. & Vogelsang, J. Molecular Water Lilies: Orienting Single Molecules in a Polymer Film by Solvent Vapor Annealing. *J. Phys. Chem. Lett.* **7**, 4451 (2016).

163 Lupton, J. M. Chromophores in Conjugated Polymers-All Straight? *Chem. Phys. Chem.* **13**, 901 (2012).

164 Mannouch, J. R., Barford, W. & Al-Assam, S. Ultra-fast relaxation, decoherence, and localization of photoexcited states in pi-conjugated polymers. *J. Chem. Phys.* **148**, 034901 (2018).

165 Scholes, G. D. Long-range resonance energy transfer in molecular systems. *Annu. Rev. Phys. Chem.* **54**, 57 (2003).

166 Wilhelm, P., Vogelsang, J., Höger, S. & Lupton, J. M. Homo-FRET in pi-Conjugated Polygons: Intermediate-Strength Dipole-Dipole Coupling Makes Energy Transfer Reversible. *Nano Lett.* **19**, 5483 (2019).

167 Wilhelm, P., Schedlbauer, J., Hinderer, F., Hennen, D., Höger, S., Vogelsang, J. & Lupton, J. M. Molecular excitonic seesaws. *Proc. Natl. Acad. Sci. U. S. A.* **115**, E3626 (2018).

168 Deutsch, Z., Schwartz, O., Tenne, R., Popovitz-Biro, R. & Oron, D. Two-Color Antibunching from Band-Gap Engineered Colloidal Semiconductor Nanocrystals. *Nano Lett.* **12**, 2948 (2012).

169 Liu, S., Borys, N. J., Sapra, S., Eychmueller, A. & Lupton, J. M. Localization and Dynamics of Long-Lived Excitations in Colloidal Semiconductor Nanocrystals with Dual Quantum Confinement. *Chem. Phys. Chem.* **16**, 1663 (2015).

170 Talapin, D. V., Koeppe, R., Götzinger, S., Kornowski, A., Lupton, J. M., Rogach, A. L., Benson, O., Feldmann, J. & Weller, H. Highly emissive colloidal CdSe/CdS heterostructures of mixed dimensionality. *Nano Lett.* **3**, 1677 (2003).

171 Borys, N. J., Walter, M. J., Huang, J., Talapin, D. V. & Lupton, J. M. The Role of Particle Morphology in Interfacial Energy Transfer in CdSe/CdS Heterostructure Nanocrystals. *Science* **330**, 1371 (2010).

172 Manna, L., Milliron, D. J., Meisel, A., Scher, E. C. & Alivisatos, A. P. Controlled growth of tetrapod-branched inorganic nanocrystals. *Nat. Mater.* **2**, 382 (2003).

173 Klimov, V. I., Mikhailovsky, A. A., McBranch, D. W., Leatherdale, C. A. & Bawendi, M. G. Quantization of multiparticle Auger rates in semiconductor quantum dots. *Science* **287**, 1011 (2000).

174 Klimov, V. I., Mikhailovsky, A. A., Xu, S., Malko, A., Hollingsworth, J. A., Leatherdale, C. A., Eisler, H. J. & Bawendi, M. G. Optical gain and stimulated emission in nanocrystal quantum dots. *Science* **290**, 314 (2000).

175 Schaller, R. D., Agranovich, V. M. & Klimov, V. I. High-efficiency carrier multiplication through direct photogeneration of multi-excitons via virtual single-exciton states. *Nat. Phys.* **1**, 189 (2005).

176 Sambur, J. B., Novet, T. & Parkinson, B. A. Multiple Exciton Collection in a Sensitized Photovoltaic System. *Science* **330**, 63 (2010).

177 Semonin, O. E., Luther, J. M., Choi, S., Chen, H. Y., Gao, J. B., Nozik, A. J. & Beard, M. C. Peak External Photocurrent Quantum Efficiency Exceeding 100% via MEG in a Quantum Dot Solar Cell. *Science* **334**, 1530 (2011).

178 Kraus, R. M., Lagoudakis, P. G., Müller, J., Rogach, A. L., Lupton, J. M., Feldmann, J., Talapin, D. V. & Weller, H. Interplay between auger and ionization processes in nanocrystal quantum dots. *J. Phys. Chem. B* **109**, 18214 (2005).

179 Park, Y. S., Ghosh, Y., Chen, Y., Piryatinski, A., Xu, P., Mack, N. H., Wang, H. L., Klimov, V. I., Hollingsworth, J. A. & Htoon, H. Super-Poissonian Statistics of Photon Emission from Single CdSe-CdS Core-Shell Nanocrystals Coupled to Metal Nanostructures. *Phys. Rev. Lett.* **110**, 117401 (2013).

180 LeBlanc, S. J., McClanahan, M. R., Jones, M. & Moyer, P. J. Enhancement of Multiphoton Emission from Single CdSe Quantum Dots Coupled to Gold Films. *Nano Lett.* **13**, 1662 (2013).

181 Nair, G., Zhao, J. & Bawendi, M. G. Biexciton Quantum Yield of Single Semiconductor Nanocrystals from Photon Statistics. *Nano Lett.* **11**, 1136 (2011).

182 Park, Y. S., Guo, S. J., Makarov, N. S. & Klimov, V. I. Room Temperature Single-Photon Emission from Individual Perovskite Quantum Dots. *ACS Nano* **9**, 10386 (2015).

183 Utzat, H., Shulenberger, K. E., Achorn, O. B., Nasilowski, M., Sinclair, T. S. & Bawendi, M. G. Probing Linewidths and Biexciton Quantum Yields of Single Cesium Lead Halide Nanocrystals in Solution. *Nano Lett.* **17**, 6838 (2017).

184 Mangum, B. D., Ghosh, Y., Hollingsworth, J. A. & Htoon, H. Disentangling the effects of clustering and multi-exciton emission in second-order photon correlation experiments. *Opt. Express* **21**, 7419 (2013).

185 Benjamin, E., Yallapragada, V. J., Amgar, D., Yang, G. L., Tenne, R. & Oron, D. Temperature Dependence of Excitonic and Biexcitonic Decay Rates in Colloidal Nanoplatelets by Time-Gated Photon Correlation. *J. Phys. Chem. Lett.* **11**, 6513 (2020).

186 Feng, S. W., Cheng, C. Y., Wei, C. Y., Yang, J. H., Chen, Y. R., Chuang, Y. W., Fan, Y. H. & Chuu, C. S. Purification of Single Photons from Room-Temperature Quantum Dots. *Phys. Rev. Lett.* **119**, 143601 (2017).

187 Hofmann, F. J., Bodnarchuk, M. I., Protesescu, L., Koyalenko, M. V., Lupton, J. M. & Vogelsang, J. Exciton Gating and Triplet Deshelving in Single Dye Molecules Excited by Perovskite Nanocrystal FRET Antennae. *J. Phys. Chem. Lett.* **10**, 1055 (2019).

188 Hofmann, F. J., Bodnarchuk, M. I., Dirin, D. N., Vogelsang, J., Kovalenko, M. V. & Lupton, J. M. Energy Transfer from Perovskite Nanocrystals to Dye Molecules Does Not Occur by FRET. *Nano Lett.* **19**, 8896 (2019).

189 English, D. S., Harbron, E. J. & Barbara, P. F. Probing photoinduced intersystem crossing by two-color, double resonance single molecule spectroscopy. *J. Phys. Chem. A* **104**, 9057 (2000).

190 Becker, K., Lupton, J. M., Müller, J., Rogach, A. L., Talapin, D. V., Weller, H. & Feldmann, J. Electrical control of Förster energy transfer. *Nat. Mater.* **5**, 777 (2006).

191 Soujon, D., Becker, K., Rogach, A. L., Feldmann, J., Weller, H., Talapin, D. V. & Lupton, J. M. Time-resolved Forster energy transfer from individual semiconductor nanoantennae to single dye molecules. *J. Phys. Chem. C* **111**, 11511 (2007).

192 Becker, M. A., Vaxenburg, R., Nedelcu, G., Sercel, P. C., Shabaev, A., Mehl, M. J., Michopoulos, J. G., Lambrakos, S. G., Bernstein, N., Lyons, J. L., Stoferle, T., Mahrt, R. F., Kovalenko, M. V., Norris, D. J., Raino, G. & Efros, A. L. Bright triplet excitons in caesium lead halide perovskites. *Nature* **553**, 189 (2018).

193 Tamarat, P., Hou, L., Trebbia, J. B., Swarnkar, A., Biadala, L., Louyer, Y., Bodnarchuk, M. I., Kovalenko, M. V., Even, J. & Lounis, B. The dark exciton ground state promotes photon-pair emission in individual perovskite nanocrystals. *Nat. Commun.* **11**, 6001 (2020).

194 Novoselov, K. S., Jiang, D., Schedin, F., Booth, T. J., Khotkevich, V. V., Morozov, S. V. & Geim, A. K. Two-dimensional atomic crystals. *Proc. Natl. Acad. Sci. U. S. A.* **102**, 10451 (2005).

195 He, Y. M., Clark, G., Schaibley, J. R., He, Y., Chen, M. C., Wei, Y. J., Ding, X., Zhang, Q., Yao, W., Xu, X. D., Lu, C. Y. & Pan, J. W. Single quantum emitters in monolayer semiconductors. *Nat. Nano.* **10**, 497 (2015).

196 Toth, M. & Aharonovich, I. Single Photon Sources in Atomically Thin Materials. *Annu. Rev. Phys. Chem.* **70**, 123 (2019).

197 Koperski, M., Nogajewski, K., Arora, A., Cherkez, V., Mallet, P., Veuillen, J. Y., Marcus, J., Kossacki, P. & Potemski, M. Single photon emitters in exfoliated WSe2 structures. *Nat. Nano.* **10**, 503 (2015).

198 Srivastava, A., Sidler, M., Allain, A. V., Lembke, D. S., Kis, A. & Imamoglu, A. Optically active quantum dots in monolayer WSe2. *Nat. Nano.* **10**, 491 (2015).

199 Tonndorf, P., Schmidt, R., Schneider, R., Kern, J., Buscema, M., Steele, G. A., Castellanos-Gomez, A., van der Zant, H. S. J., de Vasconcellos, S. M. & Bratschitsch, R. Single-photon emission from localized excitons in an atomically thin semiconductor. *Optica* **2**, 347 (2015).

200 He, Y. M., Iff, O., Lundt, N., Baumann, V., Davanco, M., Srinivasan, K., Höfling, S. & Schneider, C. Cascaded emission of single photons from the biexciton in monolayered WSe2. *Nat. Commun.* **7**, 13409 (2016).

201 Berndt, R., Schlittler, R. R. & Gimzewski, J. K. Photon-emission scanning tunneling microscope. *J. Vac. Sci. Tech. B* **9**, 573 (1991).

202 Lambe, J. & McCarthy, S. L. Light-emission from inelastic electron-tunneling. *Phys. Rev. Lett.* **37**, 923 (1976).

203 Kern, J., Kullock, R., Prangsma, J., Emmerling, M., Kamp, M. & Hecht, B. Electrically driven optical antennas. *Nat. Photon.* **9**, 582 (2015).

204 Schneider, N. L., Lu, J. T., Brandbyge, M. & Berndt, R. Light Emission Probing Quantum Shot Noise and Charge Fluctuations at a Biased Molecular Junction. *Phys. Rev. Lett.* **109**, 186601 (2012).

205 Silly, F. & Charra, F. Time-autocorrelation in scanning-tunneling-microscope-induced photon emission from metallic surface. *Appl. Phys. Lett.* **77**, 3648 (2000).

206 Leon, C. C., Roslawska, A., Grewal, A., Gunnarsson, O., Kuhnke, K. & Kern, K. Photon superbunching from a generic tunnel junction. *Sci. Adv.* **5**, eaav4986 (2019).

207 Merino, P., Grosse, C., Roslawska, A., Kuhnke, K. & Kern, K. Exciton dynamics of C-60-based single-photon emitters explored by Hanbury Brown-Twiss scanning tunnelling microscopy. *Nat. Commun.* **6**, 8461 (2015).

208 Zhang, L., Yu, Y. J., Chen, L. G., Luo, Y., Yang, B., Kong, F. F., Chen, G., Zhang, Y., Zhang, Q., Luo, Y., Yang, J. L., Dong, Z. C. & Hou, J. G. Electrically driven single-photon emission from an isolated single molecule. *Nat. Commun.* **8**, 580 (2017).

209 Gonzalez, J. I., Lee, T. H., Barnes, M. D., Antoku, Y. & Dickson, R. M. Quantum mechanical single-gold-nanocluster electroluminescent light source at room temperature. *Phys. Rev. Lett.* **93** (2004).

210 Gonzalez, J. I., Vosch, T. & Dickson, R. M. Asymmetric electrode-molecule transport dynamics tracked by nanoscale electroluminescence. *Phys. Rev. B* **74**, 064305 (2006).

211 Wientjes, E., Renger, J., Curto, A. G., Cogdell, R. & van Hulst, N. F. Strong antenna-enhanced fluorescence of a single light-harvesting complex shows photon antibunching. *Nat. Commun.* **5**, 4236 (2014).

212 Aharonovich, I., Englund, D. & Toth, M. Solid-state single-photon emitters. *Nat. Photon.* **10**, 631 (2016).

213 Ma, X. D., Roslyak, O., Duque, J. G., Pang, X. Y., Doorn, S. K., Piryatinski, A., Dunlap, D. H. & Htoon, H. Influences of Exciton Diffusion and Exciton-Exciton Annihilation on Photon Emission Statistics of Carbon Nanotubes. *Phys. Rev. Lett.* **115**, 017401 (2015).

214 Ishii, A., He, X. W., Hartmann, N. F., Machiya, H., Htoon, H., Doorn, S. K. & Kato, Y. K. Enhanced Single-Photon Emission from Carbon-Nanotube Dopant States Coupled to Silicon Microcavities. *Nano Lett.* **18**, 3873 (2018).

215 He, X. W., Hartmann, N. F., Ma, X. D., Kim, Y., Ihly, R., Blackburn, J. L., Gao, W. L., Kono, J., Yomogida, Y., Hirano, A., Tanaka, T., Kataura, H., Htoon, H. & Doorn, S. K. Tunable room-temperature single-photon emission at telecom wavelengths from sp(3) defects in carbon nanotubes. *Nat. Photon.* **11**, 577 (2017).

216 Hayee, F., Yu, L., Zhang, J. L., Ciccarino, C. J., Nguyen, M., Marshall, A. F., Aharonovich, I., Vuckovic, J., Narang, P., Heinz, T. F. & Dionne, J. A. Revealing multiple classes of stable quantum emitters in hexagonal boron nitride with correlated optical and electron microscopy. *Nat. Mater.* **19**, 534 (2020).

217 Grosso, G., Moon, H., Lienhard, B., Ali, S., Efetov, D. K., Furchi, M. M., Jarillo-Herrero, P., Ford, M. J., Aharonovich, I. & Englund, D. Tunable and high-purity room temperature single-photon emission from atomic defects in hexagonal boron nitride. *Nat. Commun.* **8**, 705 (2017).

218 Castelletto, S., Johnson, B. C., Ivady, V., Stavrias, N., Umeda, T., Gali, A. & Ohshima, T. A silicon carbide room-temperature single-photon source. *Nat. Mater.* **13**, 151 (2014).

219 Mendelson, N., Chugh, D., Reimers, J. R., Cheng, T. S., Gottscholl, A., Long, H., Mellor, C. J., Zettl, A., Dyakonov, V., Beton, P. H., Novikov, S. V., Jagadish, C., Tan, H. H., Ford, M. J., Toth, M., Bradac, C. & Aharonovich, I. Identifying carbon as the source of visible single-photon emission from hexagonal boron nitride. *Nat. Mater.* **20**, 321 (2021).

220 Krishnamurthy, S., Singh, A., Hu, Z. J., Blake, A. V., Kim, Y., Singh, A., Dolgopolova, E. A., Williams, D. J., Piryatinski, A., Malko, A. V., Htoon, H., Sykora, M. & Hollingsworth, J. A. PbS/CdS Quantum Dot Room-Temperature Single-Emitter Spectroscopy Reaches the Telecom O and S Bands via an Engineered Stability. *ACS Nano* **15**, 575 (2021).

221 Chandrasekaran, V., Tessier, M. D., Dupont, D., Geiregat, P., Hens, Z. & Brainis, E. Nearly Blinking-Free, High-Purity Single-Photon Emission by Colloidal InP/ZnSe Quantum Dots. *Nano Lett.* **17**, 6104 (2017).

222 Liu, X., Akahane, K., Jahan, N. A., Kobayashi, N., Sasaki, M., Kumano, H. & Suemune, I. Single-photon emission in telecommunication band from an InAs quantum dot grown on InP with molecular-beam epitaxy. *Appl. Phys. Lett.* **103**, 061114 (2013).

223 Dusanowski, L., Syperek, M., Misiewicz, J., Somers, A., Hofling, S., Kamp, M., Reithmaier, J. P. & Sek, G. Single-photon emission of InAs/InP quantum dashes at 1.55 mu m and temperatures up to 80K. *Appl. Phys. Lett.* **108**, 163108 (2016).

224 Zinoni, C., Alloing, B., Monat, C., Zwiller, V., Li, L. H., Fiore, A., Lunghi, L., Gerardino, A., de Riedmatten, H., Zbinden, H. & Gisin, N. Time-resolved and antibunching experiments on single quantum dots at 1300 nm. *Appl. Phys. Lett.* **88**, 131102 (2006).

225 Lv, B. H., Zhang, H. C., Wang, L. P., Zhang, C. F., Wang, X. Y., Zhang, J. Y. & Xiao, M. Photon antibunching in a cluster of giant CdSe/CdS nanocrystals. *Nat. Commun.* **9**, 1536 (2018).

226 Stangl, T., Wilhelm, P., Remmerssen, K., Höger, S., Vogelsang, J. & Lupton, J. M. Mesoscopic quantum emitters from deterministic aggregates of conjugated polymers. *Proc. Natl. Acad. Sci. U. S. A.* **112**, E5560 (2015).

227 Tizei, L. H. G. & Kociak, M. Spatially Resolved Quantum Nano-Optics of Single Photons Using an Electron Microscope. *Phys. Rev. Lett.* **110**, 153604 (2013).

228 Press, D., Götzinger, S., Reitzenstein, S., Hofmann, C., Loffler, A., Kamp, M., Forchel, A. & Yamamoto, Y. Photon antibunching from a single quantum-dot-microcavity system in the strong coupling regime. *Phys. Rev. Lett.* **98**, 117402 (2007).

229 Hsiao, T. K., Rubino, A., Chung, Y. S., Son, S. K., Hou, H. T., Pedros, J., Nasir, A., Ethier-Majcher, G., Stanley, M. J., Phillips, R. T., Mitchell, T. A., Griffiths, J. P., Farrer, I., Ritchie, D. A. & Ford, C. J. B. Single-photon emission from single-electron transport in a SAW-driven lateral light-emitting diode. *Nat. Commun.* **11**, 917 (2020).

230 Villa, B., Bennett, A. J., Ellis, D. J. P., Lee, J. P., Skiba-Szymanska, J., Mitchell, T. A., Griffiths, J. P., Farrer, I., Ritchie, D. A., Ford, C. J. B. & Shields, A. J. Surface acoustic wave modulation of a coherently driven quantum dot in a pillar microcavity. *Appl. Phys. Lett.* **111**, 011103 (2017).

231 Velez, S. T., Seibold, K., Kipfer, N., Anderson, M. D., Sudhir, V. & Galland, C. Preparation and Decay of a Single Quantum of Vibration at Ambient Conditions. *Phys. Rev. X* **9**, 041007 (2019).

232 Akimov, A. V., Mukherjee, A., Yu, C. L., Chang, D. E., Zibrov, A. S., Hemmer, P. R., Park, H. & Lukin, M. D. Generation of single optical plasmons in metallic nanowires coupled to quantum dots. *Nature* **450**, 402 (2007).

233 Rolland, C., Peugeot, A., Dambach, S., Westig, M., Kubala, B., Mukharsky, Y., Altimiras, C., le Sueur, H., Joyez, R., Vion, D., Roche, P., Esteve, D., Ankerhold, J. & Portier, F. Antibunched Photons Emitted by a dc-Biased Josephson Junction. *Phys. Rev. Lett.* **122**, 186804 (2019).

234 Lupton, J. M., Matterson, B. J., Samuel, I. D. W., Jory, M. J. & Barnes, W. L. Bragg scattering from periodically microstructured light emitting diodes. *Appl. Phys. Lett.* **77**, 3340 (2000).

235 Meerholz, K. & Müller, D. C. Outsmarting waveguide losses in thin-film light-emitting diodes. *Adv. Funct. Mat.* **11**, 251 (2001).

236 Kim, K. H., Lee, S., Moon, C. K., Kim, S. Y., Park, Y. S., Lee, J. H., Lee, J. W., Huh, J., You, Y. & Kim, J. J. Phosphorescent dye-based supramolecules for high-efficiency organic light-emitting diodes. *Nat. Commun.* **5**, 4769 (2014).

237 Jurow, M. J., Mayr, C., Schmidt, T. D., Lampe, T., Djurovich, P. I., Brütting, W. & Thompson, M. E. Understanding and predicting the orientation of heteroleptic phosphors in organic light-emitting materials. *Nat. Mater.* **15**, 85 (2016).

238 Haneder, S., Da Como, E., Feldmann, J., Lupton, J. M., Lennartz, C., Erk, P., Fuchs, E., Molt, O., Munster, I., Schildknecht, C. & Wagenblast, G. Controlling the radiative rate

of deep-blue electrophosphorescent organometallic complexes by singlet-triplet gap engineering. *Adv. Mater.* **20**, 3325 (2008).

239 Koide, Y., Takahashi, S. & Vacha, M. Simultaneous two-photon excited fluorescence and one-photon excited phosphorescence from single molecules of an organometallic complex Ir(ppy)(3). *J. Am. Chem. Soc.* **128**, 10990 (2006).

240 Graf, A., Liehm, P., Murawski, C., Hofmann, S., Leo, K. & Gather, M. C. Correlating the transition dipole moment orientation of phosphorescent emitter molecules in OLEDs with basic material properties. *J. Mat. Chem. C* **2**, 10298 (2014).

241 Steiner, F., Bange, S., Vogelsang, J. & Lupton, J. M. Spontaneous Fluctuations of Transition Dipole Moment Orientation in OLED Triplet Emitters. *J. Phys. Chem. Lett.* **6**, 999 (2015).

242 Hu, D. H. & Lu, H. P. Single-molecule triplet-state photon antibunching at room temperature. *J. Phys. Chem. B* **109**, 9861 (2005).

243 Grell, M., Bradley, D. D. C., Ungar, G., Hill, J. & Whitehead, K. S. Interplay of physical structure and photophysics for a liquid crystalline polyfluorene. *Macromolecules* **32**, 5810 (1999).

244 Becker, K. & Lupton, J. M. Dual species emission from single polyfluorene molecules: Signatures of stress-induced planarization of single polymer chains. *J. Am. Chem. Soc.* **127**, 7306 (2005).

245 Wilhelm, P., Blank, D., Lupton, J. M. & Vogelsang, J. Control of Intrachain Morphology in the Formation of Polyfluorene Aggregates on the Single-Molecule Level. *Chem. Phys. Chem.* **21**, 961 (2020).

246 Masuo, S., Tanaka, T., Machida, S. & Itaya, A. Influence of molecular weight and conformation on single-photon emission from isolated conjugated polymer chains. *Appl. Phys. Lett.* **92**, 233114 (2008).

247 Kumar, P., Lee, T. H., Mehta, A., Sumpter, B. G., Dickson, R. M. & Barnes, M. D. Photon antibunching from oriented semiconducting polymer nanostructures. *J. Am. Chem. Soc.* **126**, 3376 (2004).

248 Da Como, E., Borys, N. J., Strohriegl, P., Walter, M. J. & Lupton, J. M. Formation of a Defect-Free pi-Electron System in Single beta-Phase Polyfluorene Chains. *J. Am. Chem. Soc.* **133**, 3690 (2011).

249 Da Como, E., Becker, K., Feldmann, J. & Lupton, J. M. How strain controls electronic linewidth in single beta-phase polyfluorene nanowires. *Nano Lett.* **7**, 2993 (2007).

250 Adachi, T., Vogelsang, J. & Lupton, J. M. Chromophore Bending Controls Fluorescence Lifetime in Single Conjugated Polymer Chains. *J. Phys. Chem. Lett.* **5**, 2165 (2014).

251 Palo, K., Metz, U., Jäger, S., Kask, P. & Gall, K. Fluorescence intensity multiple distributions analysis: Concurrent determination of diffusion times and molecular brightness. *Biophys. J.* **79**, 2858 (2000).

252 Murthy, A. V. R., Goel, M., Patil, S. & Jayakannan, M. Probing the Role of Chain Length on the Diffusion Dynamics of pi-Conjugated Polymers by Fluorescence Correlation Spectroscopy. *J. Phys. Chem. B* **115**, 10779 (2011).

253 Masuo, S., Nishi, N., Hosugi, M., Machida, S. & Itaya, A. Dependence of Single-photon Emission from Single Conjugated Polymer Chains on Their Spatial Size as Determined by Photon-correlation Measurements in Fluid Solution. *Chem. Lett.* **39**, 780 (2010).

254 Lin, H. Z., Tian, Y. X., Zapadka, K., Persson, G., Thomsson, D., Mirzov, O., Larsson, P. O., Widengren, J. & Scheblykin, I. G. Fate of Excitations in Conjugated Polymers: Single-Molecule Spectroscopy Reveals Nonemissive "Dark" Regions in MEH-PPV Individual Chains. *Nano Lett.* **9**, 4456 (2009).

255 Wu, E. C., Stubbs, R. E., Peteanu, L. K., Jemison, R., McCullough, R. D. & Wildeman, J. Detection of Ultralow Concentrations of Non-emissive Conjugated Polymer Aggregates via Fluorescence Correlation Spectroscopy. *J. Phys. Chem. B* **121**, 5413 (2017).

256 Bässler, H. & Schweitzer, B. Site-selective fluorescence spectroscopy of conjugated polymers and oligomers. *Acc. Chem. Res.* **32**, 173 (1999).

257 Müller, J. G., Anni, M., Scherf, U., Lupton, J. M. & Feldmann, J. Vibrational fluorescence spectroscopy of single conjugated polymer molecules. *Phys. Rev. B* **70**, 035205 (2004).

258 Müller, J. G., Lemmer, U., Raschke, G., Anni, M., Scherf, U., Lupton, J. M. & Feldmann, J. Linewidth-limited energy transfer in single conjugated polymer molecules. *Phys. Rev. Lett.* **91**, 267403 (2003).

259 Müller, J. G., Lupton, J. M., Feldmann, J., Lemmer, U. & Scherf, U. Ultrafast intramolecular energy transfer in single conjugated polymer chains probed by polarized single chromophore spectroscopy. *Appl. Phys. Lett.* **84**, 1183 (2004).

260 Schindler, F., Lupton, J. M., Feldmann, J. & Scherf, U. A universal picture of chromophores in pi-conjugated polymers derived from single-molecule spectroscopy. *Proc. Natl. Acad. Sci. U. S. A.* **101**, 14695 (2004).

261 Hofmann, F. J., Vogelsang, J. & Lupton, J. M. Impact of charge carrier injection on single-chain photophysics of conjugated polymers. *Appl. Phys. Lett.* **108**, 263301 (2016).

262 Moskovits, M. Surface-enhanced Raman spectroscopy: a brief retrospective. *J. Raman Spectrosc.* **36**, 485 (2005).

263 Peyser-Capadona, L., Zheng, J., Gonzalez, J. I., Lee, T. H., Patel, S. A. & Dickson, R. M. Nanoparticle-free single molecule anti-stokes Raman spectroscopy. *Phys. Rev. Lett.* **94**, 058301 (2005).

264 Walter, M. J., Lupton, J. M., Becker, K., Feldmann, J., Gaefke, G. & Höger, S. Simultaneous Raman and fluorescence spectroscopy of single conjugated polymer chains. *Phys. Rev. Lett.* **98**, 137401 (2007).

265 Dang, M. T., Hirsch, L. & Wantz, G. P3HT:PCBM, Best Seller in Polymer Photovoltaic Research. *Adv. Mater.* **23**, 3597 (2011).

266 Thiessen, A., Vogelsang, J., Adachi, T., Steiner, F., Vanden Bout, D. & Lupton, J. M. Unraveling the chromophoric disorder of poly(3-hexylthiophene). *Proc. Natl. Acad. Sci. U. S. A.* **110**, E3550 (2013).

267 Steiner, F., Vogelsang, J. & Lupton, J. M. Singlet-Triplet Annihilation Limits Exciton Yield in Poly(3-Hexylthiophene). *Phys. Rev. Lett.* **112**, 137402 (2014).

268 Vogelsang, J., Adachi, T., Brazard, J., Bout, D. A. V. & Barbara, P. F. Self-assembly of highly ordered conjugated polymer aggregates with long-range energy transfer. *Nat. Mater.* **10**, 942 (2011).

269 Vogelsang, J. & Lupton, J. M. Solvent Vapor Annealing of Single Conjugated Polymer Chains: Building Organic Optoelectronic Materials from the Bottom Up. *J. Phys. Chem. Lett.* **3**, 1503 (2012).

270 Thomas, A. K., Brown, H. A., Datko, B. D., Garcia-Galvez, J. A. & Grey, J. K. Interchain Charge-Transfer States Mediate Triplet Formation in Purified Conjugated Polymer Aggregates. *J. Phys. Chem. C* **120**, 23230 (2016).

271 Thomas, A. K., Garcia, J. A., Ulibarri-Sanchez, J., Gao, J. & Grey, J. K. High Intrachain Order Promotes Triplet Formation from Recombination of Long-Lived Polarons in Poly(3-hexylthiophene) J-Aggregate Nanofibers. *ACS Nano* **8**, 10559 (2014).

272 Liang, Y., Xu, Z., Xia, J., Tsai, S.-T., Wu, Y., Li, G., Ray, C. & Yu, L. For the Bright Future-Bulk Heterojunction Polymer Solar Cells with Power Conversion Efficiency of 7.4%. *Adv. Mater.* **22**, 135 (2010).

273 Hedley, G. J., Steiner, F., Vogelsang, J. & Lupton, J. M. Determining the True Optical Gap in a High-Performance Organic Photovoltaic Polymer Using Single-Molecule Spectroscopy. *J. Phys. Chem. Lett.* **8**, 3494 (2017).

274 Hedley, G. J., Steiner, F., Vogelsang, J. & Lupton, J. M. Fluctuations in the Emission Polarization and Spectrum in Single Chains of a Common Conjugated Polymer for Organic Photovoltaics. *Small* **14**, 1804312 (2018).

275 Spano, F. C. & Silva, C. H- and J-Aggregate Behavior in Polymeric Semiconductors. *Annu. Rev. Phys. Chem.* **65**, 477 (2014).

276 Allolio, C., Stangl, T., Eder, T., Schmitz, D., Vogelsang, J., Höger, S., Horinek, D. & Lupton, J. M. H-Aggregation Effects between pi-Conjugated Chromophores in Cofacial Dinners and Trimers: Comparison of Theory and Single-Molecule Experiment. *J. Phys. Chem. B* **122**, 6431 (2018).

277 Stangl, T., Wilhelm, P., Schmitz, D., Remmerssen, K., Henzel, S., Jester, S. S., Höger, S., Vogelsang, J. & Lupton, J. M. Temporal Fluctuations in Excimer-Like Interactions between pi-Conjugated Chromophores. *J. Phys. Chem. Lett.* **6**, 1321 (2015).

278 Eder, T., Vogelsang, J., Bange, S., Remmerssen, K., Schmitz, D., Jester, S. S., Keller, T. J., Höger, S. & Lupton, J. M. Interplay Between J- and H-Type Coupling in Aggregates of pi-Conjugated Polymers: A Single-Molecule Perspective. *Angew. Chem. Int. Ed.* **58**, 18898 (2019).

279 Eder, T., Stangl, T., Gmelch, M., Remmerssen, K., Laux, D., Höger, S., Lupton, J. M. & Vogelsang, J. Switching between H- and J-type electronic coupling in single conjugated polymer aggregates. *Nat. Commun.* **8**, 1641 (2017).

280 Zondervan, R., Kulzer, F., Orlinskii, S. B. & Orrit, M. Photoblinking of rhodamine 6G in poly(vinyl alcohol): Radical dark state formed through the triplet. *J. Phys. Chem. A* **107**, 6770 (2003).

281 Tempelaar, R., Jansen, T. L. C. & Knoester, J. Exciton-Exciton Annihilation Is Coherently Suppressed in H-Aggregates, but Not in J-Aggregates. *J. Phys. Chem. Lett.* **8**, 6113 (2017).

282 Chaudhuri, D., Li, D., Che, Y., Shafran, E., Gerton, J. M., Zang, L. & Lupton, J. M. Enhancing Long-Range Exciton Guiding in Molecular Nanowires by H-Aggregation Lifetime Engineering. *Nano Lett.* **11**, 488 (2011).

283 Camacho, R., Taeuber, D. & Scheblykin, I. C. Fluorescence Anisotropy Reloaded-Emerging Polarization Microscopy Methods for Assessing Chromophores'

Organization and Excitation Energy Transfer in Single Molecules, Particles, Films, and Beyond. *Adv. Mater.* **31**, 1805671 (2019).

284 Nie, S. M., Chiu, D. T. & Zare, R. N. Probing individual molecules with confocal fluorescence microscopy. *Science* **266**, 1018 (1994).

285 Yang, H. & Xie, X. S. Probing single-molecule dynamics photon by photon. *J. Chem. Phys.* **117**, 10965 (2002).

286 Yang, H., Luo, G. B., Karnchanaphanurach, P., Louie, T. M., Rech, I., Cova, S., Xun, L. Y. & Xie, X. S. Protein conformational dynamics probed by single-molecule electron transfer. *Science* **302**, 262 (2003).

Figures and Captions

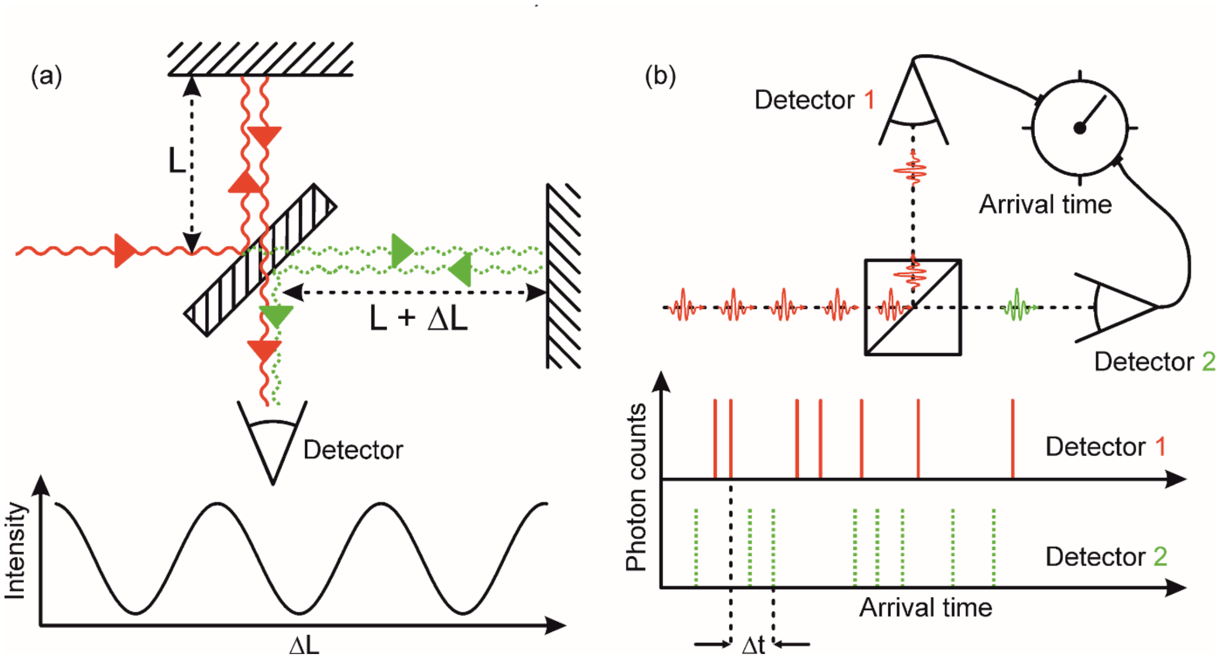

FIG. 1. Measuring correlations in the electric field amplitude and intensity of light. (a) Michelson interferometer for detecting the wave nature of light. Below, the expected intensity modulation is plotted due to constructive and destructive interference between the red and green (dotted) light paths. (b) Hanbury Brown and Twiss (HBT) setup for detecting the particle nature of light. Below, the arrival times of single photons detected on the two detectors are plotted. The arrival time differences, Δt, between two photons on different detectors is recorded to analyze the photon stream.

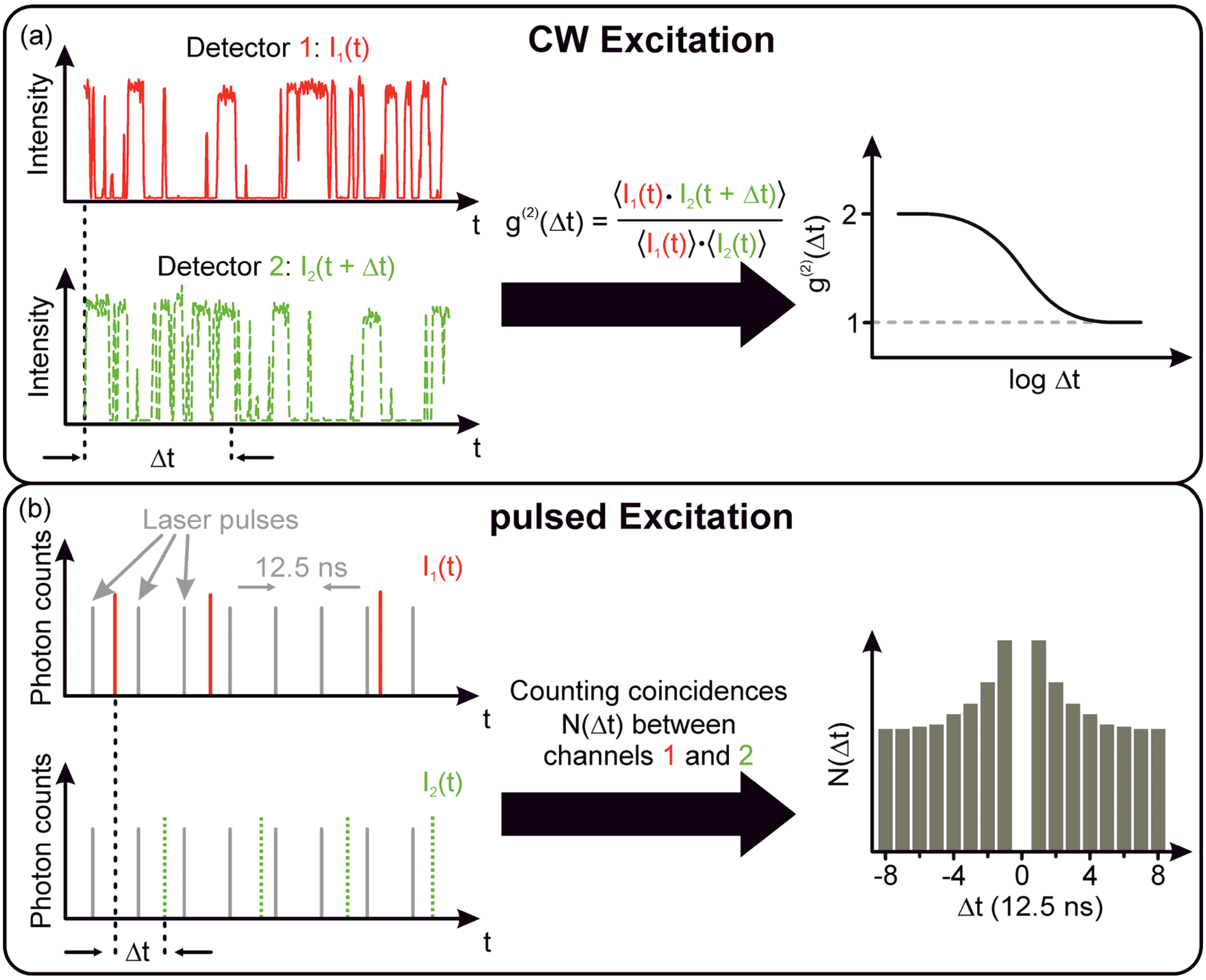

FIG. 2. Intensity correlation analysis under continuous-wave (CW) and pulsed excitation. (a) A second-order intensity cross-correlation, $g^{(2)}(\Delta t)$, is performed under CW excitation between two detection channels. (b) The coincidences, $N(\Delta t)$, are counted under pulsed excitation to detect two photons simultaneously for different time lags, Δt, on both detection channels. Δt is binned in multiples of the repetition rate of the laser (12.5 ns here), because often only a single photon can be detected per excitation pulse and detection channel. Both methods are similar and differ only in the normalization of the correlation function. $g^{(2)}(\Delta t)$ is usually used to analyze dynamics on time scales greater than 1 µs, whereas the coincidence histogram $N(\Delta t)$ is often employed for nanosecond time scales under pulsed excitation.

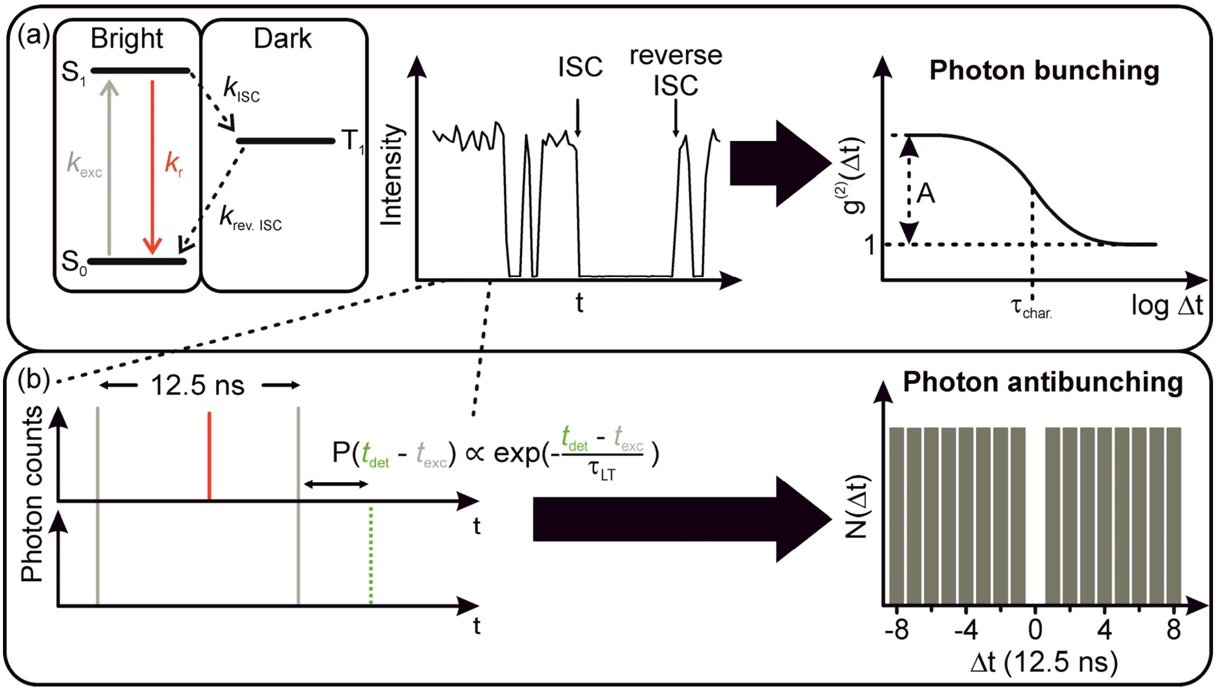

FIG. 3. Processes responsible for photon bunching and photon antibunching. (a) Simplified Jablonski diagram of a single chromophore. The chromophore emits light, i.e. it is in a bright state, if it resides in the singlet manifold, S_0 and S_1, and it is dark, if it transitions by intersystem crossing (ISC) into the triplet manifold. Depending on the triplet-state lifetime, the chromophore can be dark for several microseconds up to milliseconds, which results in bunching of the emitted photons and the typical blinking observed in the PL intensity transients. Such blinking can be analyzed by $g^{(2)}(\Delta t)$, from which the amplitude, A, and the characteristic timescale of the blinking, τ_{char}, can be extracted. (b) A single chromophore can only emit one single photon per excitation pulse if the excitation pulse is orders of magnitude shorter than the excited-state lifetime, τ_{LT}. For this reason, zero coincidences are expected for a time delay of zero between both channels, i.e. $N(0) = 0$, an effect which is referred to as photon antibunching.

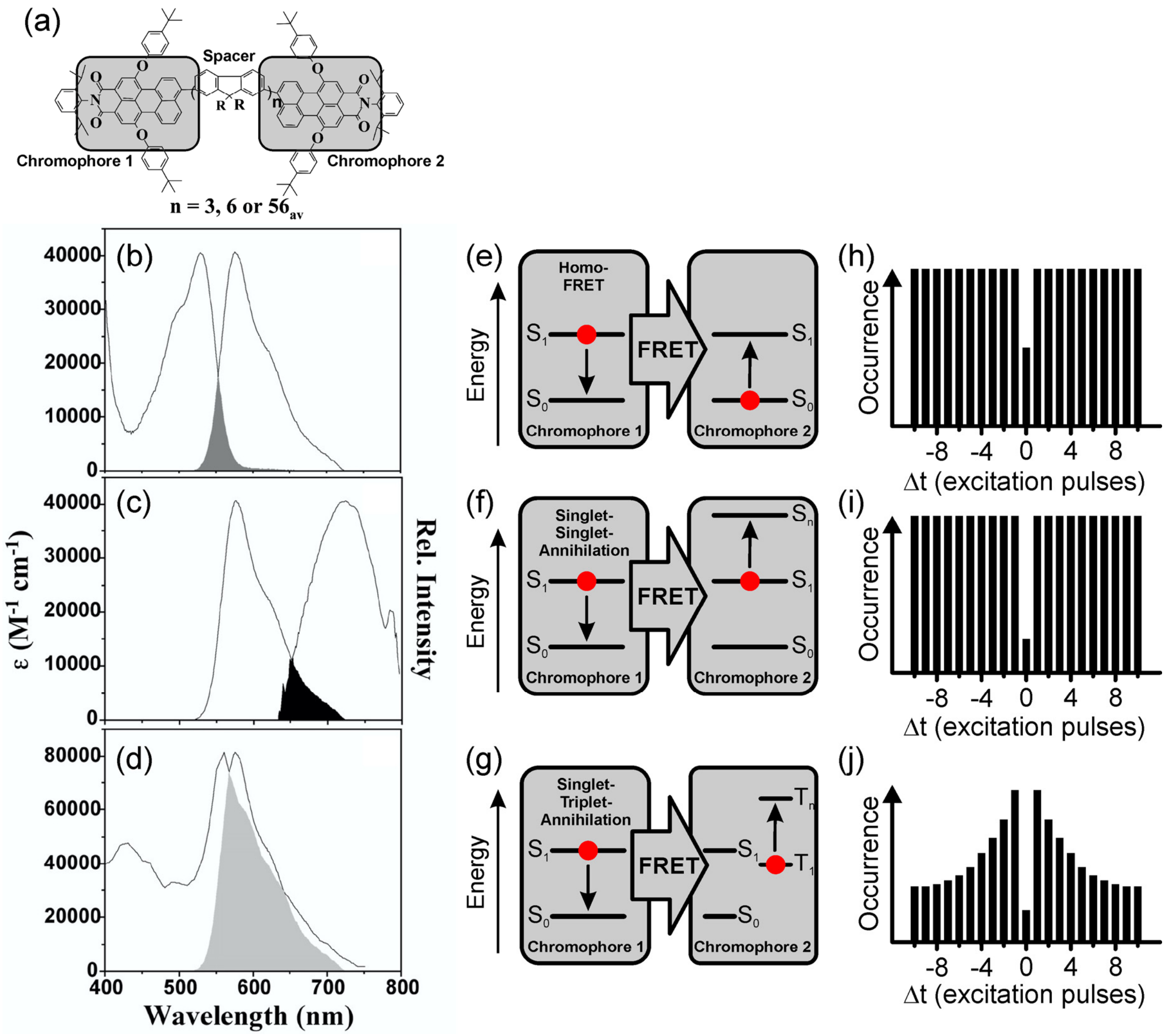

FIG. 4. Interaction processes between chromophores and their influence on photon statistics. (a) Chemical structure of a bichromophoric molecule with a variable spacer between the chromophores. (b) S_0 absorption and fluorescence spectrum of the chromophores shown in (a). (c) Fluorescence spectrum and S_1 absorption spectrum. (d) Fluorescence spectrum and T_1 absorption spectrum. The shaded areas represent the respective spectral overlaps between emission and absorption, which give rise to either homo-FRET (b), singlet-singlet annihilation [SSA, panel (c)] and singlet-triplet annihilation [STA, panel (d)] between both chromophores as depicted in panels (e)-(f). Panels (h)-(j) illustrate the expected photon coincidence histograms, $N(\Delta t)$, for all cases. Reproduced with permission from Proc. Natl. Acad. Sci. U. S. A. 100, 13146 (2003). Copyright (2003) National Academy of Sciences.

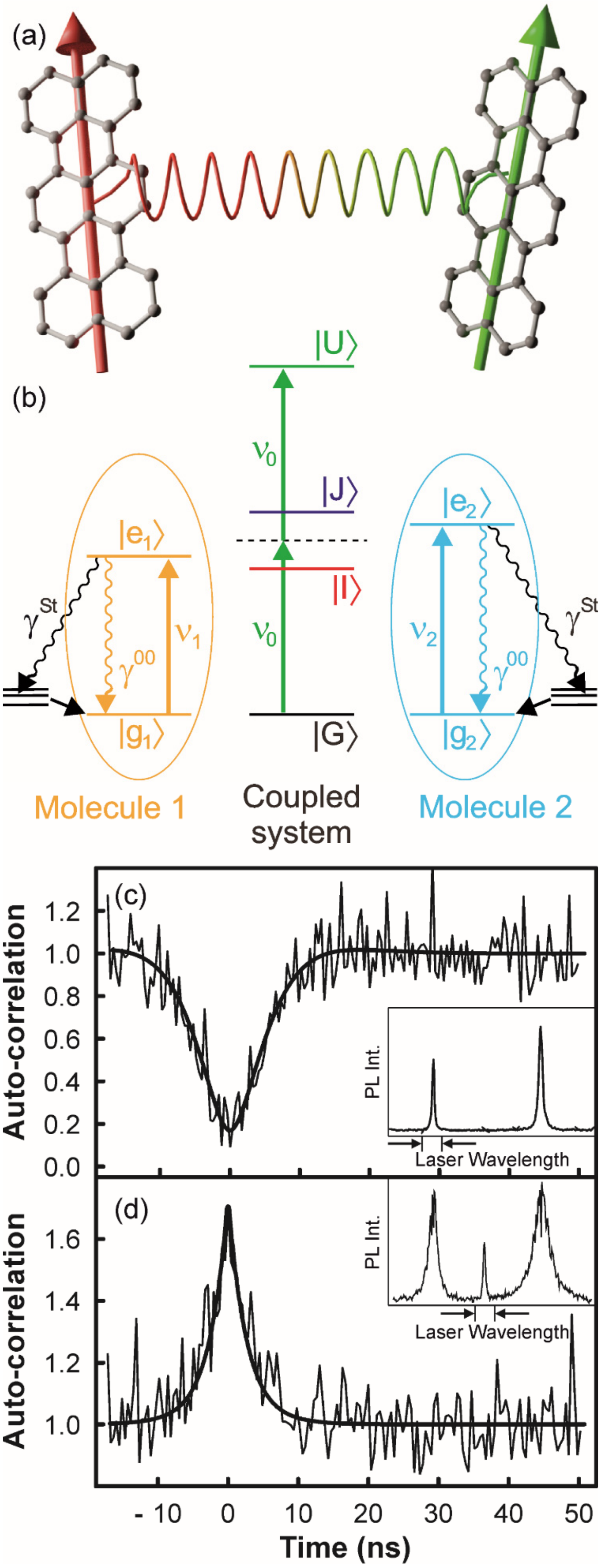

FIG. 5. Emergence of superradiance and photon bunching from dipole-dipole coupled molecules. (a) Schematic of two terrylene chromophores, coupled electronically by dipolar

interactions. The transition dipoles are represented by the red and green arrows, respectively. (b) Energy diagram of two coupled molecules with ground states $|g_1\rangle$ and $|g_2\rangle$ and excited states $|e_1\rangle$ and $|e_2\rangle$. The coupled system is given in the center with green transitions marked. The excited state can decay with rates γ^{00} and γ^{St}, in the latter case resulting in a Stokes shift and generating molecular vibrations. Because the transitions to the vibrational levels are followed by fast decay to the ground state, they do not contribute to the coherent coupling between the molecules. (c, d) $g^{(2)}(\Delta t)$ is plotted and photon antibunching is observed by scanning the laser wavelength over the lower resonance (c), i.e. over non-coupled chromophores. In contrast, photon bunching is observed by scanning over the central absorption peak (d), i.e. over coupled-chromophore transition. In each case, the PL excitation spectra corresponding to the system under study along with the frequency region of the spectrum contributing to the photon correlation measurement are shown in the inset. Reproduced with permission from Science 298, 385 (2002). Copyright 2002 AAAS.

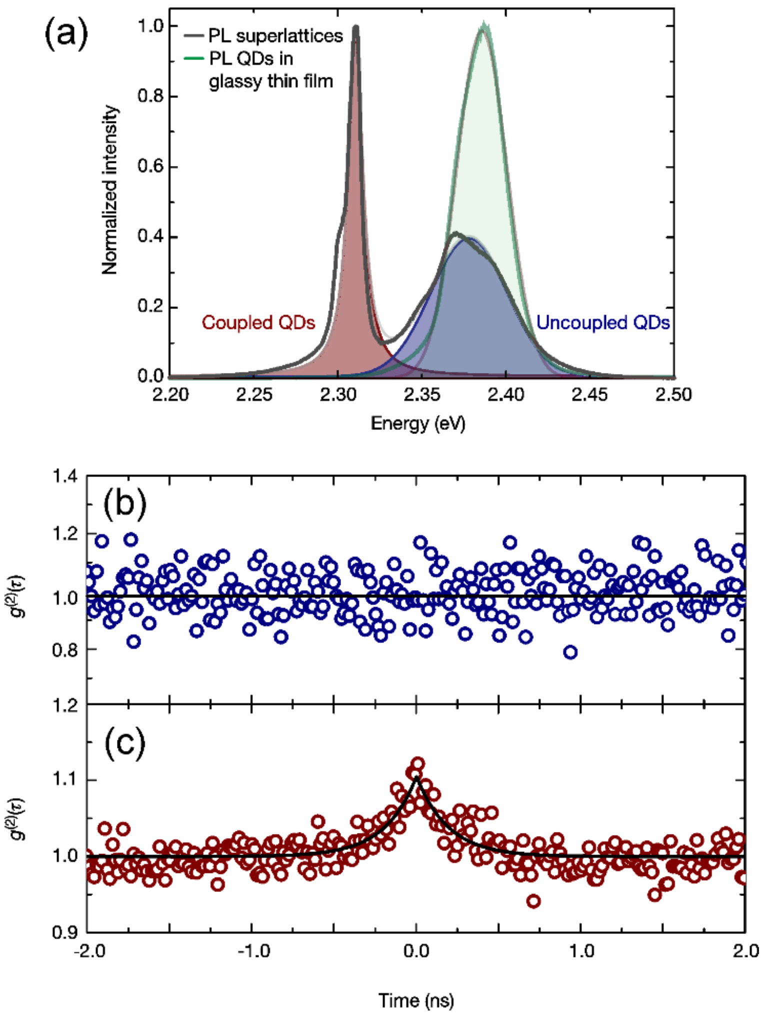

FIG. 6. Emergence of superradiance and photon bunching from coupled perovskite quantum dots. (a) PL spectrum of a superlattice of $CsPbBr_3$ perovskite nanocrystal quantum dots (black solid line). The high-energy band, i.e. the blue-shaded area, is assigned to the emission of uncoupled QDs, the red low-energy feature corresponds to coupled QDs. The low-energy band is not present in glassy films of nanocrystals (green solid line). (b, c) $g^{(2)}(\Delta t)$ obtained with an HBT setup, showing a flat curve for the high-energy emission band (uncoupled QDs) (b) and photon bunching from the low-energy emission band (coupled QDs) (c). Reproduced with permission from Nature 563, 671 (2018). Copyright 2018 Springer Nature.

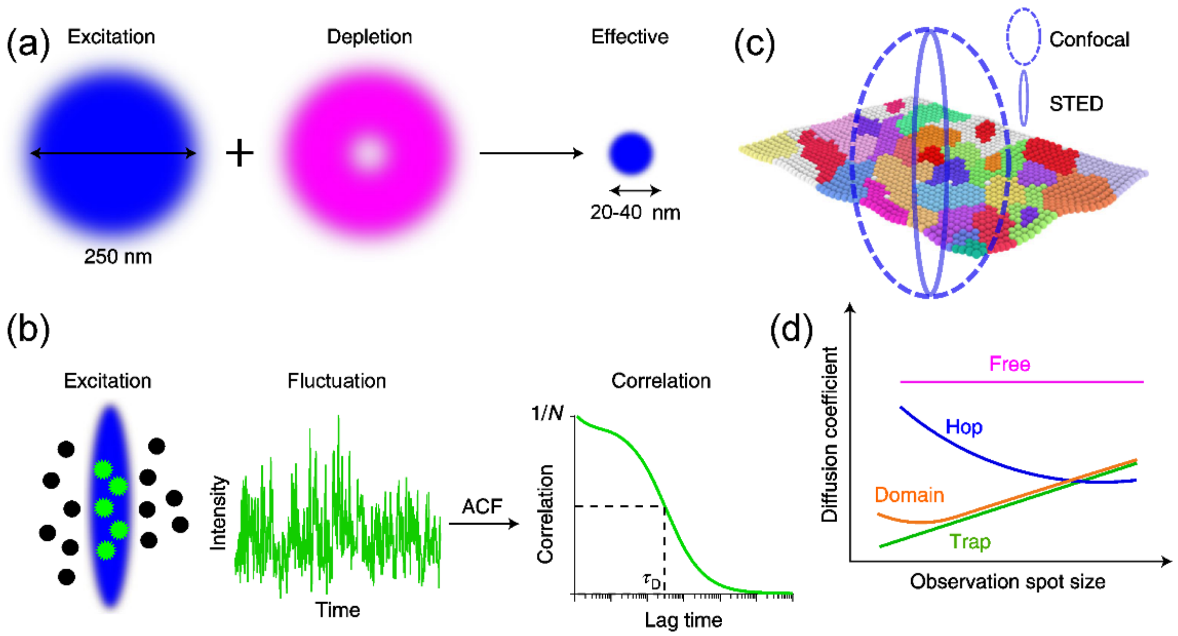

FIG. 7. Superresolution microscopy combined with fluorescence correlation spectroscopy (FCS). (a) STED microscopy relies on the depletion of spontaneous emission from excited molecules (blue) via stimulated emission induced by an additional laser featuring a local intensity zero in the center of the beam profile (magenta), thereby creating a subdiffraction-sized effective observation volume. (b) FCS measures the average transit time of fluorescent molecules (left: black and green circles) diffusing through the observation volume of a fluorescence microscope (blue) from recordings of the temporal fluorescence intensity fluctuations (center) and subsequent calculation of the temporal autocorrelation function (ACF, right) of the fluctuations, i.e. $g^{(2)}(\Delta t)$, in the fluorescence signal detected. The ACF decays with a characteristic time scale, the "transit time" τ_{D}, i.e. the average time a molecule takes to diffuse through the observation spot, and is defined by an amplitude 1/N, where N is the average number of fluorescent molecules in the observation volume. (c) Sketch of nanoscale plasma membrane heterogeneity, which can be detected with STED–FCS but not with a large confocal observation volume. (d) STED–FCS results in a series of diffusion coefficient measurements from FCS recordings that are obtained at various differently sized effective observation spots. This approach makes it possible to distinguish between free Brownian diffusion (purple) and hindered diffusion modes such as transient trapping (green), transient domain occupation (orange), or combined hopping diffusion (blue) on the relevant subdiffraction spatial scales (<200-nm observation spot sizes). Reproduced with permission from Nat. Prot. 14, 1054 (2019). Copyright 2019 Springer Nature.

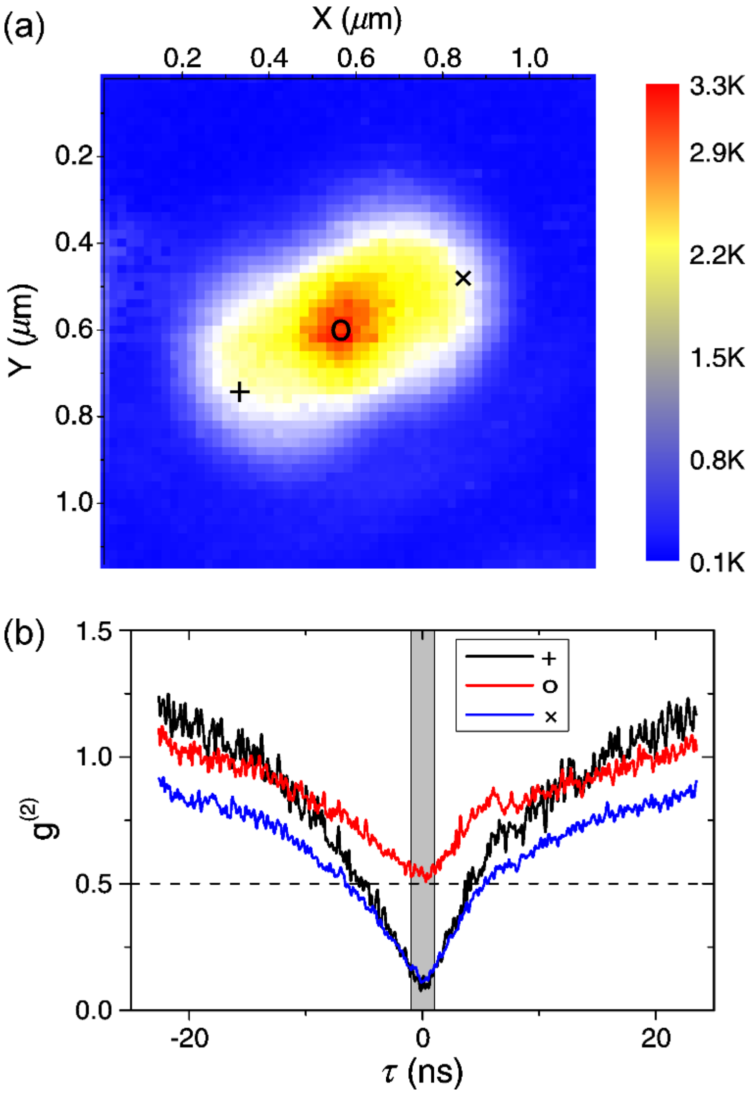

FIG. 8. Superresolution fluorescence microscopy by photon correlation spectroscopy. (a) Confocal image of two nitrogen vacancy (NV) centers in diamond, separated in space by ~366 nm. The luminescence intensity scale is shown on the right. (b) $g^{(2)}(\Delta t \equiv \tau)$ measurements at different points of the image as marked in (a), showing different degrees of photon antibunching. Reproduced with permission from Phys. Rev. Lett. 110, 153901 (2013). Copyright 2013 by the American Physical Society.

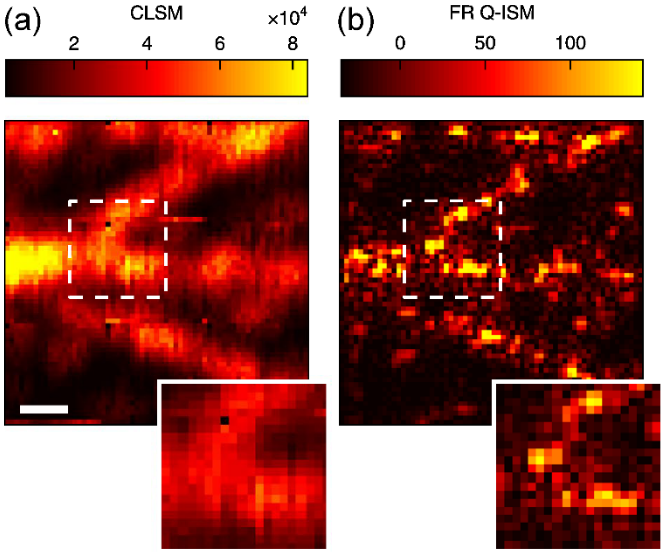

FIG. 9. Quantum-enhanced superresolution microscopy of a biological specimen. (a) Conventional confocal laser-scanning microscopy (CLSM) image and (b) Fourier reweighted "quantum image scanning microscopy" (FR Q-ISM) image, determined by analyzing the photon correlation function, analyzed from a confocal scan (50 nm steps, 100 ms pixel dwell time) of a 3 µm × 3 µm section of microtubules in a fixed mouse embryonic fibroblast 3T3 cell labelled with fluorescent quantum dots. The color bar for (a) represents the number of detected photon counts and the color bar for (b) indicates the number of missing detected photon pairs, i.e. the degree of photon correlations. Reproduced with permission from Nat. Photon. 13, 116 (2019). Copyright 2019 Springer Nature.

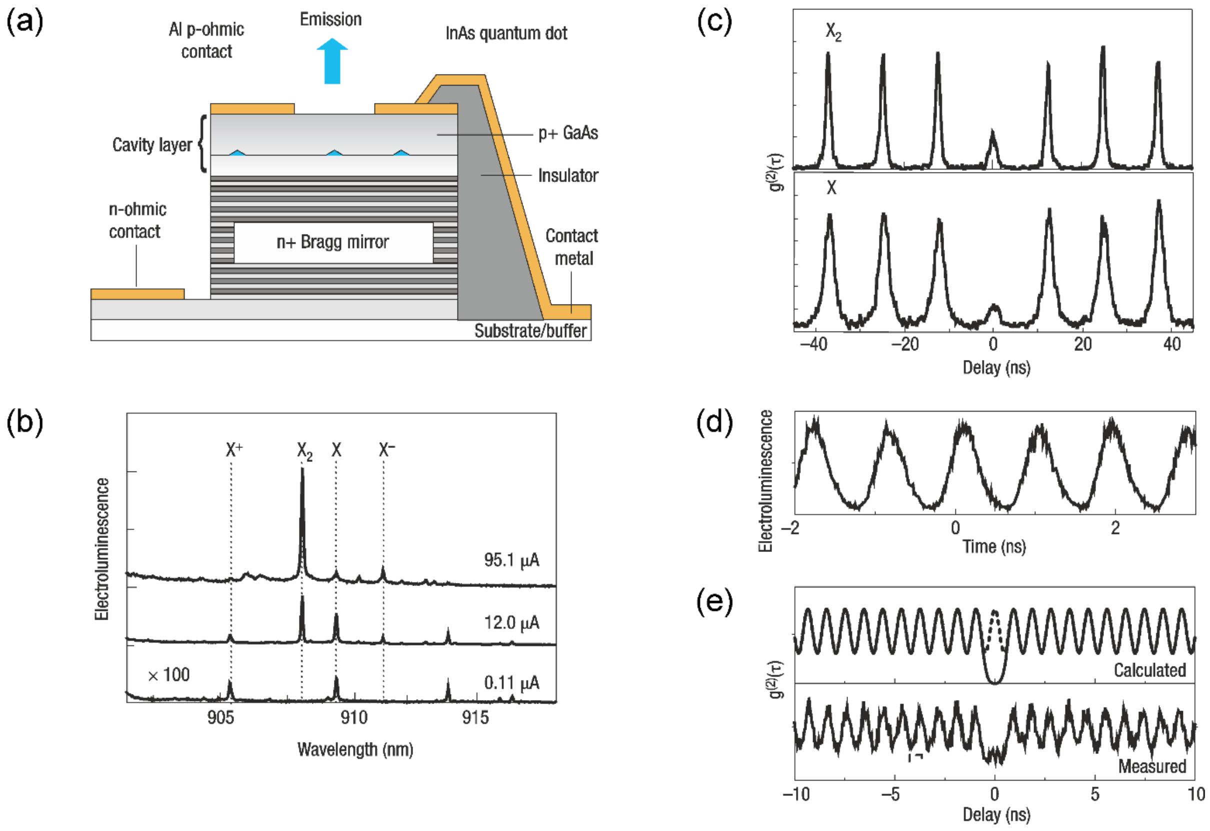

FIG. 10. Electrically driven single-photon emission. (a) Schematic of a single-photon LED. (b) Electroluminescence spectra of the device. Note that the spectra are dominated by the exciton X and biexciton X_2 emission lines, which have linear and quadratic dependencies on drive current, respectively. Other weak transition lines arise due to charged excitons. (c) Second-order correlation function recorded for the biexciton (top) and exciton (bottom) emission lines. (d) Time-resolved electroluminescence from a device operating under sinusoidal electrical drive of 1.07 GHz frequency. (e) Modelled (top) and measured (bottom) $g^{(2)}(\Delta t \equiv \tau)$ of the biexciton electroluminescence at 1.07 GHz. Reproduced with permission from Nat. Photon. 1, 215 (2007). Copyright 2007 Springer Nature.

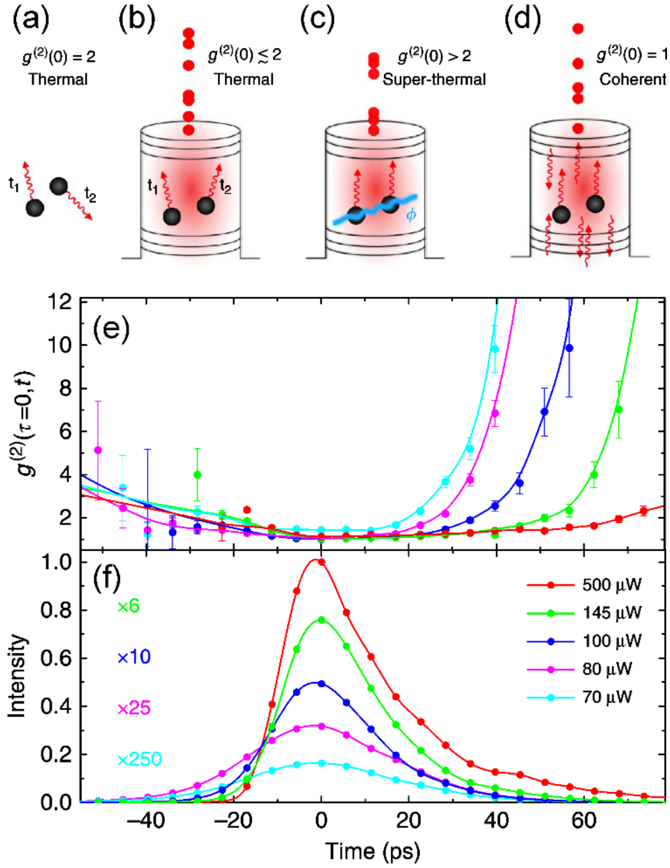

FIG. 11. Photon statistics in the excitonic recombination luminescence of quantum-dot lasers. (a) Spontaneous recombination from independent emitters gives rise to thermal, i.e. chaotic, radiation. (b) Using three-dimensional photon confinement in a cavity-quantum-electrodynamics (cQED) laser, spontaneous emission is directed into a single resonator mode. For independent emitters, below the threshold of stimulated emission, the photon emission is uncorrelated, producing thermal or close-to-thermal light. (c) The exchange of photons between excitons introduces correlations between the electronic states of different emitters. Information on a relative phase Φ is established spontaneously, and the emission from this entangled many-particle state then leads to a superradiant pulse with giant photon bunching. (d) Above threshold, stimulated emission dominates the radiative processes, leading to coherent radiation. Measurements of $g^{(2)}(\tau = 0, \mathrm{t})$ (i.e. $g^{(2)}(\Delta \mathrm{t} = 0, \mathrm{t})$) (e) and of the time-resolved luminescence output intensity (f) after pulsed excitation of the nanolaser structure with various intensities, i.e. excitonic population densities. For each pump intensity, the time zero is shifted to the output-pulse maximum. The lines are guides to the eye. Jahnke, F., Gies, C., Assmann, M., Bayer, M., Leymann, H. A. M., Foerster, A., Wiersig, J., Schneider, C., Kamp, M. & Höfling, S. Nat. Commun. 7, 11540 (2016); licensed under a Creative Commons Attribution (CC BY) license.

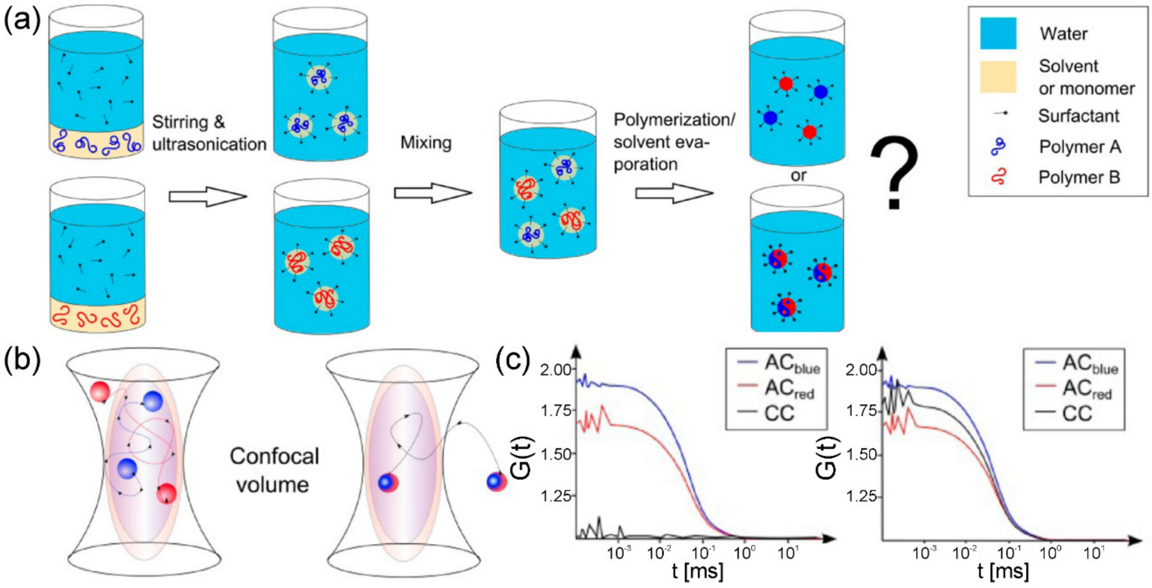

FIG. 12. Tracking polymer self-assembly by FCS. (a) Two differently fluorescently labeled polymers are dissolved in an organic solvent or monomer and dispersed via stirring and ultrasonication prior to mixing. Polymerization or solvent evaporation leads to the formation of dispersed stable nanoparticles. (b) The two spatially overlapping observation volumes created by the “blue” and “red” laser excitation with differently labeled species diffusing either independently (left) or together (right). (c) Corresponding correlation curves ($G(t) \equiv g^{(2)}(\Delta t)$) in relation to (b). Reproduced with permission from Nano Lett. 12, 6012 (2012). Copyright 2012 American Chemical Society.

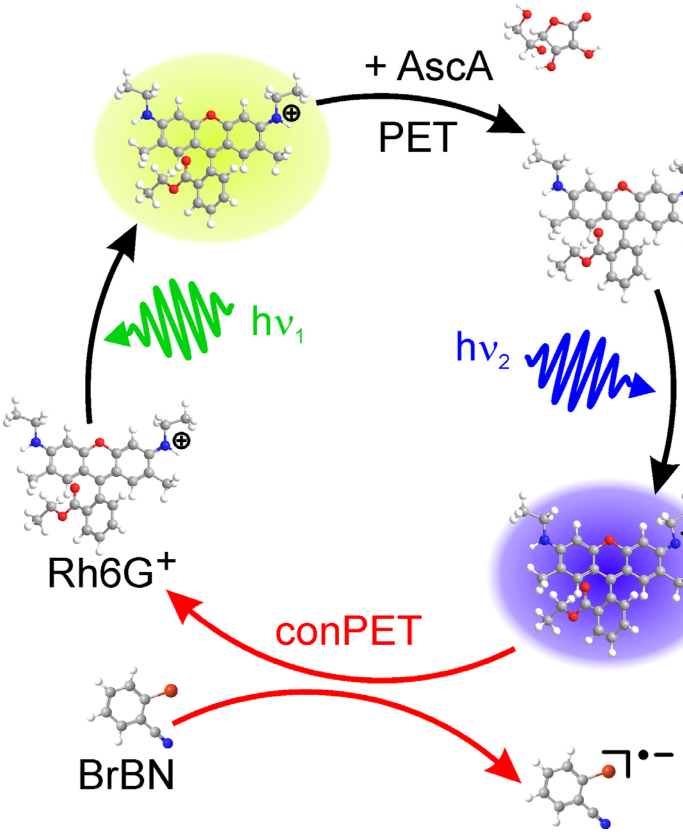

FIG. 13. Single-photon single-molecule photocatalytic cycle, driven by consecutive photoinduced electron transfer (conPET). A cationic rhodamine 6G (Rh6G) dye molecule in phosphate-buffered saline (PBS) is excited by a photon of energy $h\nu_1$ and is subsequently reduced by ascorbic acid (AscA) to form a radical. A second photon $h\nu_2$ excites the radical, leading to PET to the halogenated substrate molecule 2-bromobenzonitrile (BrBN). The dye is immobilized in solution by a DNA tether so that the FCS signal is not determined by diffusion. Haimerl, J., Ghosh, I., König, B., Vogelsang, J. & Lupton, J. M. Chem. Sci. 10, 681 (2019); licensed under a Creative Commons Attribution (CC BY) license.

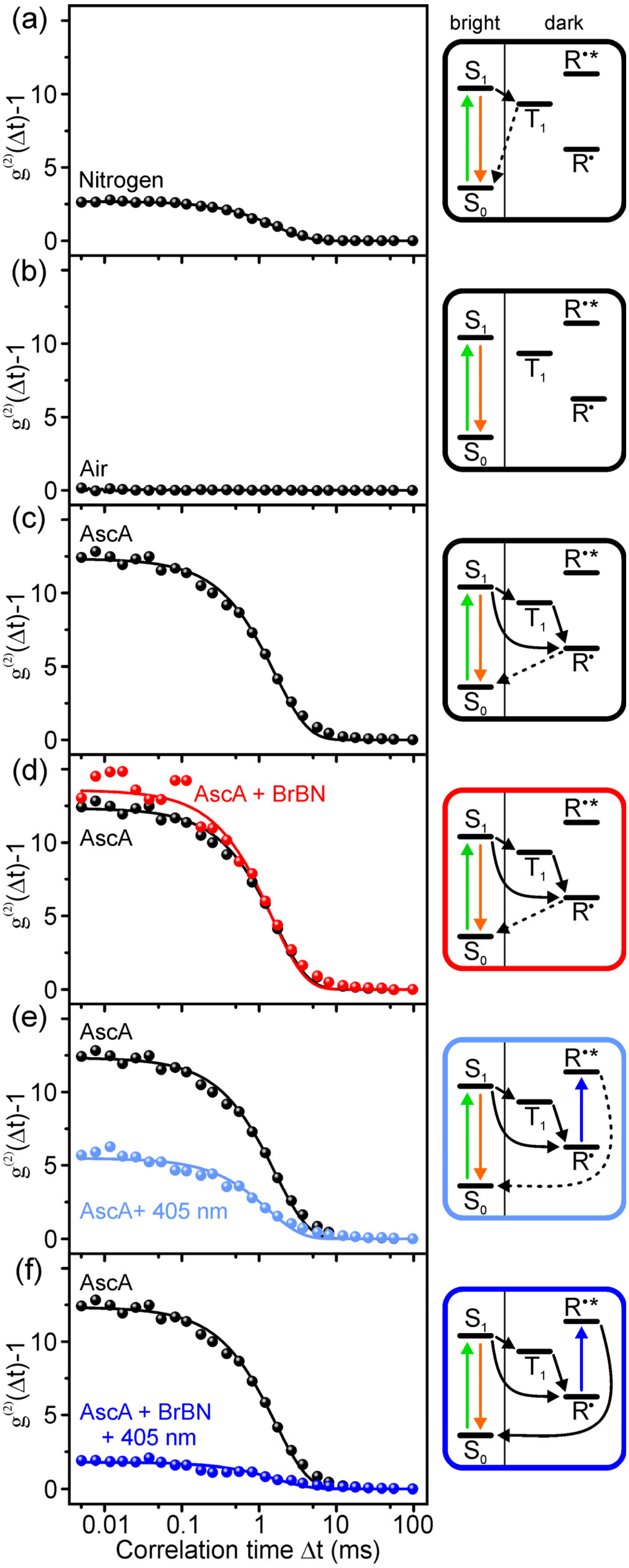

FIG. 14. Control of fluorescence intensity correlations of single Rh6G molecules through the reaction conditions. The plots show median values of the correlations, $g^{(2)}(\Delta t) - 1$, at each time Δt for one hundred single molecules each, with single-exponential fits to describe the dark-

state lifetime. The level schemes responsible for each correlation signal are indicated on the right. (a) Rh6G in N_2-saturated solution. (b) Rh6G in air-saturated solution, where the triplet excited state is quenched. (c) Rh6G in N_2-saturated solution with the reducing agent ascorbic acid (AscA) added to form a dye radical. (d) As in panel c, but with the substrate molecule 2-bromobenzonitrile (BrBN) added. (e) As in panel c, but with the "reagent photon" $h\nu_2$ added, which raises the radical to an excited state. (f) As in panel e, but with the substrate molecule BrBN added. Only in this last case is the dark state of the fluorophore removed by the closed conPET cycle of Fig. 13, so that the correlation curve appears flat. Haimerl, J., Ghosh, I., König, B., Vogelsang, J. & Lupton, J. M. Chem. Sci. 10, 681 (2019); licensed under a Creative Commons Attribution (CC BY) license.

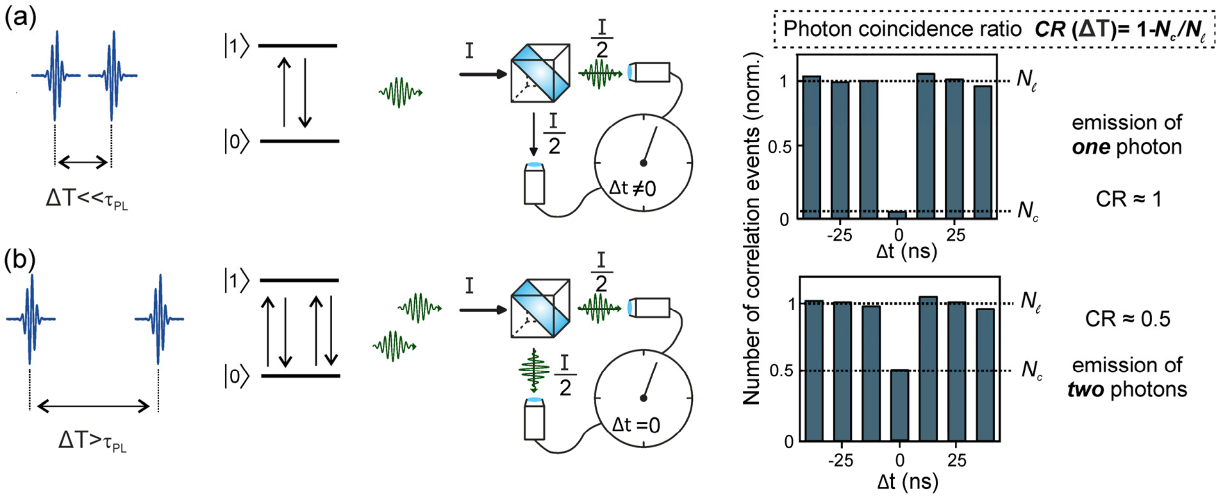

FIG. 15. Probing ultrafast excited-state dynamics by measuring photon antibunching under double-pulse excitation. (a) Two laser pulses are incident on a single emitter, separated in time by $\Delta T \ll \tau_{\mathrm{PL}}$, where τ_{PL} is the excited-state lifetime of the molecule, the PL decay time. Because the emitter can only generate one single photon at a time, photon antibunching is observed in the coincidence rate of two photodetectors. Photon coincidences on the detectors will occur for finite time differences Δt, i.e. for multiples of the period of the pulsed laser, but not for $\Delta t = 0$, provided that the second excitation pulse arrives before the molecule has relaxed to the ground state. These coincidences are graphed in a histogram, where N_{c} describes the number of coincidences at the center (i.e. for $\Delta t = 0$) and N_{ℓ} the lateral coincidence peak height, to which the distribution is normalized. (b) If the second laser pulse arrives after a long delay time ($\Delta T \gg \tau_{\mathrm{PL}}$), the emitter will have relaxed so that it can absorb a second photon, resulting in a photon coincidence signal at $\Delta t = 0$. The "photon coincidence ratio", i.e. the contrast of the photon antibunching histogram defined as $CR(\Delta T) = 1 - N_{\mathrm{c}}(\Delta T)/N_{\ell}$, gives a measure of the excited-state population at time ΔT. Reproduced with permission from Nano Lett. 20, 1074 (2020). Copyright 2020 American Chemical Society.

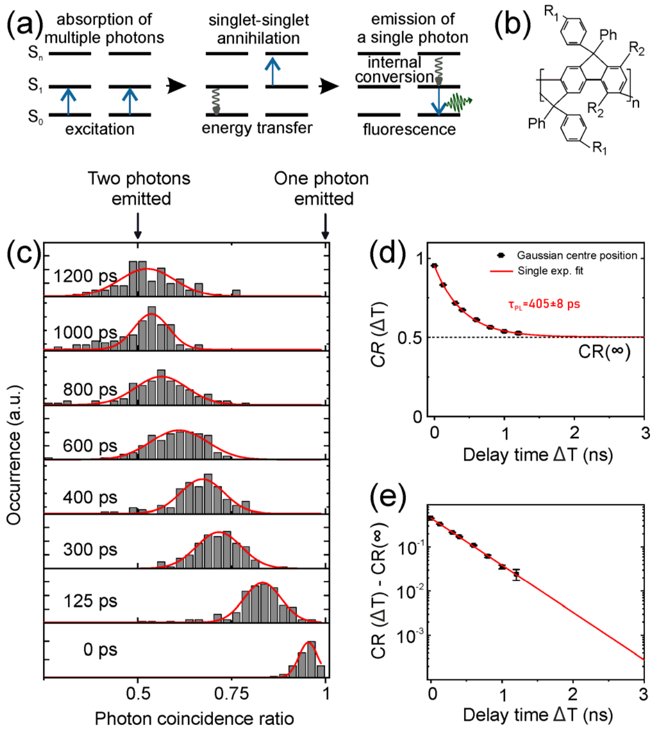

FIG. 16. Excited-state dynamics in single multichromophoric π-conjugated polymer chains. (a) The polymer phenyl-substituted ladder-type poly(*para*-phenylene) (LPPP, structure shown in (b)) forms distinct chromophores, which couple to each other by excitation-energy transfer. When multiple chromophores are excited within one chain, excitations annihilate each other by raising a chromophore to a higher-lying state S_n, which subsequently dissipates energy non-radiatively by internal conversion. (c) Histograms of photon coincidence ratios determined for 100 single chains immobilized in PMMA measured at different delay times Δt, excited at 405 nm. The delay time between the two pulses is stated in each histogram. Gaussian fits (red curves) were used to extract the center position and the corresponding fitting errors for further analysis. (d) Decay of the average photon coincidence ratio (black dots) with time on a linear (d) and a semilogarithmic scale (e), together with single-exponential fits (red curves). Reproduced with permission from Nano Lett. 20, 1074 (2020). Copyright 2020 American Chemical Society.

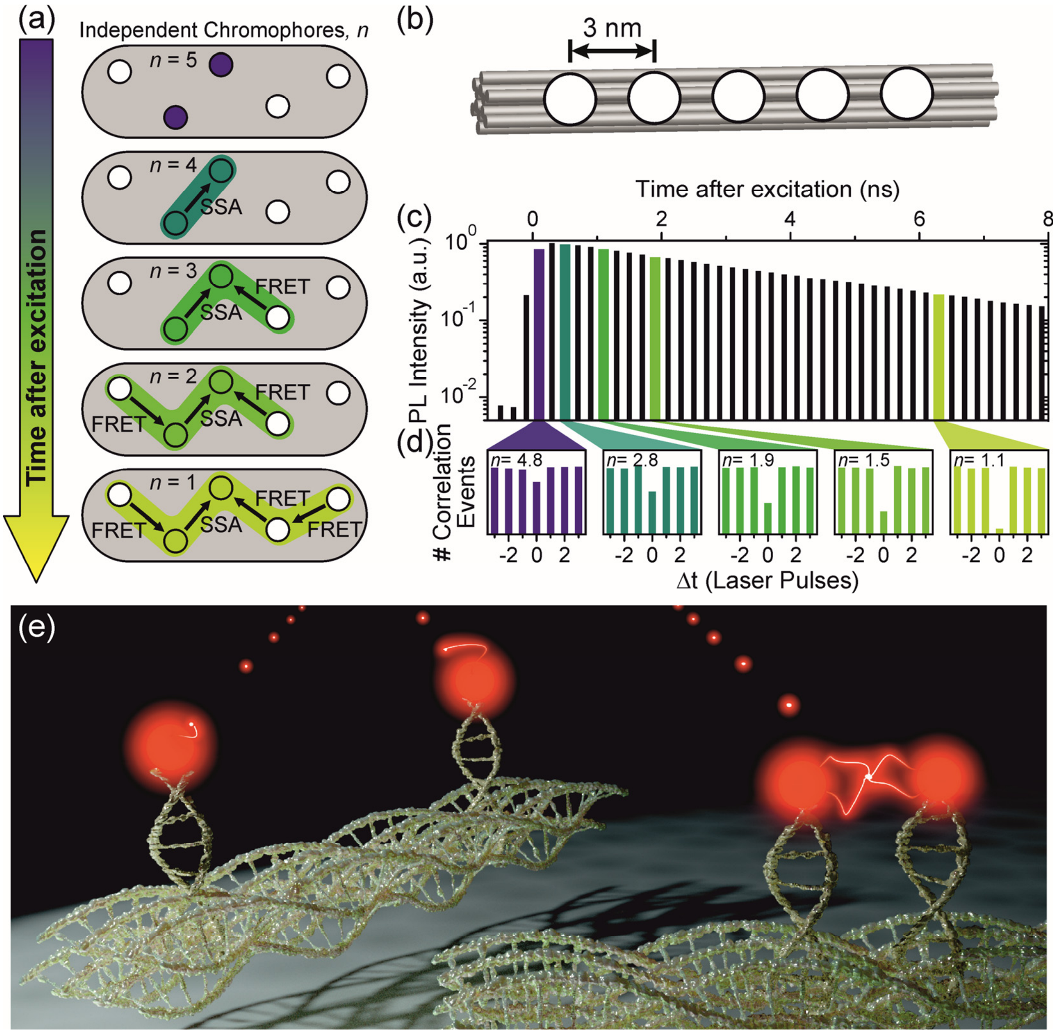

FIG. 17. Resolving the number of independent chromophores in a multichromophoric structure in time. (a) Five chromophores (discs) in a nanoparticle are shown schematically. Two singlet excitons occupy the system (colored discs). After photoexcitation, these excitons can diffuse by site-to-site hopping, i.e. by homo-FRET between the dye molecules, and annihilate by singlet-singlet annihilation (SSA) during the excited-state lifetime. (b) Schematic of a short part of a 225-nm-long 12-helix-bundle DNA-origami structure with six inner and six outer helices. Five dyes (white discs) can be positioned at 3-nm spacing from each other. (c) Measured photoluminescence (PL) decay of a single DNA-origami structure with five dye molecules. A single-exponential decay is observed with a PL lifetime of 4.2 ns. Panel (d) shows five corresponding histograms of photon statistics for different “microtime” bins (0-200 ps, 200-400 ps, 800-1000 ps, 1,600-1,800 ps and 6,400-6,600 ps after excitation), i.e. for different photon arrival times. Data were accumulated for 54 single multichromophoric nanoparticles. The number of independent chromophores, n, determined from the correlation histogram for each microtime bin is stated in the plots. (e) Schematic of two DNA origami structures with

two dye molecules (red dots) attached to each. In the upper part of the figure, the dye molecules do not interact with each other and both emit single photons (small red dots) per instant in time. In the lower part of the figure, both dyes interact with each other and therefore, in terms of their quantum-optical characteristics, effectively behave as one single dye molecule. Hedley, G. J., Schröder, T., Steiner, F., Eder, T., Hofmann, F., Bange, S., Laux, D., Höger, S., Tinnefeld, P., Lupton, J. M. & Vogelsang, J. Nat. Commun. 12, 1327 (2021); licensed under a Creative Commons Attribution (CC BY) license.

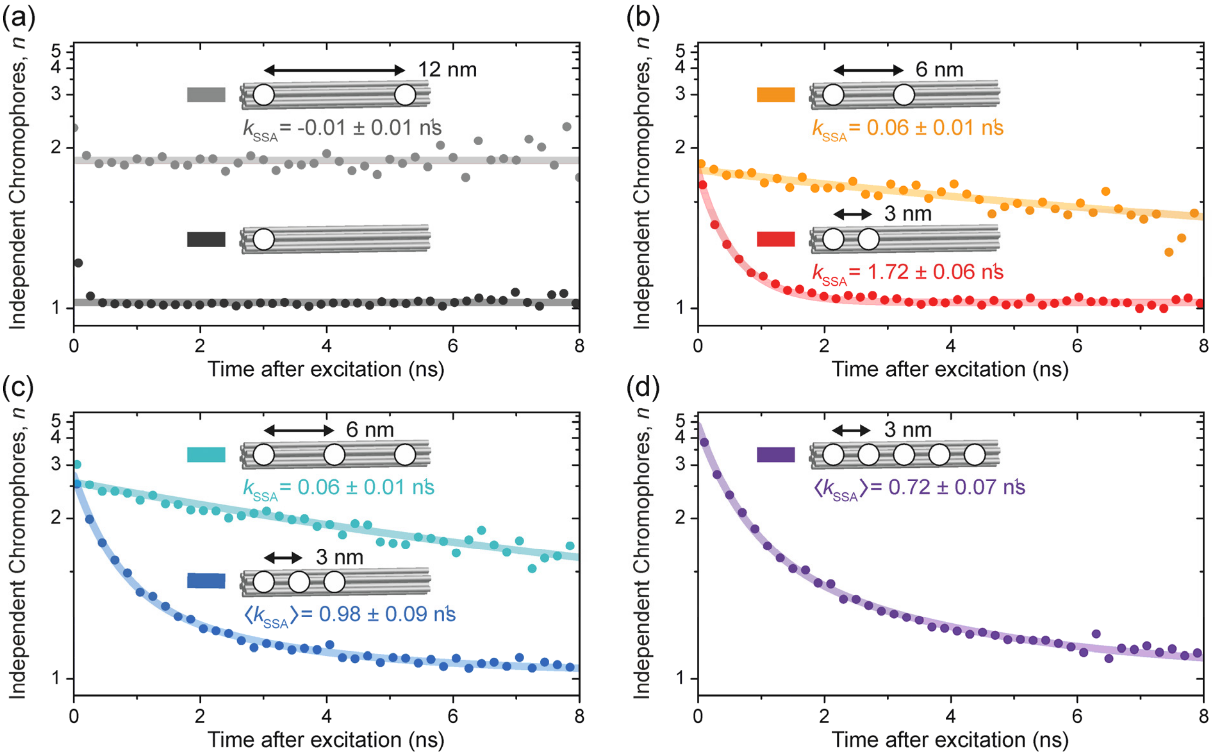

FIG. 18. Exciton-exciton annihilation in different well-defined multichromophoric nanoparticle structures. The evolution of the number of independently emitting chromophores, n, as a function of the time after excitation is shown for seven different structures. The structures have different numbers of dyes incorporated with different spacings between the dyes to control the frequency of site-to-site hopping, i.e. the effectiveness of homo-FRET. The y-axes are shown on a reciprocal scale to allow for better comparison between the graphs. (a) One dye molecule (dark grey) and two dye molecules separated by 12 nm (light grey). (b) Two dye molecules separated by 6 nm (orange) and 3 nm (red). The curves superimposed are described by a single-exponential model of exciton annihilation. (c) Three dye molecules separated by 6 nm (cyan) and 3 nm (blue). The cyan curve is described by the relation $n(t) = \{y_0 - [A \cdot \exp(-k_{\mathrm{SSA}}\, t)]\}^{-1}$, but the blue points follow a biexponential decay of the form $n(t) = \{y_0 - [A_1 \exp(-k_{\mathrm{SSA},1} \cdot t) + A_2 \exp(-k_{\mathrm{SSA},2} \cdot t)]\}^{-1}$, with an amplitude-weighted average SSA rate $\langle k_{\mathrm{SSA}}\rangle$ as stated in the figure. (d) Five dyes separated by 3 nm. The curve is again described by the biexponential decay. Between 54 and 98 single DNA-origami structures were measured individually, and the photon statistics of each measurement were accumulated to obtain each correlation curve. Each particle was measured for only 5 s to ensure that photobleaching and spectral shifts were negligible during data acquisition. Hedley, G. J., Schröder, T., Steiner, F., Eder, T., Hofmann, F., Bange, S., Laux, D., Höger, S., Tinnefeld, P.,

Lupton, J. M. & Vogelsang, J. Nat. Commun. 12, 1327 (2021); licensed under a Creative Commons Attribution (CC BY) license.

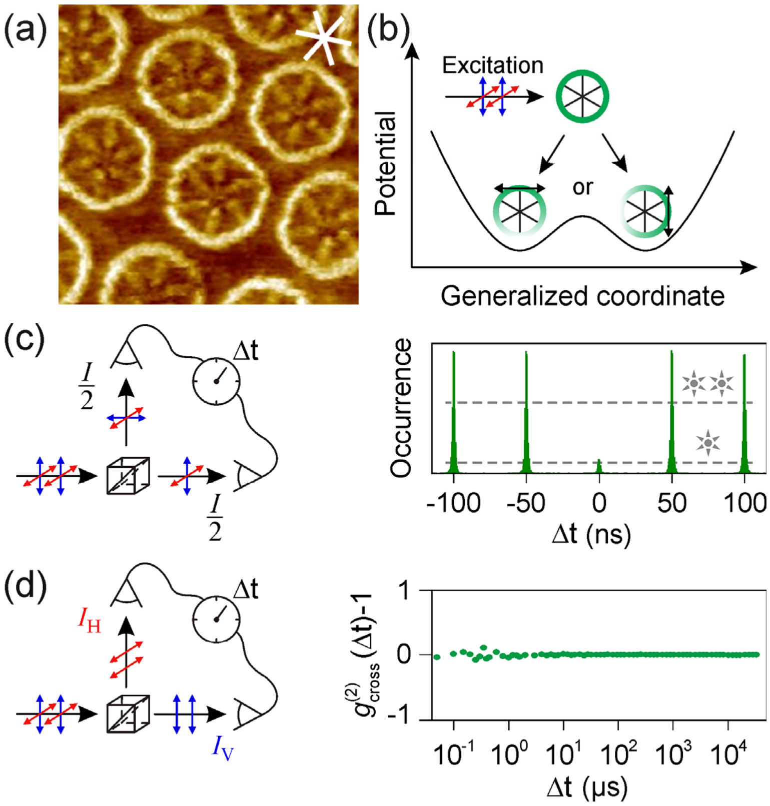

FIG. 19. Spontaneous symmetry breaking in the excited state of a giant π-conjugated spoked-wheel macrocycle. (a) 19×19 nm² STM image of the molecules on graphite with the crystal axes of the substrate indicated in white. (b) Excitation with light of arbitrary polarization leads to exciton formation. Excitons relax to segments of length comparable to the size of two repeat units, whereas the ring consists of six identical units. Owing to bond-length changes in the excited state, the local potential surface in the proximity of the exciton is modified. Such exciton localization occurs at random anywhere on the ring perimeter. (c) Temporal photon correlation under pulsed excitation. Fluorescence passes through a beam splitter and is recorded with two photodiodes. At a delay time of $\Delta t = 0\,ns$ between the detectors, the photon coincidence approaches zero; photon antibunching implies the activity of precisely one chromophore in the macromolecule. Dashed lines indicate the calculated thresholds for one (lower) and two emitters (upper) given the signal strength in comparison to the noise. The experiment was carried out at a repetition rate of 20 MHz, which gives the 50-ns spacing on the Δt axis. (d) The cross-correlation function $g^{(2)}_{\text{cross}}(\Delta t) - 1$ between two detector channels of orthogonal polarization shows no discernible timescale for polarization fluctuations, which implies that the ring emission appears unpolarized. Reproduced with permission from Nat. Chem. 5, 964 (2013). Copyright 2013 Springer Nature.

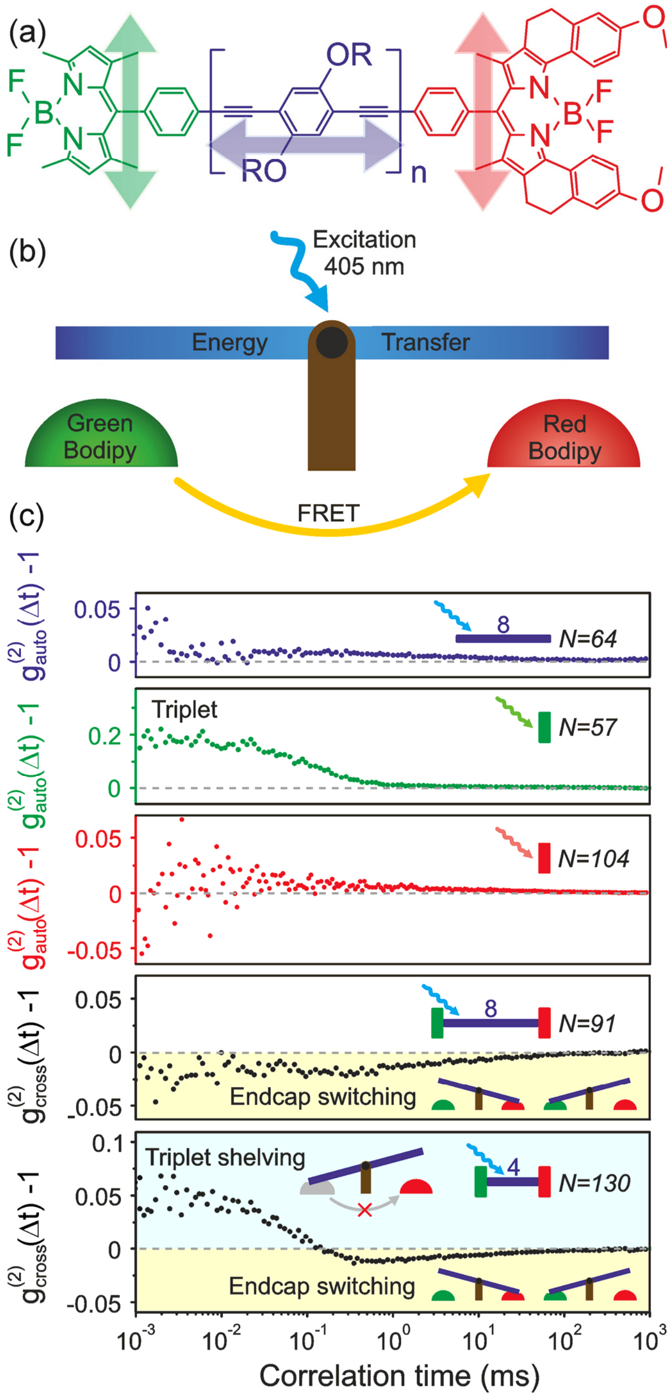

FIG. 20. Spontaneous symmetry breaking in the excited state of an excitonic "seesaw" molecule. (a) Chemical structure of the molecule consisting of an oligo(phenylene-butadiynylene) π-conjugated donor (blue) and a green and red dye endcap acceptor of "bodipy" (boron-dipyrromethene) derivatives. (b) Energy transfer can occur either from the backbone to one of the endcaps, or through conventional FRET from the green to the red bodipy dye. (c) Fluorescence photon correlation, $g^{(2)}(\Delta t) - 1$, of the three constituents of the excitonic seesaw with 8 repeat units of the oligo(phenylene-butadiynylene), measured using only one luminescence channel (color) to determine the autocorrelation, and of the excitonic seesaw with

8 and 4 repeat units, measured using a dichroic mirror to separate red and green endcap fluorescence to determine the intensity cross-correlation between the different emitters. All measurements were performed in air to maximize the molecular brightness by efficiently depopulating the dark triplet states. The number of molecules measured for each correlation is indicated by N. A positive correlation due to the triplet shelving effect is only seen for the excitonic seesaw structure with 4 repeat units, where substantial through-space FRET between the endcaps occurs. The absence of such a positive correlation for the excitonic seesaw with 8 repeat units implies that the shelving of one endcap in a dark state does not impact the energy transfer from the backbone to the other endcap. Reproduced with permission from Proc. Natl. Acad. Sci. U. S. A. 115, E3626 (2018). Copyright 2018 National Academy of Sciences, U.S.A.

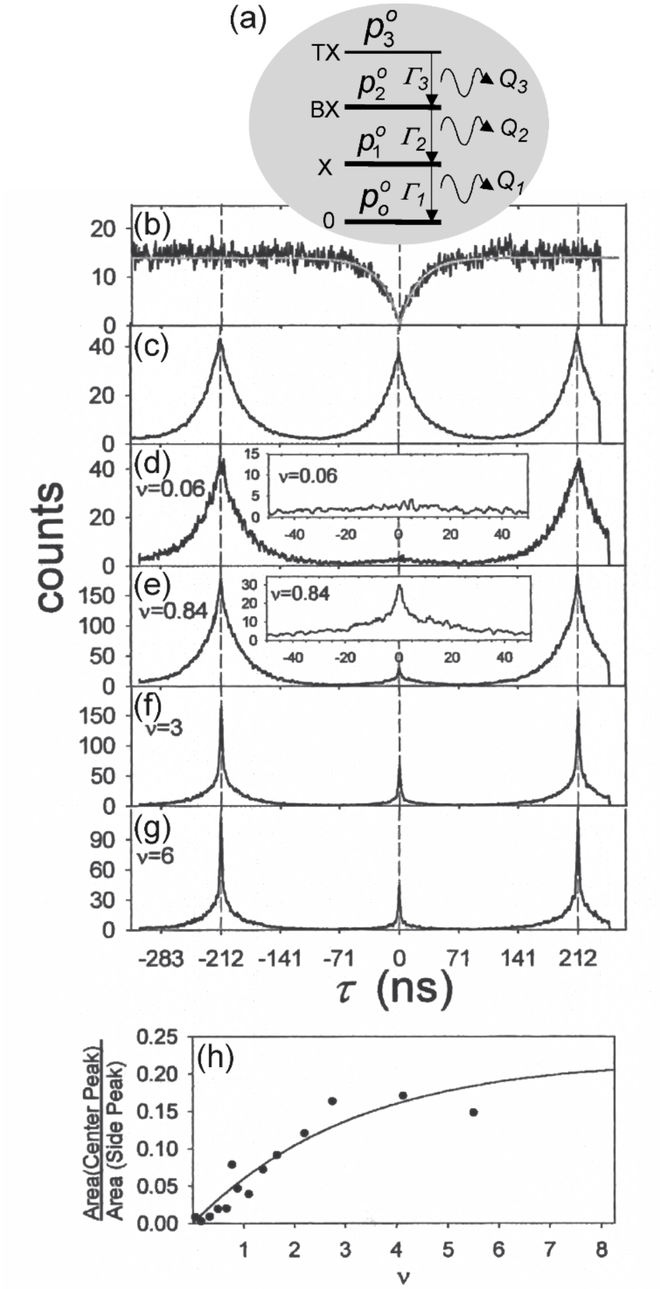

FIG. 21. Ordered photon emission from multiexciton states in single CdSe nanocrystal quantum dots. (a) Schematic of a four-level system of a single nanocrystal with a ground state, 0, a single excitonic state, X, and biexcitonic, BX, and triexcitonic, TX, states. The initial population numbers of the states p_i^0 are determined by the Poisson distributed probability of exciting 0, 1, 2, and >2 excitons in a nanocrystal, given an average number ν of excitons generated per laser pulse. (b) Number of photon coincidences for a single quantum dot under CW excitation with an exponential fit (grey line), which yields a ratio of central to lateral peaks of $N_c/N_\ell = 0.025$. (c) Same as in (b), but for a collection of single nanocrystals and under low-intensity and pulsed excitation. (d-g) Same as in (c), but for single nanocrystals under different excitation intensities. (h) N_c/N_ℓ versus excitation density along with the calculated value (solid line). Reproduced

with permission from Phys. Rev. Lett. 94, 087403 (2005). Copyright 2005 by the American Physical Society.

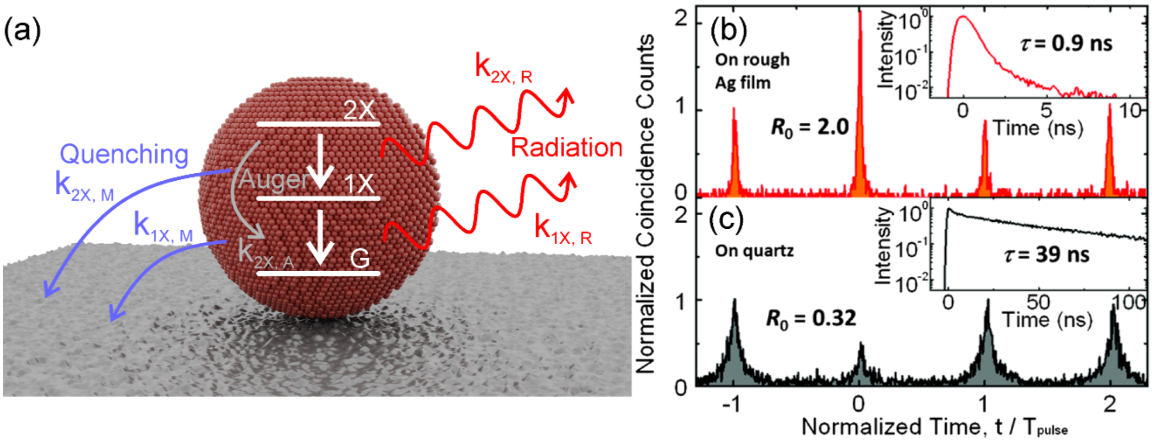

FIG. 22. Photon bunching from biexcitons in giant single CdSe nanocrystal quantum dots. (a) Schematics of a quantum cascade process when a biexciton (2X) decays first to an exciton (1X) and then to a ground state (G) for a nanocrystal quantum dot coupled to a rough silver surface which enhances the emission rate. (b) $g^{(2)}(\Delta t)$ functions of single giant quantum dots deposited on a rough silver surface and on a quartz substrate (c). Insets in (b) and (c) display the PL decay of a single nanocrystal, illustrating the dramatic effect the silver film has on the luminescence lifetime. Reproduced with permission from Phys. Rev. Lett. 110, 117401 (2013). Copyright 2013 by the American Physical Society.

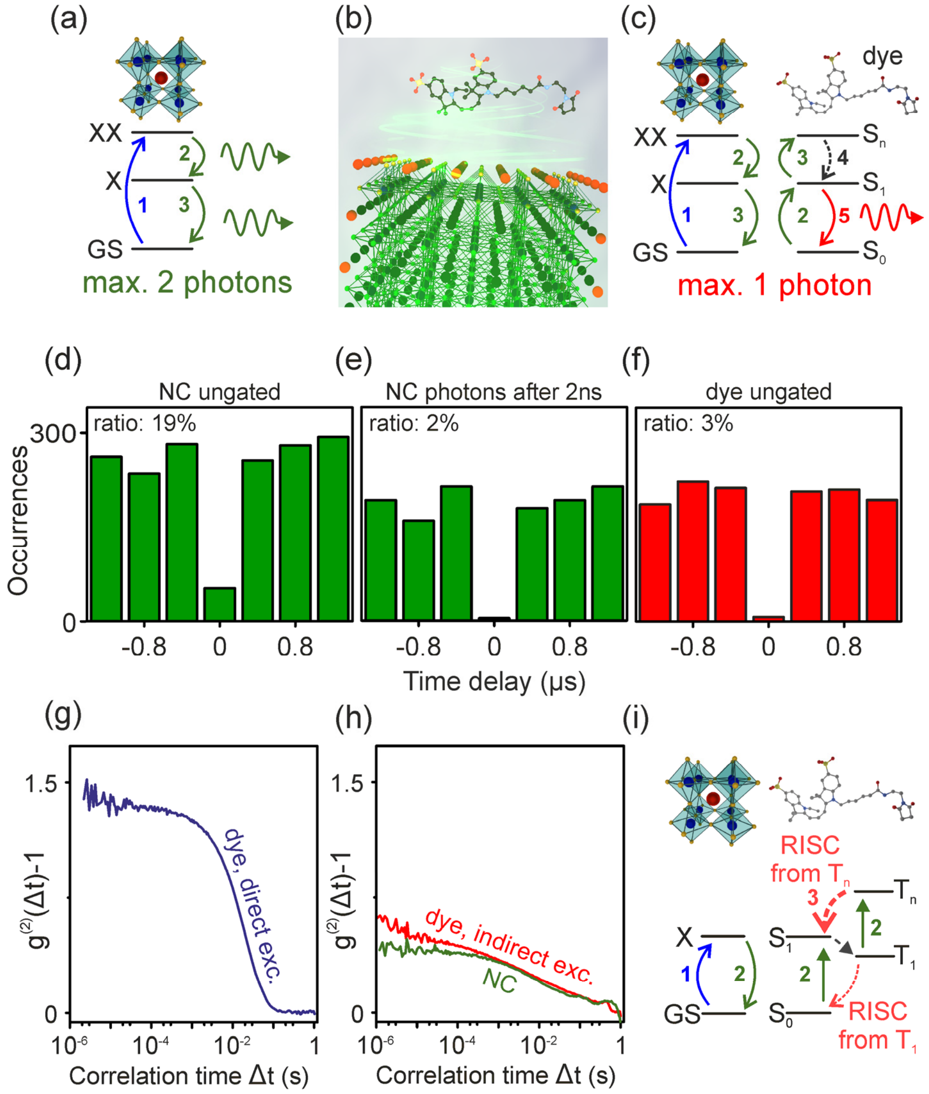

FIG. 23. Exciton gating and triplet deshelving in coupled arrangements of perovskite nanocrystal quantum dots and single dye molecules. (a) Illustrations of the biexciton emission process of single perovskite nanocrystals. (b) Schematic of a hybrid inorganic-organic “excitonic antenna” arrangement based on perovskite nanocrystals transferring excitation energy to fluorescent dye molecules. (c) Illustrations of the multiexciton gating process in a nanocrystal/dye pair. (d-f) Photon antibunching histograms from the nanocrystal/dye pair for the donor channel (green) and the acceptor channel (red). (d) Without gating out any photons by selecting specific microtimes, biexciton emission raises the photon coincidence peak at zero delay time. (e) By selecting only photons arriving more than 2 ns after the excitation pulse, detected in the spectral region of the nanocrystal donor emission, the biexciton contribution to the luminescence is effectively removed, lowering the N_c/N_ℓ ratio to 2 %. (f) Almost the same ratio is seen when considering only the dye emission of the nanocrystal/dye pair, without any electronic photon gating: the energy-transfer process to the dye acts as an effective gate to

biexcitonic contributions to the luminescence. (g) Typical intensity autocorrelation function of a single dye molecule, $g^{(2)}(\Delta t) - 1$, and (h) of a single NC/dye pair for the donor (green curve) and acceptor emission channel (red curve) under a nitrogen atmosphere, where the triplet state of the molecule is stabilized giving an exponential decay of the correlation. Photon bunching due to the triplet state is seen for the dye molecule under direct excitation but not under excitation by energy transfer from the nanocrystal. (i) Illustration of a proposed triplet deshelving mechanism by reverse intersystem crossing (RISC), which appears to be responsible for the decreased photon bunching in the dye emission due to triplet-state shelving when excited by energy transfer. Reproduced with permission from J. Phys. Chem. Lett. 10, 1055 (2019). Copyright 2019 American Chemical Society.

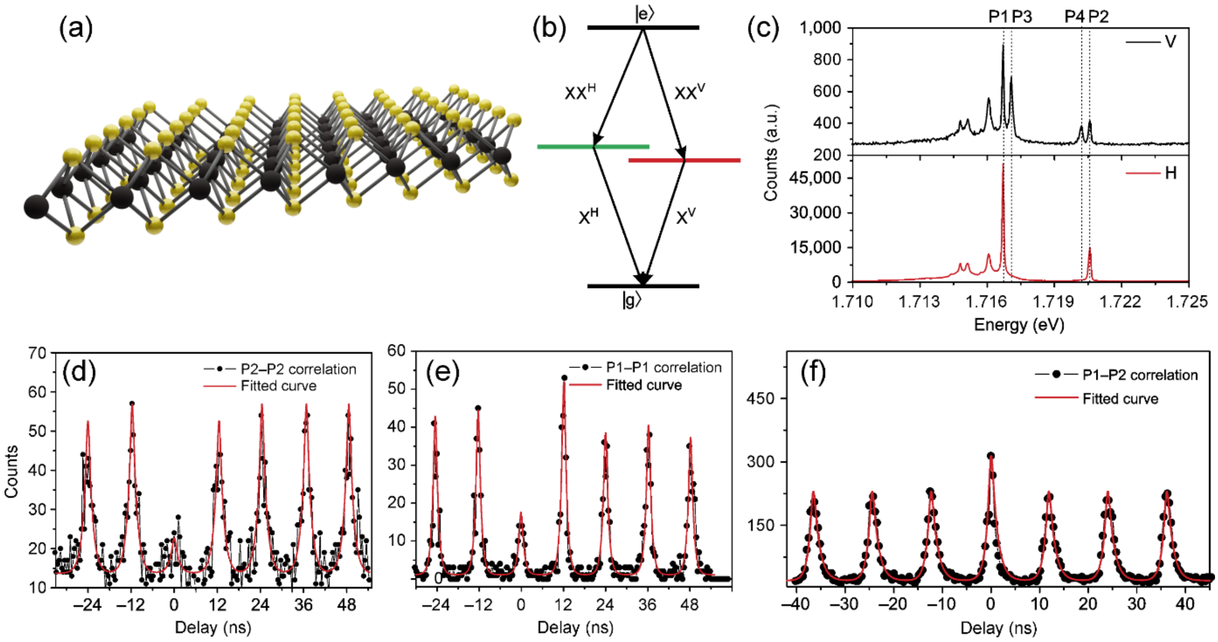

FIG. 24. Photon statistics in the luminescence of exfoliated monolayer WSe2 crystals at cryogenic temperatures. (a) Schematic illustration of a transition-metal dichalcogenide (TMDC) monolayer. (b) Energy-level diagram of the biexcitonic photon emission cascade. Fine-structure splitting is expected for the electron-hole exchange interaction in the presence of an in-plane anisotropy, lifting the degeneracy. (c) Polarization-resolved spectra measured under horizontally (H) and vertically (V) resolved linear polarizations. Two pairs of spectral doublets are observed at energies of 1.7167 eV (P1) and 1.7171 eV (P3); and at 1.7202 eV (P4) and 1.7206 eV (P2). Four peaks are indicated by the dashed lines. (d, e) $g^{(2)}(\Delta t)$ measurement of the P2 and P1 emission lines under 13.6 nW pulsed excitation at 475 nm with a repetition rate of 82 MHz and a pulse length of 3 ps. (f) $g^{(2)}(\Delta t)$ cross-correlation measurement between P1 and P2 emission lines under pulsed excitation. The red lines show fits to a biexponential decay of the excited-state population, convoluted with the response function of the photon-counting apparatus. He, Y. M., Iff, O., Lundt, N., Baumann, V., Davanco, M., Srinivasan, K., Höfling, S. & Schneider, C. Nat. Commun. 7, 13409 (2016); licensed under a Creative Commons Attribution (CC BY) license.

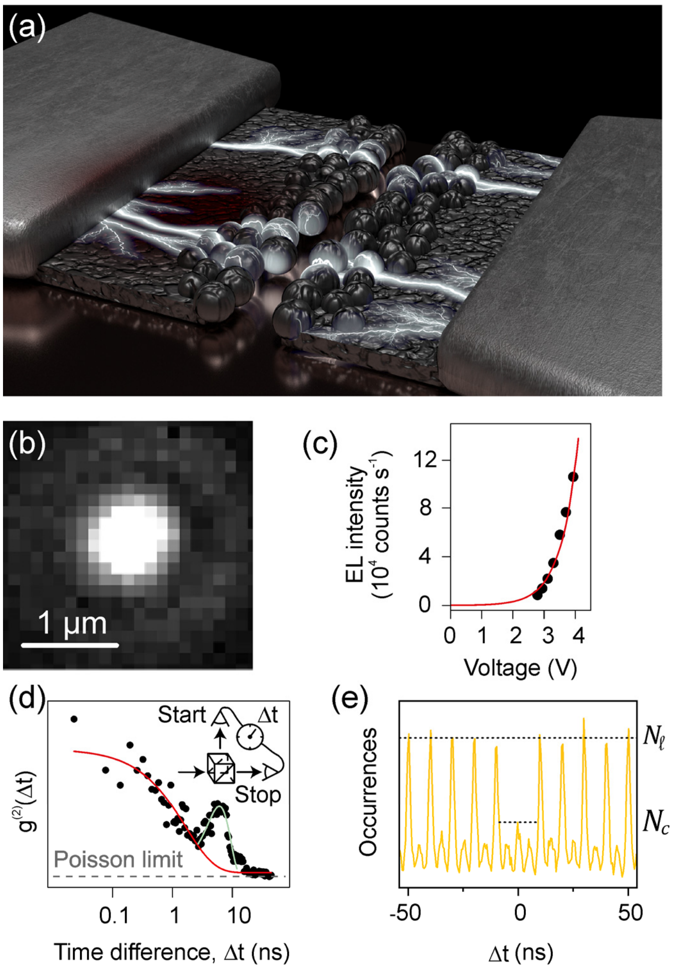

FIG. 25. Photon bunching and antibunching of electrically driven light emission from silver and gold nanoparticles, respectively. (a) Cartoon of the device structure. An evaporated 20 nm thin silver square is contacted by thicker silver electrode leads. Electromigration under current flow by application of a constant DC voltage gives rise to the formation of a break junction at the center of the thin square, where electroluminescence occurs. (b) Microscope image of a diffraction-limited electroluminescence spot. (c) Brightness–voltage characteristic of a single electroluminescence spot driven under AC bias to inhibit electromigration with an exponential fit to the data illustrating diode-like behavior. (d) Photon correlation of a single spot showing photon bunching on the timescale of 2 ns, which is assigned to the RC time constant of the nanoparticle aggregate. The electroluminescence in this case is driven under a DC bias. The red curve shows an exponential fit to the correlation with the Poisson limit of classical photon emission ($g^{(2)}(\Delta t) = 1$) marked by a grey dashed line. The peak at 8 ns in the autocorrelation, marked in light green, originates from the secondary photon emission, i.e. the afterglow, of the avalanche photodiodes used for detection. (e) Photon antibunching from a single electroluminescence spot under AC driving of a gold nanoparticle film. Reproduced with

permission from Nat. Nano. 12, 637 (2017). Copyright 2017 Springer Nature. Reproduced with permission from Small 17, 2006425 (2021). Copyright 2021 John Wiley and Sons.

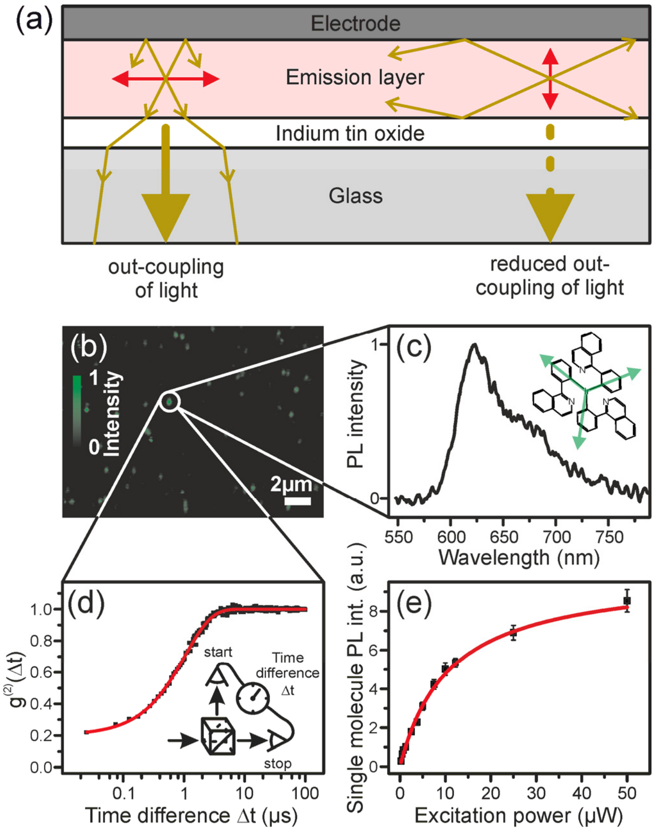

FIG. 26. Photon correlations in the phosphorescence from a single triplet-emitting molecule as used widely in OLEDs. (a) Effect of dipole orientation (red arrows) on light out-coupling in an OLED. Radiation polarized perpendicular to the plane of the emission layer is preferentially trapped by waveguiding effects. (b) Scanning confocal single-molecule microscope image of the $Ir(piq)_3$ emitter molecule under excitation at 485 nm. The chemical structure is inset in panel (c), which also shows a typical single-molecule PL spectrum. (d) Photon correlation spectroscopy of the single-molecule luminescence from the triplet state, i.e. phosphorescence, measured from one single molecule under pulsed excitation. The correlation shows a photon antibunching dip at short time differences, implying that only one photon passes through the beam splitter at a given time. The red line is a single-exponential fit to the correlation function, which is determined by the apparent triplet-state lifetime. (e) Single-molecule PL intensity as a function of excitation power averaged for ~300 single molecules for each excitation intensity. The red line shows a fit to the data with a saturation function of the form $I(P_{\text{exc}}) = I_\infty(\frac{P_{\text{exc}}}{P_{\text{sat}}})/(1+\frac{P_{\text{exc}}}{P_{\text{sat}}})$, with I_∞ the saturated PL intensity, P_{exc} the excitation power and P_{sat} the saturation excitation power. Reproduced with permission from J. Phys. Chem. Lett. 6, 999 (2015). Copyright 2015 American Chemical Society.

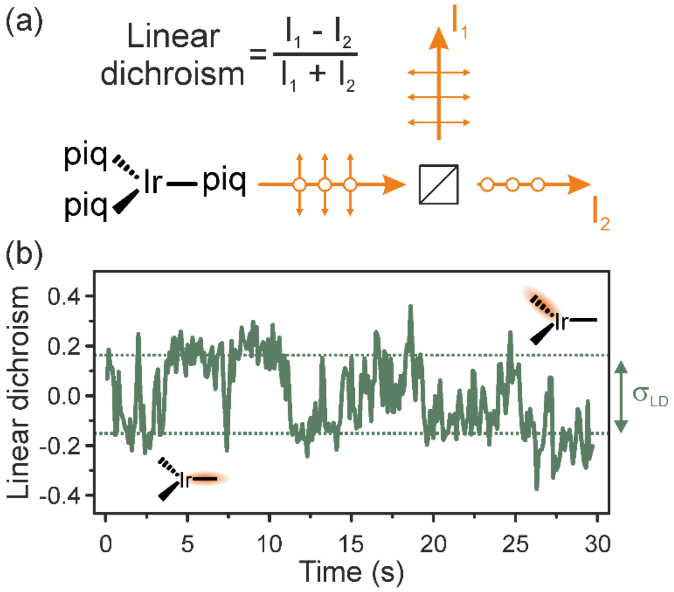

FIG. 27. Random polarization fluctuations in a single OLED triplet emitter molecule due to spontaneous symmetry breaking. (a) Light is passed through a polarizing beam splitter and detected by two photodiodes. The linear dichroism is defined as the difference-sum-ratio of the PL intensity in the two polarization planes. (b) A representative single-molecule time trace of the linear dichroism, demonstrating pronounced switching in emission polarization. The measured noise in the linear dichroism is defined as σ_{LD} and is found to be much greater than the overall noise in the emission intensity. Reproduced with permission from J. Phys. Chem. Lett. 6, 999 (2015). Copyright 2015 American Chemical Society.

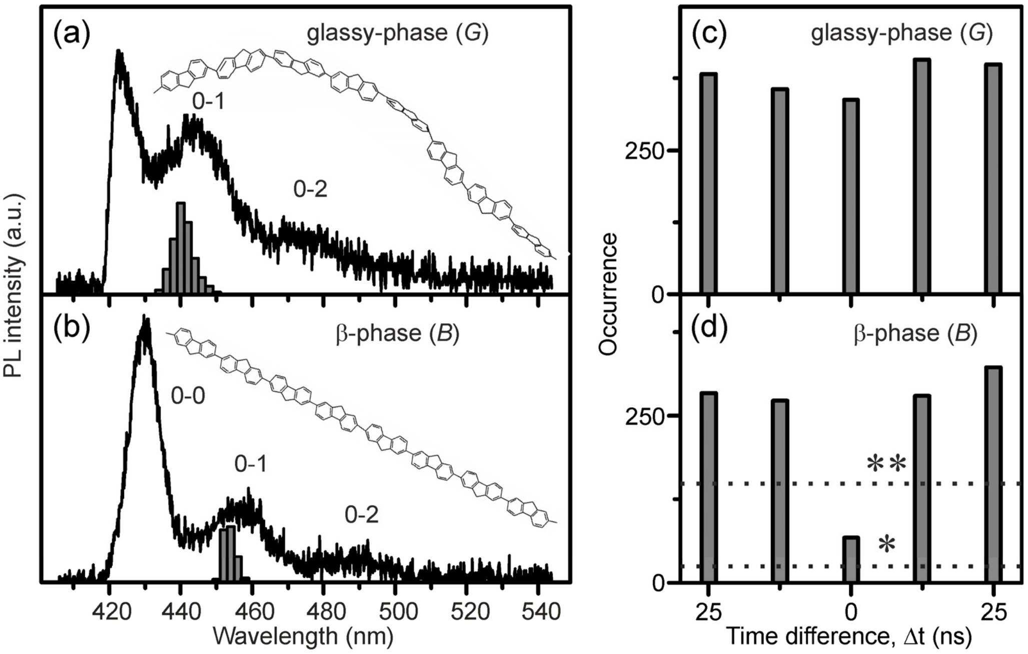

FIG. 28. Effect of molecular conformation on photon statistics from single chains of the π-conjugated polymer polyfluorene. (a, b) Differentiation between twisted glassy-phase and planarized β-phase polyfluorene chains in room-temperature single-molecule PL spectra. Histograms of the position of the 0−1 vibronic peak constructed from 147 molecules of each species. Note that the glassy-phase spectrum is truncated below 420 nm because of the optical filter used to block the excitation laser. The chemical structure of poly(9,9-dioctylfluorene) is sketched without showing the backbone substituents. The conformations shown are for illustration purposes only. (c, d) Photon coincidence histograms (at a 12.5 ns laser period) of single chains, summed over 16 single glassy-phase molecules and 12 single β-phase molecules. Reproduced with permission from J. Phys. Chem. Lett. 5, 2165 (2014). Copyright 2014 American Chemical Society.

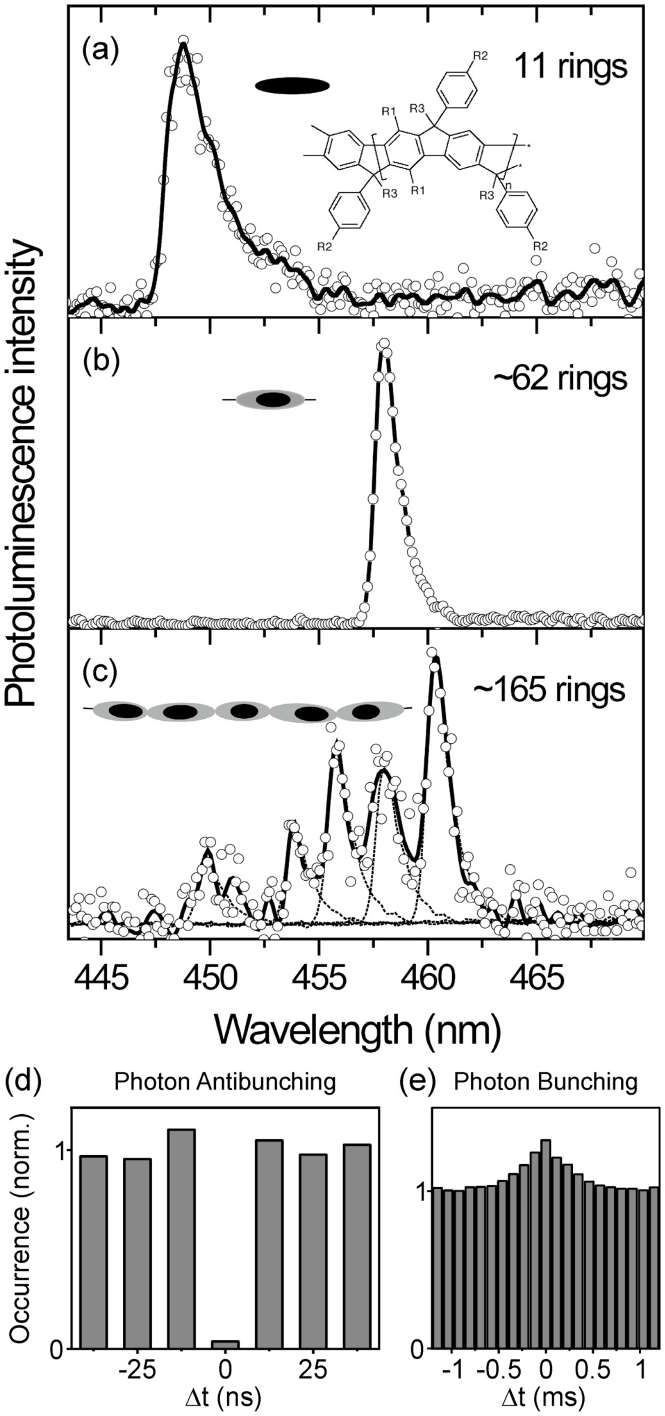

FIG. 29. Single-molecule PL spectra at 5 K of a model oligomer and the conjugated polymer LPPP (chemical structure inset) and the corresponding fluorescence photon statistics. Spectra are shown for the undecamer (a), a short-chain polymer ($M_r \approx 25$ kDa) (b), and a long-chain molecule ($M_r \approx 67$ kDa) (b). Each of the individual peaks in the emission spectrum from the long-chain material is identical in shape to the single peak in the emission from the short-chain polymer. This single peak is superimposed for each peak in panel (c) as dashed lines. The peaks can therefore be assigned to transitions on individual chromophores of the long polymer chain. The sketches indicate the difference between exciton size (black) and conjugation length (grey)

of the chromophore. (d)-(e) Energy transfer between the polymer chromophores is demonstrated by the fact that both strong photon antibunching and bunching occur in long polymer chains. (d) Photon correlation histograms of one single LPPP molecule, binned in intervals of the repetition period of the pulsed laser (12.5 ns) at room-temperature, showing strong photon antibunching. (e) Photon correlation histogram on the millisecond timescale demonstrating strong photon bunching due to triplet-state formation. Reproduced with permission from Angew. Chem. Int. Ed. 44, 1520 (2005). Copyright 2005 John Wiley and Sons. Reproduced with permission from J. Phys. Chem. Lett. 11, 5192 (2020). Copyright 2020 American Chemical Society.

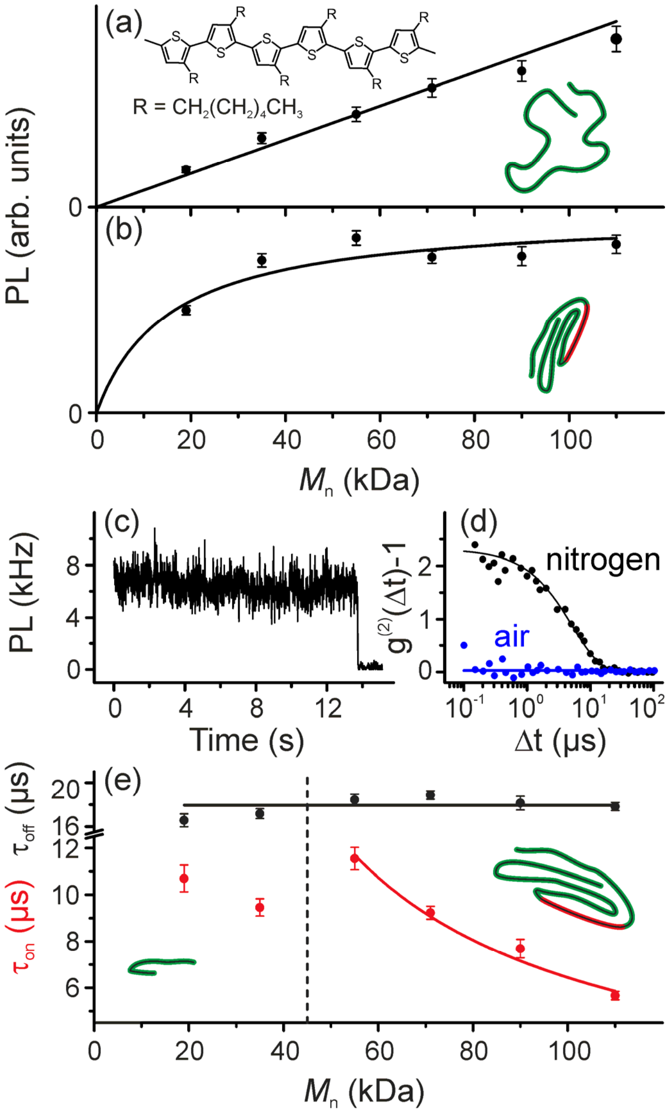

FIG. 30. Triplet quenching of the fluorescence of single folded polymer chains. (a) Perfectly unfolded and unaggregated regioregular poly(3-hexylthiophene) (P3HT) chains (structure inset) only exist in solution. The average PL intensity was obtained by fluorescence correlation spectroscopy in solution and plotted against the molecular weight M_{n}. (b) Folded chains are formed, on the single-chain level, by dispersion in a PMMA matrix. PL saturation with M_{n} can be described by a typical saturation curve (black line, cf. Fig. 26e). Error bars give the standard error. (d) Second-order cross-correlation, $g^{(2)}(\Delta t) - 1$, obtained from the PL transient in (c) under nitrogen atmosphere, where the triplet dark state is preserved. The cross-correlation curve becomes flat under oxygen (blue dots) because all triplets are quenched by O_2. (e) For each M_{n}, PL intensity transients of approximately 100 molecules were obtained to give averaged $g^{(2)}(\Delta t)$ curves, and the average "on" times τ_{on} of the PL were extracted (red dots) as were the "off" times τ_{off} (black dots). Error bars designate fitting-error values. "On" times for the two

lowest M_n samples deviate from the $1/M_\mathrm{n}$ dependence (red line) because the acceptor is not fully formed at this chain length, as illustrated in the sketch. The “off” times appear independent of M_n. Reproduced with permission from Phys. Rev. Lett. 112, 137402 (2014). Copyright 2014 American Physical Society.

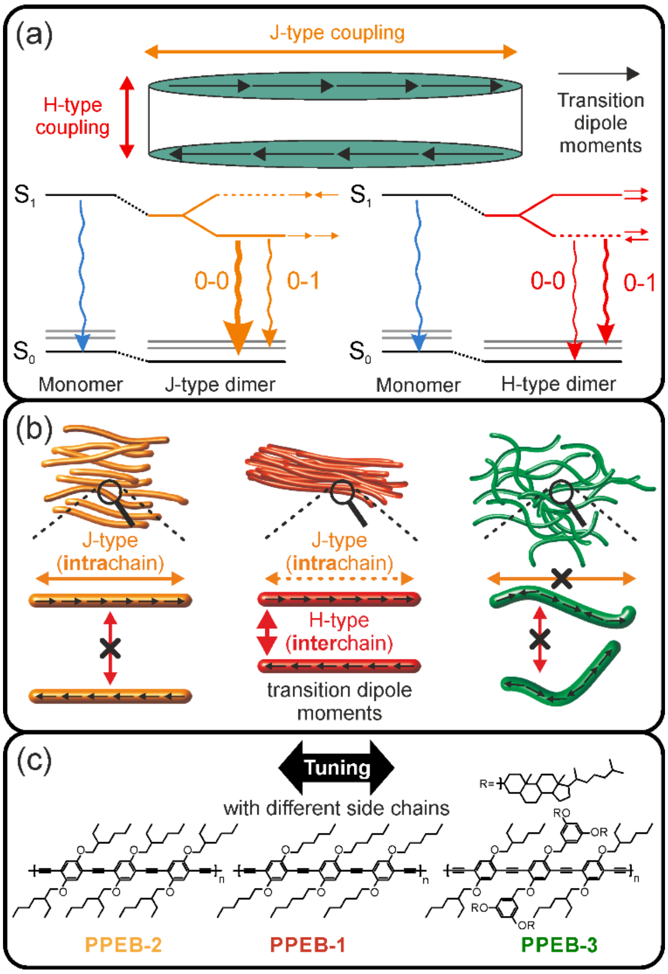

FIG. 31. Tuning intra- and intermolecular interactions in conjugated polymers. (a) J- and H-type coupling in π-conjugated molecular dimers. Transition-dipole moments (TDMs) of individual repeat units add up to yield a J-type aggregate excitation. The more ordered the chain, the greater the red-shift and the weaker the relative vibrational coupling. H-aggregation results from interactions between parallel chromophores and suppresses radiative recombination, enhancing the ratio of the vibronic-to-electronic fluorescence intensity. (b) The expected relationship of electronic aggregation phenomena to the microscopic aggregate morphology. (c) Chemical structures of polymer samples used to tune between H-type (PPEB-1), J-type (PPEB-2), and suppressed coupling (PPEB-3) by changing the side chains. Eder, T., Stangl, T., Gmelch, M., Remmerssen, K., Laux, D., Höger, S., Lupton, J. M. & Vogelsang, J. Nat. Commun. 8, 1641 (2017); licensed under a Creative Commons Attribution (CC BY) license.

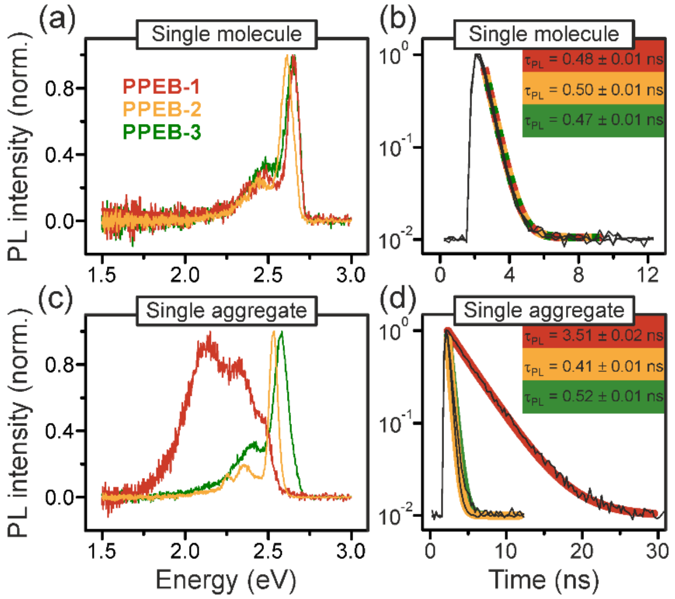

FIG. 32. Effect of electronic aggregation processes on PL spectra and PL lifetimes in single multichain polymer nanoparticles formed by controlled solvent-vapor annealing. (a, c) Typical normalized PL spectra of single chains and single aggregates of PPEB-1 (red), PPEB-2 (orange) and PPEB-3 (green) in PMMA, measured in air to facilitate deactivation of the dark triplet state. (b, d) Corresponding normalized PL decays of single chains and single aggregates. The transient PL was fitted with an exponential function offset to account for the background, yielding the PL lifetimes stated in (b) and (d). A strong effect of aggregation is observed for materials PPEB-1 and PPEB-2, but not for PPEB-3. Eder, T., Stangl, T., Gmelch, M., Remmerssen, K., Laux, D., Höger, S., Lupton, J. M. & Vogelsang, J. Nat. Commun. 8, 1641 (2017); licensed under a Creative Commons Attribution (CC BY) license.

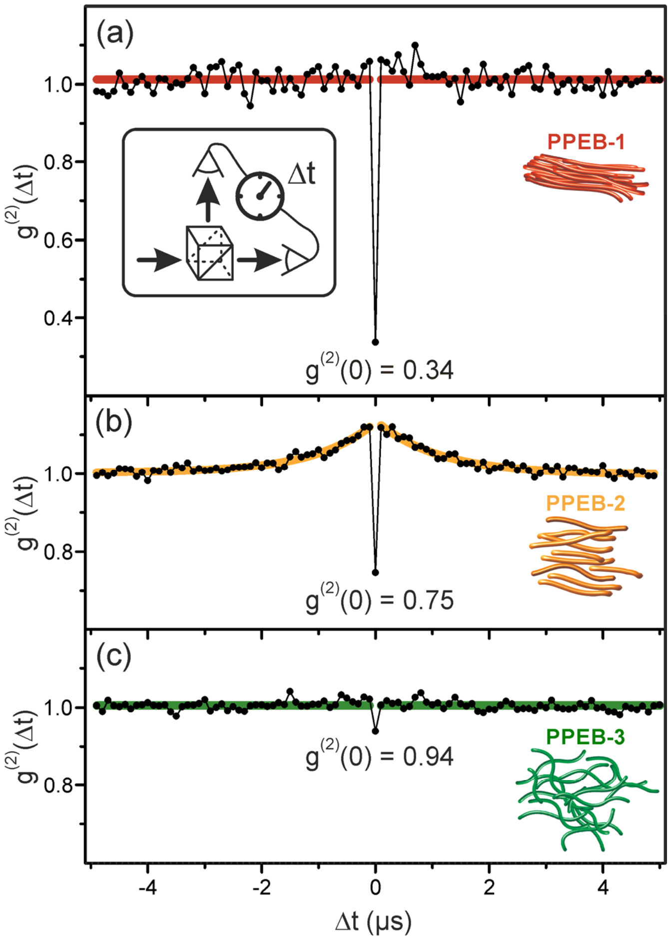

FIG. 33. Photon statistics of single multichain aggregates measured in air to prevent triplet buildup. Accumulated second-order cross-correlation curves $g^{(2)}(\Delta t)$ for (a) 57 single PPEB-1, (b) 47 PPEB-2, and (c) 44 PPEB-3 aggregates. The aggregates were excited by laser pulses (10 MHz repetition rate) to control the difference Δt in photon arrival time between the two detectors. The photon antibunching dip at $\Delta t = 0$ is apparent. In (b), photon bunching occurs for $|\Delta t| > 0$, which is described by a single-exponential fit (orange) yielding a short lifetime of the dark state, presumably the triplet which is strongly quenched by O_2, of approximately 1 μs. Eder, T., Stangl, T., Gmelch, M., Remmerssen, K., Laux, D., Höger, S., Lupton, J. M. & Vogelsang, J. Nat. Commun. 8, 1641 (2017); licensed under a Creative Commons Attribution (CC BY) license.

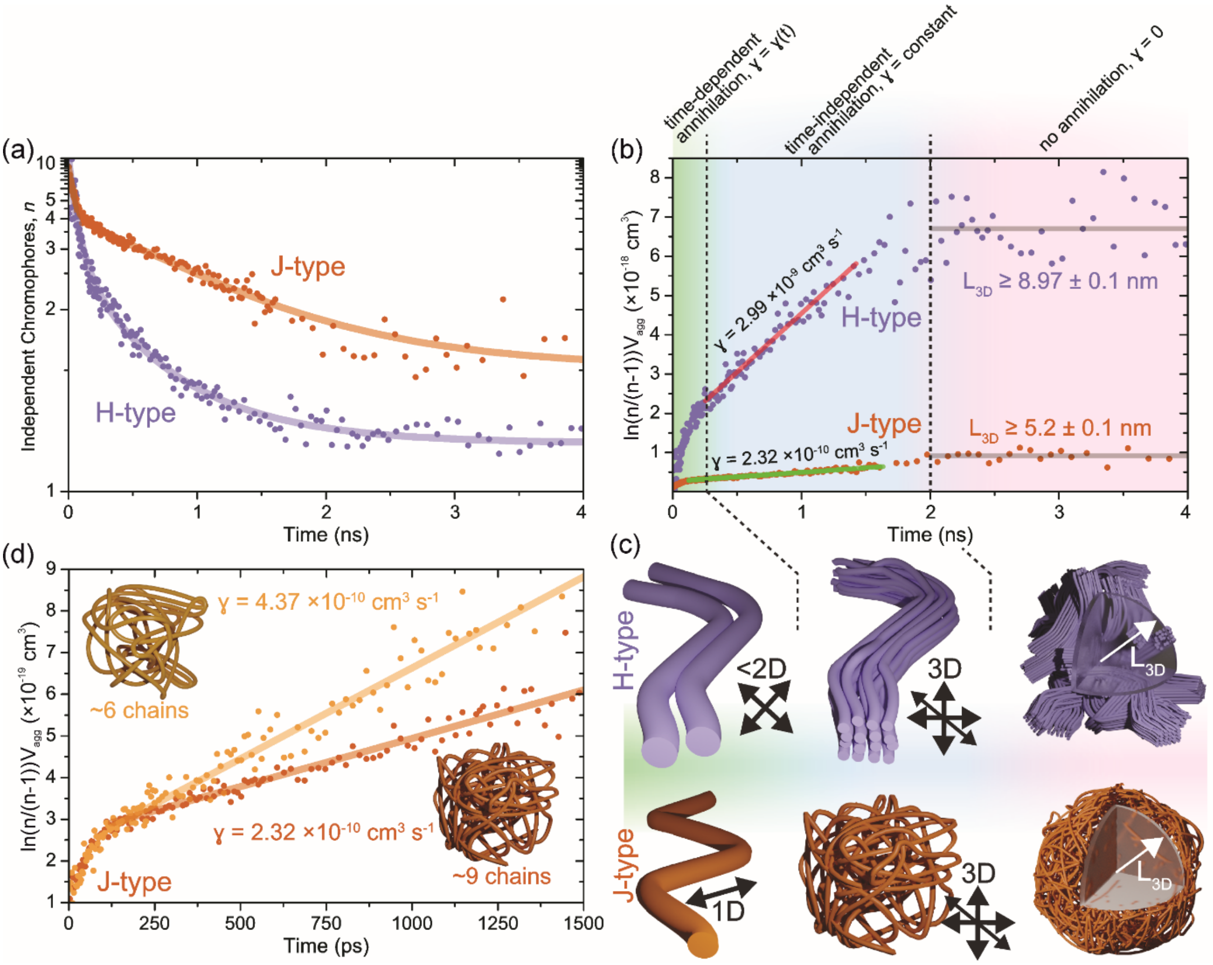

FIG. 34. Measuring exciton diffusion and the true number of emitting chromophores in multichain polymer aggregates by time-resolved photon antibunching. (a) Temporal evolution of the number of independent chromophores in the aggregate, determined as discussed in Fig. 17, for the H-type and J-type aggregates. A significant difference in the dynamics is observed. Lines shown are a guide to the eye. (b) Plotting of the time-dependent quantity ln $\left(\frac{n}{n-1}\right) V_{\text{agg}}$ for the H- and J-type aggregates reveals three distinct domains. The gradients of the curves correspond to the exciton annihilation rate, γ, of diffusion-controlled singlet-singlet annihilation as discussed in Fig. 18. At early time (0-250 ps), γ is time-dependent; at intermediate times (250-2,000 ps), γ is constant and ten times higher in the H- compared to the J-type aggregate; and at late times (> 2,000 ps), γ is zero. (c) Interpretation of the different domains of the exciton diffusion dynamics: at early times, diffusion is either one dimensional in the J-type aggregates, i.e. it occurs solely along the chains; or it is less than two-dimensional in the H-type aggregates, i.e. it occurs along chains and between a few parallel chains. At intermediate times, diffusion is three-dimensional, where the 3D aggregate is ordered in the case of H-type aggregation and more disordered in the case of J-type aggregation since intermolecular interactions are

suppressed. Note that the level of disorder is exaggerated in the cartoon. Finally, at late times, annihilation ceases because the exciton density is too low. The latter range provides a lower limit of the three-dimensional diffusion length $L_{3\mathrm{D}}$. (d) Comparison of the dynamics of the nine-chain J-type aggregate from panel (b) (brown) with a smaller six-chain aggregate (orange). The gradient of the diffusion dynamics, i.e. the singlet-singlet annihilation rate γ, is smaller by a factor of two in the larger aggregate, indicating that three-dimensional diffusivity is reduced when more chains are present. This reduction is consistent with reduced ordering of the chains with respect to each other as the aggregate grows larger, and thus with reduced interchain couplings. The six-chain dataset is made up of 260 individually measured single aggregates. Hedley, G. J., Schröder, T., Steiner, F., Eder, T., Hofmann, F., Bange, S., Laux, D., Höger, S., Tinnefeld, P., Lupton, J. M. & Vogelsang, J. Nat. Commun. 12, 1327 (2021); licensed under a Creative Commons Attribution (CC BY) license.